SPACEBORNE DEMONSTRATION OF P-BAND SIGNALS OF OPPORTUNITY REMOTE SENSING: INSTRUMENT MODELING AND VALIDATION

by

Benjamin Nold

A Dissertation

Submitted to the Faculty of Purdue University

In Partial Fulfillment of the Requirements for the degree of

Doctor of Philosophy

School of Electrical and Computer Engineering

West Lafayette, Indiana

May 2023

THE PURDUE UNIVERSITY GRADUATE SCHOOL
STATEMENT OF COMMITTEE APPROVAL

Dr. James Garrison, Co-Chair

School of Aeronautics and Astronautics

Dr. Mark Bell, Co-Chair

School of Electrical and Computer Engineering

Dr. Michael Zoltowski

School of Electrical and Computer Engineering

Dr. Jeffrey Piepmeier

National Aeronautics and Space Administration - Goddard Space Flight Center

Approved by:

Dr. Dimitrios Peroulis

To my parents, Jonathan and Kimberly Nold. Without their support, I would not have made it to the end of my PhD.

To my siblings who provided the emotional support for me through this, Katherine and Rebekah Nold.

ACKNOWLEDGMENTS

First to my mentor, Dr. James Garrison. Thank you for extending the opportunity for me to join your lab for a Summer as an undergrad so many years ago. I hope I have been able to contribute to the success of the Radio Navigation Lab and the SNOOPI Mission.

To my lab mates throughout my time in the Radio Navigation Lab! Sidd, thank you for the week of your time at ACRE helping assemble WYATT-EIRP. Seho, Eric and Archie, for the times we both spent working on tower data, front-end assembling and other various "fun" at ACRE. Abi, Harris, Feixion, Han, Aakash, and Leo. Thank you for conversations and the good times. Special shout out to Jared, Kevin, and Christian. Thank you for your friendship through the grad school years.

I would like to thank Luke Winternitz, Manuel Vega, and Jeff Piepmeier at NASA Goddard Space Flight Center. Thank you for allowing me to raid your personal textbook libraries and the countless hours spent discussing SNOOPI.

Dave and Tina McGuffey, Jawalleh Deborah Promise, Ron Pieper, Carole Ritchie Pieper, and Connie Buck, you are my Maryland family. Thank you for sharing your houses, and especially your friendship during my long, drawn out degree.

Mom and Dad, your son has finished attending college full-time as an engineering student (finally).

TABLE OF CONTENTS

LIST OF TABLES

LIST OF FIGURES

ABBREVIATIONS

COTS	Commercial Off The Shelf
DBE	Digital Back End
EIRP	Effective Isotropic Radiated Power
FPGA	Field Programmable Gate Array
FFT	Fast Fourier Transform
JPL	Jet Propulsion Laboratory
LNFE	Low Noise Front End
NASA	National Aeronautics and Space Administration
GSFC	Goddard Space Flight Center
SoOp	Signals of Opportunity
SNOOPI	Signals of Opportunity P-Band Investigation
SDR	Software Defined Radio

ABSTRACT

Signals of Opportunity (SoOp) reflectometry allows the reuse of existing communication signals as sources of illumination for remote sensing. The Signals of Opportunity P-band Investigation (SNOOPI) mission is a spaceborne technology demonstration of a P-Band SoOp receiver. P-Band frequencies allow for deeper penetration depths for soil moisture sensing than conventional L-Band radar instruments. P-Band also allows for higher precision in applications requiring phase unwrapping such as Snow Water Equivalent measurements. To support the SNOOPI instrument development and analysis, a bit-level simulator was developed to verify the microwave instrument and digital signal processor unit. A ground-monitoring station was developed to monitor the SoOp source's Effective Isotropic Radiated Power (EIRP), background noise sky-map verification, and self-ambiguity function monitoring. An overview of tower based instruments implementing the SoOp receiver technique is also provided.

1. INTRODUCTION

Root Zone Soil Moisture (RZSM) and Snow Water Equivalent (SWE) play critical roles in water resource management, agriculture, and climate studies. Both parameters are identified by the National Academy of Sciences in the *Earth Science and Application from Space* Decadal Survey as priority target variables, stating that they require accurate and frequent measurements [1]. RZSM knowledge is key to understanding various hydrological processes, including floods, droughts, agriculture production, and climate change modeling [2]. RZSM is the amount of stored water available to plants, which is vital for agriculture planning and crop yield predictions. Additionally, it dominates the radiation to land heat exchange processes, and influences precipitation's transition between evapotranspiration and water runoff.

SWE is the measurement of the amount of water stored in the snowpack. Because snow is an insulator with high albedo, SWE measurements are essential for estimating run off during the spring melt. SWE is required for forecasting seasonal stream-flow and water availability in snow-dominated regions [3]. Accurate SWE measurements are needed for water resource management applications, managing reservoirs and flood forecasting, irrigation planning and agriculture production.

Although accurate knowledge of these variables are essential, current spaceborne remote sensing measurement techniques cannot directly measure RZSM or SWE. Although spaceborne radars are sensitive to soil moisture, they cannot penetrate into the root zone. RZSM estimates are formed using data assimilation with physical modeling. SWE also cannot be directly measured from space and must be derived from multi-sensor data fusion and hydrological modeling techniques. This work covers the design and modeling of a novel, low-frequency spaceborne radar that is designed to be directly sensitive to both RZSM and SWE.

1.1 In Situ Measurements

Soil moisture is measured in situ by various labor intensive methods. The soil gravimetric method requires the removal of soil from the measurement site, and the transportation of

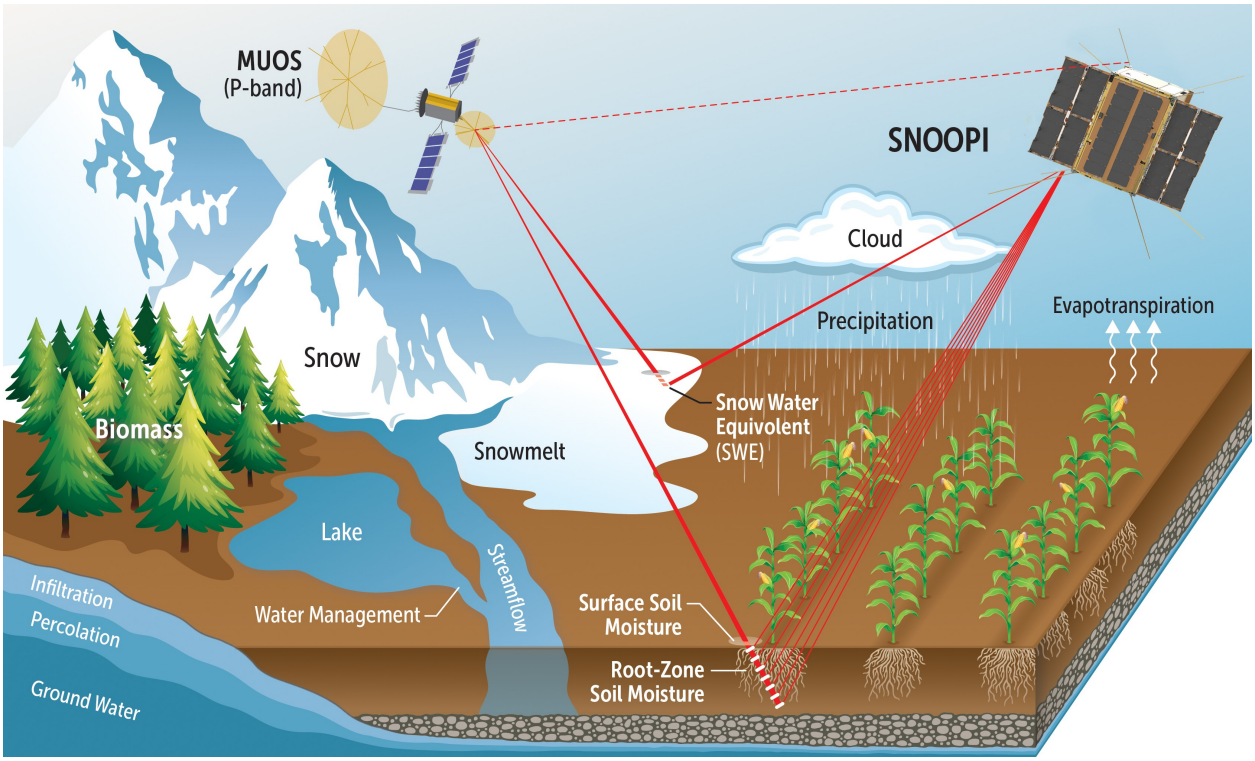

Figure 1.1. Space Based SoOp Receiver

the sample to a oven for drying. The sample is weighed before and after the week long drying processes. Soil core sampling tools can be used to extract soil from the root zone for gravimetric measuring, but these tools can be challenging to use in dry soil conditions and in the presence of roots [4]. This method directly measures the water content of soil, but it is labor intensive for both temporal and spatial resolution.

In situ electrical sensors are also used to measure soil moisture. Common sensor types are capacitance, impedance and time domain reflectivity. Sensors provide sub-second temporal resolution but are labor intensive to increase their spatial resolution. Each sensor must be buried in the soil at the required measurement depth. This can become labor and time intensive to install sensors into the root zone, up to 2 meters deep in some applications. Furthermore, periodic soil gravimetric measurements are typically required to calibrate the sensors.

In situ measurements of SWE are also labor and time intensive. SWE can be directly measured via the gravimetric method; snow is removed from the snowpack and weighed. Depending on the measurement requirements, either a handheld snow sampling tool or snow tube is used to obtain the snow. A handheld snow sampling tool requires the digging of a snow pit from the top of the pack to the ground, large enough for a person to stand in. A snow tube can obtain the measurement while standing on top of the snow, but depending on the snow pack, particularly in the presence of ice layers, handles have to be fit to the tube to rotate and bore the tube through the snowpack. [5],

Electrical sensors have been developed to measure SWE. The traditional sensor for SWE is a snow pillow, a circular ballast filled with anti-freeze, installed flush to the ground. The snowpack over the pillow causes a pressure change sensed by transducers. Snow pillows cannot be used in sloping ground conditions and do not perform well in areas with frequent freeze-thaw events. Other methods include neutron probes, cosmic radiation probes, time domain reflectometry, and capacitive sensors [6].

1.2 Space Based Remote Sensing

Current spaceborne microwave instruments targeting RZSM and SWE are either active radar or passive radiometers. These technologies can only operate in protected RF bands classified for science. There are very few bands allocated for spaceborne earth observation remote sensing, and the lowest of these bands is at 1.2 GHz.

The current best spaceborne radar remote sensing instruments is the Soil Moisture Active Passive (SMAP) satellite. SMAP operates in L-Band and had an active radar at 1.21 GHz paired with a passive radiometer operating at 1.41 GHz. SMAP was designed to provide soil moisture data with a spatial footprint of approximately 9 km4. It employs a deployable, rotating 6 m mesh reflector antenna to achieve the spatial resolution requirement. Due to L-Band, SMAP is only sensitive to approximately the top 5 cm of soil-moisture; data assimilation is needed to provide estimates of RZSM [7]. Unfortunately, the active radar failed in July, 2015 due to a work defect. As a consequence of the failure, SMAP can only

use its passive radar, resulting in a 36 km sensing footprint [8]. SMAP's orbit provides 2-3 day revisit, global soil moisture data product.

SWE cannot currently be directly measured from space but rather is derived from data fusion and assimilation techniques. SWE estimates using multi-frequency passive microwave instruments have high error in retrieval with deep snow, forests, and mountain environments [9] [10] [11].

1.3 Signals of Opportunity

Signals of Opportunity (SoOp) is an emerging microwave remote sensing technology that can operate in any allocated microwave RF band. A SoOp instrument is completely passive, reusing existing digitally modulated signals as sources of illumination in a bi-static radar configuration. This allows for lower power requirements and smaller instrument payload designs in comparison with active radars and smaller antenna sizes than passive radiometers.

SoOp began utilizing L-Band signals from Global Navigation Satellite Systems (GNSS) for ocean winds applications [12]. GNSS-R has recently expanded to soil moisture applications, repurposing the radar on SMAP [13] and using CYGNSS data products [14], [15]. In 2012, it was demonstrated that any digital communication signal could be used as a SoOp source [16]. This development allowed for signals in virtually all occupied microwave bands to be used for remote sensing, including the lower frequency bands that exhibit higher sensitivity to SWE and RZSM.

SoOp instruments focusing on RZSM have been designed that operate in P-Band which offers the possibility to directly measure up to 1.5 meters into soil. In 2017, an airborne instrument demonstrated sensitivity to soil moisture using SoOp in P-Band [17], [18]. Tower based instruments have been demonstrated using SoOp in P-Band for RZSM as well [19], [20]. More recent work using I-Band SoOp sources has been done with UAV instruments as well [21].

SoOp has also been used the remote sensing of SWE in both S and P-Band [22], [23]. Analytical models of the SWE retrieval have also been developed **shah2017**.

This thesis details the design and analysis of a new SoOp spaceborne instrument operating in P-Band. The Cubesat SNOOPI (SigNals Of Opportunity P-band Investigation) has a dual band, 255 and 370 MHz SoOp receiver, designed to demonstrate SoOp technology in space. P-Band was chosen for SNOOPI, because it offers the ability to directly measure up to 1.5 meters into soil. In the following chapter, the instrument signal model is defined and numerically validated using an sample level bit-simulator designed for this work. The ground based monitoring station, WYATT-EIRP is discussed as well as a the design of a new tower-based multi-frequency SoOp Instrument. Finally an analysis is presented of raw P-Band data that was recorded in orbit, demonstrating the first example of spaceborne P-Band SoOp using a single antenna.

2. THE SNOOPI MISSION

Figure 2.1. Artist Rending of SNOOPI in Orbit

The SNOOPI (Signals of Opportunity P-band Investigation) mission is a technology demonstration of a P-Band SoOp remote sensing instrument to be flown on a 3X2 (6U) CubeSatellite spacecraft. The SNOOPI mission consists of three goals [24]:

1. Verify reflected signal coherence from Low Earth Orbit altitudes under a variety of different surfaces conditions.

2. Demonstrate robustness of the SoOp retrieval in presence of RFI (Radio Frequency Interference).

3. On orbit demonstration of the delay/Doppler prediction algorithm to validated end-to-end instrument tools and system error budget.

2.1 Signals of Opportunity Source Selection

SNOOPI is designed to observe two P-Band signals of opportunity sources: UHF Follow On (UFO) at 255 MHz and Multiple User Objective System (MUOS) at 370 MHz [25]. The MUOS satellites transmit both the legacy UFO channels and its replacement system MUOS, a summary of the channels are showed in Table 2.1. This source has several desirable features for the SNOOPI mission:

- Geostationary Orbit

  This reduces the complexity of the delay-Doppler prediction, as the specular point location is only a function of the position of the SNOOPI spacecraft and the reflecting surface height.

- Multiple Down-link Bands on a Single Platform

  This enables Snoopi to make a phase retrieval using two sources separated in frequency (UFO at 255 MHz and MUOS at 370 MHz). The change in phase between the two sources is only a function of the reflection media, surface height and the position of the SNOOPI spacecraft.

- Near Global Coverage

  The MUOS constellation has 5 spacecraft transmitters in total providing global coverage. This enables follow-on missions from SNOOPI to have global coverage.

Table 2.1. SNOOPI Microwave Instrument Summary

	MUOS	UFO	Units
Operating Frequency	360-380	240-270	MHz
Number of Channels	4	17	-
Channel Bandwidth	5000	25	kHz
Assumed Transmit Power	37	26	dBW
Microwave Front End Bandwidth	20	30	MHz
Front End Noise Figure	1100	1100	K
Front End Diode Power	1500	1500	K

2.1.1 Instrument Antenna

SNOOPI went through several design iterations. Initially a 1x6U CubeSat design was planned, but it was found that COTS antennas for the instrument were not readily available. Due to the lack of civilian operating space-to-earth communication band allocations in the P-Band range, there were very few COTS antenna options. Additionally, elementary physics of the the P-Band wavelength $\approx 1.5 - 2$m sets a lower bound on general antenna designs size to be on the same size of a CubeSat.

COTS communication antennas were procured from GomSpace. These antennas were designed to operate in the frequency range of 340-680 MHz. Two antennas were procured, one designed for 370 MHz and one for 255 MHz. The antennas are a canted turnstile design providing RHCP polarization in the forward direction and LHCP in the reverse direction. As a complete coincidence of engineering history, this antenna design was initially conceived at NASA Goddard to be an omni-directional circularly polarized antenna design for satellites in the mid 1960's [26].

2.1.2 Low Noise Front End

The instrument Low Noise Front End (LNFE) was designed by NASA Goddard Instrument Systems and Technology Division. The LNFE is a four channel instrument providing approximately 45 dB of gain. The LNFE has low insertion loss, sharp roll-off RFI filters to protect the instrument from adjacent RF signals. The LNFE has two internal calibration sources, a matched load and a noise diode. The gain stage ends with a limiter to further protect the instrument from RFI.

2.1.3 Digital Back End

The digital back end was designed by NASA Jet Population Laboratory. The DBE is designed to accept 4, 50 MHz P-band RF inputs. The RF chain uses a a down conversion IC and a 14 bit analog-to-digial converter. The DBE's processor is a Cubesat Space Processor

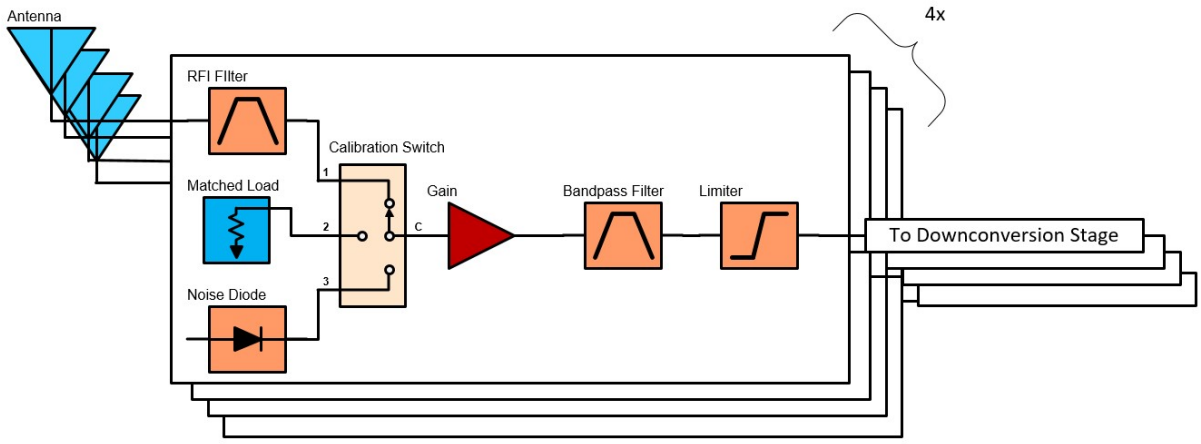

Figure 2.2. Instrument LNFE Block Diagram

(CSP) which has a Xilinx Zynq 7020 FPGA and ARM Processor system on chip. The DBE is also connected to a Novatel OEM 729 GNSS receiver to allow for time-tagging of the data.

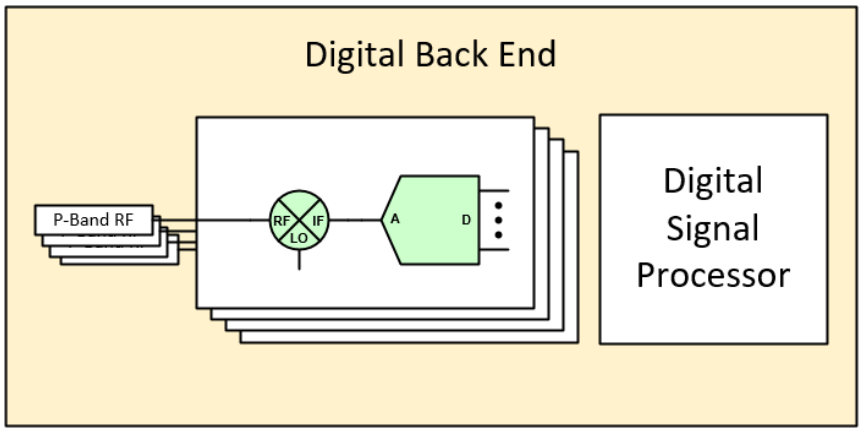

Figure 2.3. Instrument DBE Block Diagram

Unfortunately, due to FPGA limitations, the DBE is not able to process all of the available channels. The DBE processes five of the 25 KHz, 255 MHz band channels and a single 5 MHz 370 MHz channel. Also, only 2 of the 4 RF channels can be used simultaneously, a single 255 and 370 MHz channel. A summary is provided in Table 2.2.

Table 2.2. DBE Correlating Parameters

	MUOS	UFO	Units
Number of Channels	1	5	
Correlation Bandwith	5000	25	kHz
Number of Samples in 1 ms	5000	25	Samples

The DBE has three operating modes. The primary mode is the Delay Doppler Map (DDM) generation mode. This mode will generate complex DDMs and a corresponding signal energy calculation at 1 ms period. The DBE can also generate perform complex averaging on the DDMs and generate DDMs at a 2-10 ms period. At launch, the DBE will be programmed to generate DDM's at 2 ms. The DBE also has two "data capture mode" that allows for raw sample data to be recorded and saved. Table 2.4 shows the summary of the data recording mode.

Table 2.3. DBE DDM Generator Summary

Signal Band	255	370
Channel Bandwidth	5 KHz	5 MHz
Numer of channels	5 MHz	1 MHz
Aggregate Bandwidth	25 KHz	5 MHz
Chip Length	12 km	60 m
Delay Resesolution	60 m	15 m
Delay Bins	5	200
Doppler Bins	3	3

The DBE also has two "data capture mode" that allows for raw sample data to be recorded and saved. Table 2.4 shows the summary of the data recording mode.

Table 2.4. Data Capture Mode Summary

RAW Mode		
255 Mhz	50 Mhz	500 KHz
Recording Time	1 s	100 s
IF Mode		
370 Mhz	50 MHz	5 Mhz
Recording Time	1 s	10 s

2.2 Launch Plans

SNOOPI's launch is planned for early 2024. It will be launched from the International Space Station (ISS) via the NanoRacks CubeSat Deployer. This will result in a orbit similar to the ISS at 400 km, 51.6 deg with a planned 9 months of operation. All input to the simulations in this work assumes a ISS launch orbit.

3. SINGLE ANTENNA THEORETICAL DERIVATION

The following is the theoretical deviation for estimating reflectivity using a single antenna. This derivation is used for the basis of the SNOOPI sample simulator.

The following assumptions are made in this derivation:

1. The transmitted SoOp source is multiple QPSK modulated channels. The data is assumed to be uncorrelated uniform wide-sense stationary
2. The transmitted RF signal is circularly polarized
3. There is a single antenna on the instrument and it is sensitive to both the direct and reflected signals.
4. The reflected electromagnetic signal is assumed to be reverse polarization
5. The reflection is specular and coherent.

The first assumption is a property of the data of the SoOp source and can be modeled as a random variable. The 2nd through 5th assumptions are physical properties of the radio frequency of the SoOp source.

3.1 Basic Setup

Effective Isotropic Radiated Power

The Effective Isotropic Radiated Power (EIRP) is the radiated power from an RF transmitter, accounting for the antenna gain pattern and internal amplifier gains.

$$EIRP = G_T P_T$$

Free space path loss:

$$L_r = \left(\frac{\lambda}{4\pi r}\right)^2$$

Function of r (distance) and λ signal wavelength.

Radar Equation with Coherent Reflection:

$$C_R = \frac{G_T P_T \lambda^2}{\Big(4\pi(R_{TS} + R_{SR})\Big)^2}\Gamma$$

The received power C_R is proportional to the distance between the transmitter and the specular point R_{TS} and the distance between the specular point to the receiver R_{SR} and the reflectivity of the media Γ.

Electromagnetic Wave-Media Interaction

The receiver is estimating reflectivity Γ (units of power) which is due to the interactions of the electromagnetic wave with the reflected media.

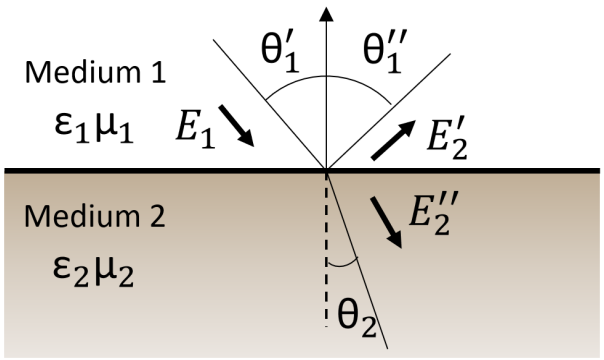

Figure 3.1. Electromagnetic Wave Reflection

When an electromagnetic wave transitions between two media the wave may split, partially reflecting and transmitting. The Fresnel coefficients determine the amplitude of the reflected and transmitted wave due to the differences in permittivity between the media. The Fresnel coefficient for a horizontally-polarized plane wave is given by:

$$\mathcal{R}_{HH} = \frac{E''_{H1}}{E'_{H1}} = \frac{cos(\theta_1) - \sqrt{\epsilon_{2r} - sin^2(\theta_1)}}{cos(\theta_1) + \sqrt{\epsilon_{1r} - sin^2(\theta_1)}} \tag{3.1}$$

where: ϵ_{1r}, ϵ_{2r} are the complex dielectric constants of the media. ϵ is dependent on soil composition and soil moisture.

Similarly for a vertically polarized plane wave:

$$\mathcal{R}_{VV} = \frac{E''_{V1}}{E'_{V1}} = \frac{\epsilon_{2r}cos(\theta_1) - \sqrt{\epsilon_{2r} - sin^2(\theta_1)}}{\epsilon_{2r}cos(\theta_1) + \sqrt{\epsilon_{2r} - sin^2(\theta_1)}} \tag{3.2}$$

A simple transformation can be done to convert from horizontally polarized waves to circular polarization:

$$\begin{bmatrix} \mathcal{R}_{RR} & \mathcal{R}_{RL} \\ \mathcal{R}_{LR} & \mathcal{R}_{LL} \end{bmatrix} = \frac{1}{2} \begin{bmatrix} \mathcal{R}_{HH} + \mathcal{R}_{VV} & \mathcal{R}_{HH} - \mathcal{R}_{VV} \\ \mathcal{R}_{HH} - \mathcal{R}_{VV} & \mathcal{R}_{HH} + \mathcal{R}_{VV} \end{bmatrix}$$

The subscripts H and V denote horizontal and vertical polarization respectively. The subscripts RR and LL correspond to the wave that remains RHCP or LCHP upon reflection. The subscripts RL and LR correspond to the wave that changes from RHCP to LHCP upon reflection and LCHP to RHCP respectively.

Reflectivity

Reflectivity (units of power) is the square of the reflection coefficient (units of amplitude):

$$\Gamma = \mid \mathcal{R} \mid^2$$

3.2 Signal Processing Definitions

For a continuous, finite energy signal $x(t)$:

Time Averaging Notation

Finite time averaging will be use the following notation:

$$\frac{1}{T} \int_{-T/2}^{T/2} x(t)dt = \Big\langle x(t) \Big\rangle_T \tag{3.3}$$

Square brackets $[n]$ will be used to denote a discrete signal. The equivalent finite time average for a discrete signal:

$$\frac{1}{N}\sum^{N} x[n]dt = \Big\langle x[n] \Big\rangle_N \tag{3.4}$$

Energy of a Signal

$$E_x = \Big\langle x[n], x[n] \Big\rangle_N = \frac{1}{N}\sum^{N} \Big| x[n] \Big|^2$$

Autocorrelation

The autocorrelation of a random signal is defined as:

$$R_s(\tau) = E\Big\{ s(t)s^*(t-\tau) \Big\}$$

Autocorrelation of exponential function

$$R_s(\mathrm{e}^{\mathrm{j}\omega t}) = \Big\langle \mathrm{e}^{\mathrm{j}\omega t} \Big\rangle = sinc\Big(\frac{\omega\tau}{2\pi}\Big) \tag{3.5}$$

Autocorrelation Properties

Even Function:

$$R_a(\tau) = R_a^*(-\tau) \tag{3.6}$$

Spectrum of a random process

$$S(f) = \int_{-\infty}^{\infty} R_s(\tau)\mathrm{e}^{-2\pi f\tau \mathrm{j}} df$$

Because $s(t)$ is normalized to unity power, $R_s(0) = 1$, $\int S(f)df = 1$

System Noise Random Variable

The system noise $\eta(t)$ is assumed to be a zero mean band-limited white Gaussian random processes with a power spectral density of:

$$S(f) = \frac{N_0}{2}$$

Assume we apply a filter of bandwidth B to the noise with frequency response:

$$H(f) = \begin{cases} 1, & \mid f \mid \leq B \\ 0, & \mid f \mid > B \end{cases}$$

The power of the noise $\eta(t)$ is then:

$$P_n = \int_{-\infty}^{\infty} S_n(f)df = \frac{N_0}{2}\int_{B}^{B} 1dF = N_0 B \tag{3.7}$$

The autocorrelation of $\eta(t)$:

$$R_n(\tau) = \mathcal{F}^{-1}\{S_n\} = \int_{-B}^{B} \frac{N_0}{2} \mathrm{e}^{\mathrm{j}2\pi f\tau} df = N_0 \frac{sin(2\pi B\tau)}{2\pi B\tau} = N_0 B sinc(2B\tau) \tag{3.8}$$

Noise Power

For a microwave signal with power P, the equivalent noise bandwidth is expressed as:

$$P = kT_{\mathrm{e}}B$$

where k is Boltzmann's constant, T_{e} is the equivalent noise temperature of the source in Kelvin, and B is the measurement bandwidth.

3.3 Signal Model

For this analysis, we assume the transmitter is spaceborne and at an altitude higher than the spaceborne receiver, as shown in Figure 3.2. We assume the instrument antenna

has a gain pattern given by $G_p(\vec{\Omega})$, where p is the polarization and $\vec{\Omega}$ is a unit vector. The transmitted signal is RHCP polarized: $G_D = G_{RHCP}(\vec{\Omega_D})$, $G_R = G_{LHCP}(\vec{\Omega_R})$. Ω_D is the unit vector towards the transmitter and Ω_R is the unit vector towards the reflection point. It is assumed that the cross polarization components $G_D = G_{LHCP}(\vec{\Omega_D})$, $G_D = G_{RHCP}(\vec{\Omega_R})$ are negligible. We can make this assumption for SNOOPI based on the gain patterns of the antenna.

A signal C as transmitted from a source is modeled as:

$$x(t) = \sqrt{C}s(t)e^{j\omega_c t} \tag{3.9}$$

Where C is the transmit power, $s(t)$ is the normalized signal modulation and $e^{j\omega_c t}$ is the signal carrier.

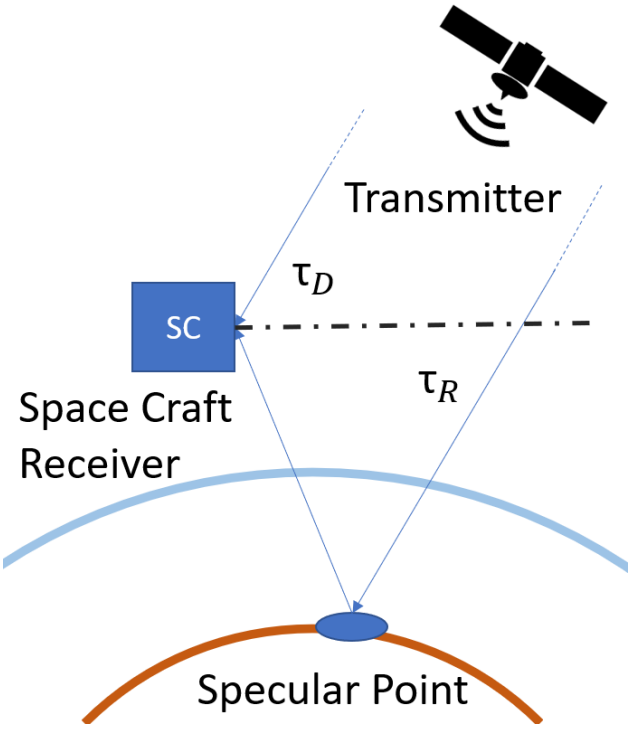

Figure 3.2. Basic Bi-Static Reflection Geometry

Using a ray path model with a single, specular reflection point the signal received at the space craft:

$$x_D(t) = \sqrt{C_D}s(t-\tau_D)\mathrm{e}^{\mathrm{j}\omega_D(t-\tau_D)} \tag{3.10}$$

$$x_R(t) = \sqrt{C_R}s(t-\tau_R)\mathrm{e}^{\mathrm{j}\omega_R(t-\tau_R)} \tag{3.11}$$

The reflected delay $\tau_R = \tau_{TS} + \tau_{SR}$ is defined as the delay from between the transmitter and the specular point τ_{TS} and the delay from the specular point to the receiver τ_{SR}.

The power of the signal at the instrument antenna from the direct signal path:

$$C_D = \frac{G_T P_T \lambda^2}{(4\pi R_D)^2}$$

The power of the signal at the instrument antenna reflected path with a coherent reflection:

$$C_R = \frac{G_T P_T \lambda^2}{(4\pi(R_{TS}+R_{SR}))^2}\Gamma$$

Because of the extra path length the reflected signal travels to the instrument, the estimated observable "effective reflectivity" needs to be corrected. The observed reflection coefficient $\mathcal{R}_\mathrm{e}$ is related to the surface reflection coefficient $\mathcal{R} = \sqrt{\Gamma}$.

$$\mathcal{R}_\mathrm{e} = \frac{R_D}{(R_{TS}+R_{SR})}\sqrt{\frac{G_R}{G_D}}\mathcal{R} \tag{3.12}$$

A low noise front end (LNFE) provides system gain G_{sys} and noise η_{FE}. Then the received signal is represented as:

$$x(t) = \sqrt{G_{sys}}\left[\sqrt{G_D C_D}a(t-\tau_D)\mathrm{e}^{\mathrm{j}\omega_D(t-\tau_D)} + \sqrt{G_R C_R}a(t-\tau_{RD})\mathrm{e}^{\mathrm{j}\omega_R(t-\tau_R)} + \eta_{sys}(t)\right] \tag{3.13}$$

Where: $\tau_{RD} = \tau_R - \tau_D$. $\eta_{sys}(t)$ is a band-limited white Gaussian noise processes with the standard deviation of the microwave system's thermal noise equivalent noise temperature T_{FE}, and the antenna temperature due to the scene and galactic noise T_A. Also note the

receiver will apply the down-conversion frequency ω_a. For the rest of the derivation, it is assumed that $e^{j\omega_D t}, e^{j\omega_R t}$ has been converted to an intermediate frequency. Also note, ω_D, ω_R will vary independently of each other due to Doppler shift of the SNOOPI spacecraft.

Receiver Signal Processing

The receiver will generate a delay-Doppler map via:

$$R(\tau,\omega) \ = \frac{1}{T}\int x(t)x^*(t+\tau)e^{j\omega t}\,dt = \Big\langle x(t)x^*(t-\tau)e^{j\omega t}\Big\rangle_T \tag{3.14}$$

This function will generate a map over delay τ and frequency ω.

$$\begin{aligned}
R(\tau,\omega) = G_{sys}\Big[& G_D C_D < a(t-\tau_D)a^*(t-\tau_D-\tau)e^{j\omega t} > e^{j(\omega_D+\omega)\tau} + \\
& G_R C_D \Gamma < a(t-\tau_R)a^*(t-\tau_R-\tau)e^{j\omega t} > e^{j(\omega_R+\omega)\tau} + \\
& C_D\sqrt{G_D G_R \Gamma} < a(t-\tau_D)a^*(t-\tau_R-\tau)e^{j(\omega_D-\omega_R+\omega)t} > e^{j(\omega_R\tau_R-\omega_D\tau_D)}e^{-j\omega_R\tau} + \\
& C_D\sqrt{G_D G_R \Gamma} < a(t-\tau_R)a^*(t-\tau_D-\tau)e^{j(\omega_R-\omega_D+\omega)t} > e^{j(\omega_D\tau_D-\omega_R\tau_R)}e^{-j\omega_D\tau} + \\
& \sqrt{G_D C_D} < a(t-\tau_D)n^*(t-\tau)e^{j\omega_D+\omega t} > e^{-j\omega_D\tau_D} + \sqrt{G_R C_D \Gamma} < a(t-\tau_R)n^*(t-\tau)e^{j\omega_R+\omega t} > e^{-j\omega_R\tau_R} + \\
& \sqrt{G_D C_D} < n(t)a^*(t-\tau_D-\tau)e^{j(\omega-\omega_D)t} > e^{j\omega_D\tau_D} + \sqrt{GRRC_D\Gamma} < n(t)a^*(t-\tau_R-\tau)e^{j(\omega-\omega_R)t} > e^{j\omega_R\tau_R} + \\
& < n(t)n^*(t+\tau)e^{j\omega t} > e^{j\omega\tau}\Big]
\end{aligned}$$

It is easy to show that the expected value of the signal with the noise is zero mean.

$$E\Big\{a(t-\tau_D)n^*(t-\tau)\Big\} = E\Big\{a(t-\tau_D)\Big\}E\Big\{n^*(t-\tau)\Big\} = 0 \tag{3.15}$$

From Equation 3.8 the auto-correlation of the noise term:

$$< n(t)n^*(t+\tau) >= N_O B sinc(2B\tau) \tag{3.16}$$

If we perform a time shift such that $t = t+\tau_D$ and define $\tau_{RD} = \tau_D - \tau_R$, $\omega_{RD} = \omega_D - \omega_R$ we get the following:

$$R(\tau,\omega) = G_{sys}\Big[G_D C_D R_s(\tau)\mathrm{e}^{\mathrm{j}(\omega_D+\omega)\tau} + G_R C_D \Gamma R_s(\tau)\mathrm{e}^{\mathrm{j}(\omega_R+\omega)\tau} + C_D\sqrt{G_D G_R \Gamma} R_s(\tau-\tau_{RD})\mathrm{e}^{\mathrm{j}\phi_{RD}}\mathrm{e}^{-\mathrm{j}\omega_R\tau} sinc\Big(\frac{\omega+\omega_{RD}\tau}{2\pi}\Big) + C_D\sqrt{G_D G_R \Gamma} R_s(\tau+\tau_{RD})\mathrm{e}^{-\mathrm{j}\phi_{RD}}\mathrm{e}^{-\mathrm{j}\omega_D\tau} sinc\Big(\frac{\omega-\omega_{RD}\tau}{2\pi}\Big) + N_0 B sinc(2B\tau) sinc\Big(\frac{\omega\tau}{2\pi}\Big) + \nu_0\Big] \quad (3.17)$$

ν_0 is a zero mean processes: $E\{\nu_0\} = 0$. $\mathcal{R}(\tau,\omega)$ has peaks located at $\tau = 0, -\tau_{RD}, +\tau_{RD}$ as shown in Figure 3.3.

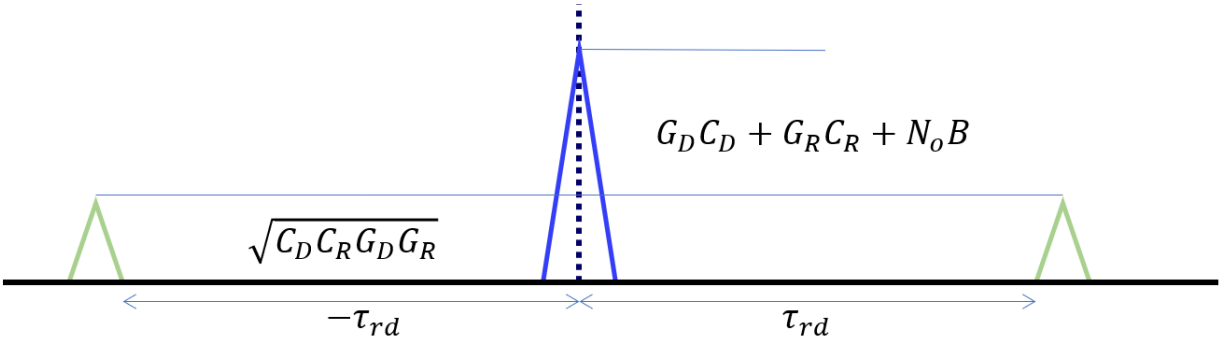

Figure 3.3. Auto-correlation Observable Graphic

Estimate of Reflectivity

Solving Eq 3.17 at $\tau = 0$ and $\tau = \tau_{RD}$:

$$R(0,0) = G_{sys}\Big[G_D C_D + G_R C_D \Gamma + kT_{sys}B + \nu_0\Big] \quad (3.18)$$

$T_{sys} = T_{FE} + T_A$

$$R(\tau_{RD},\omega_{RD}) = G_{sys}\Big[C_D\sqrt{G_D G_R \Gamma}\Big] + \nu_{RD} \quad (3.19)$$

Let

$$y_1 = \mathcal{R}(0,0) - G_{sys}kT_{sys}B \tag{3.20}$$

$$y_2 = R(\tau_{RD}, \omega_{RD})\mathrm{e}^{-\mathrm{j}\phi} \tag{3.21}$$

We defined the observable as:

$$d = \frac{y_1}{y_2} = \frac{1+\mathcal{R}^2}{\mathcal{R}} => \mathcal{R} = \frac{d}{2} \pm \sqrt{\left(\frac{d}{2}\right)^2 - 1} \tag{3.22}$$

$$d' = \frac{d}{2} = \frac{y_1}{2y_2} = \frac{1+\mathcal{R}^2 + \frac{\nu_0}{G_{sys}G_D^L C_D}}{2\mathcal{R} + \frac{2\nu_{RD}}{G_{sys}G_D^L C_D}} \tag{3.23}$$

Solving for $\mathcal{R}$

$$\mathcal{R} = d' \pm \sqrt{d'^2 - 1} \tag{3.24}$$

3.4 Onboard Instrument Calibration Network

The SNOOPI instrument has an onboard calibration network to obtain the estimates G_{sys}, N_0.

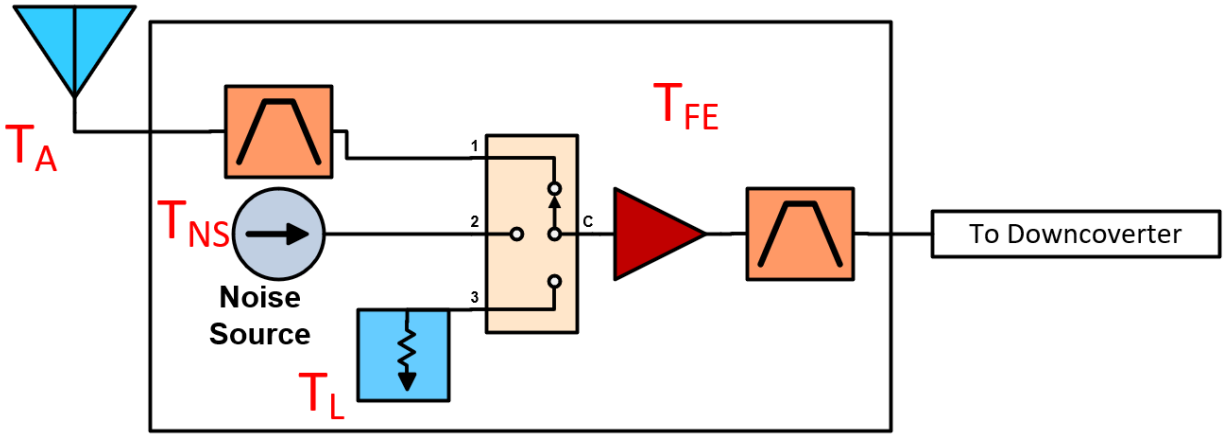

Figure 3.4. Calibration Source Notation

The digital receiver samples at $B_S = 50$ MHz. The LNFE has sharp filters before the digital receiver with the filter bandwidth less than the sampling bandwith.

Table 3.1. System Noise Sources Symbol Definitions

Source Name	**Symbol**
Antenna Noise Temperature	T_A
Matched Load Temperature	T_L
Noise Diode Temperature	T_{NS}
Front End Temperature	T_{FE}
System Noise Temperature	$T_{sys} = T_A + T_{FE}$

Matched Load

This mode disconnects the antenna from the LNFE and applies a matched load with to the system. The matched load has a temperature sensor to provide the equivalent noise temperature.

$$x(t) = \sqrt{G}\Big[\eta_L(t) + \eta_{FE}(t)\Big] \tag{3.25}$$

$$R_L(\tau, f) = G(T_L + T_{FE})kB_S sinc(2B\tau)sinc(fT) \tag{3.26}$$

$$R_L(0, 0) = G(T_L + T_{FE})kB_S \tag{3.27}$$

Noise Diode

This mode disconnects the antenna from the LNFE and connects a noise diode with known noise temperature T_{ND} to the input.

$$x(t) = \sqrt{G}\Big[\eta_{ND}(t) + \eta_{sys}(t)\Big] \tag{3.28}$$

$$R_{ND}(0, 0) = G(T_{ND} + T_{FE})kB_S \tag{3.29}$$

3.5 System Noise Estimates

Several noise sources must be estimated and removed to make the reflectivity estimate.

Galactic/Antenna Noise

Existing background universe noise maps for 408 MHz [27] will be used to empirically calculate T_A. To make this calculation, knowledge of the orbit and attitude of the spacecraft as well as the antenna patterns is required. Simulated gain patterns of the SNOOPI antennas.

Front End Noise Estimate

Then $\hat{G}_{sys}$ can be found from 3.27 and 3.29.

$$\hat{G}_{sys} = \frac{R_{ND}(0,0) - R_L(0,0)}{(T_{ND} - T_L)(kB_S)} \tag{3.30}$$

Then we get $\hat{T}_{sys}$ from either 3.27 or 3.29:

$$\hat{T}_{sys} = \frac{R_{ND}(0,0)}{\hat{G}_{sys} k B_S} - T_{ND} + \hat{T}_A \tag{3.31}$$

3.6 Onboard Calibration Precision

The precision on the estimate of Equation 3.31 is dependent on the integration time. For the full derivation of the uncertainty in temperature estimate as a function of integration time and bandwidth, see Appendix C. The error in the reflectivity estimate is a function of the precision of the calibration source and reflectivity. The propagation of error method was used to calculate the root square mean error of the reflectivity estimate.

The precision estimate for the noise diode and the matched load is a band-limited white Gausian process. When a square law detector (equivalent to signal energy in Equation 3.2, the error in the equivalent noise temperature measurement:

$$\Delta T \approx \frac{T}{\sqrt{B\tau}} \tag{3.32}$$

B is the system bandwidth, T is the equivalent noise temperature. Table 3.2 has details for each of SNOOPI's bands.

Table 3.2. Calibration Temperature Estimate Precision

Band	UFO	MUOS	Units
Bandwith	25 KHz	5 MHz	Hz
Matched Load Temperature	290	290	K
Noise Diode Temperature	1500	1500	K
Integration Time	1		ms
Matched Load Uncertainty	300	4.1	K
Noise Diode Uncertainty	58	21.2	K
Integration Time	10		ms
Matched Load Uncertainty	94.9	1.3	K
Noise Diode Uncertainty	18.3	6.7	K

The propagation of errors method was used to calculate the error in estimated reflectivity.

$$\Delta f = \left|\frac{df}{dx}\right| \Delta x \tag{3.33}$$

The reflectivity estimate, due to the error for the noise and signal sources:

$$\Delta\Gamma(R(0,0), R_{ref}, R_{ND}, T_A) = \sqrt{(\delta\Gamma/\delta R(0,0)\ \Delta R(0,0))^2\ \delta\Gamma/\delta R_{ref}\ \Delta R_{ref})^2 + (\delta\Gamma/\delta R_{ND}\ \Delta R_{ND})^2 + (\delta\Gamma/\delta T_A\ \Delta T_A)^2} \tag{3.34}$$

The standard deviation of the estimator for a signal with a known noise power is derived in Appendix C. The result is given as:

$$\sigma_s = \hat{P}_s \sqrt{\frac{1}{N_r}\left(1 + \frac{1}{S_N}\right)^2 + \frac{1}{N_n}\left(\frac{1}{S_n}\right)^2} \tag{3.35}$$

Where $N_r = B\tau_r$ is the integration time of the signal + noise condition and $N_n = B\tau_n$ is the integration time of the noise/calibration state.

The reflectivity estimate is re-written in terms of correlation values, of which the standard deviation can be estimated. Rewriting Equation 3.23:

$$d' = \frac{R(0,0) - \left(\frac{R_{ND}(0,0)(T_{ND}-T_{Ref})}{R_{ND}(0,0)-R_{ref}(0,0)} - T_{ND} - T_A\right)\left(\frac{R_{ND}-R_{Ref}}{T_{ND}-T_{Ref}}\right)kB}{2\sqrt{C_D C_R G_D G_R}} \tag{3.36}$$

Realistic values for $R(0,0), R_{ND}(0,0), R_{ref}(0,0)$ were estimated based off of knowledge of the DBE. The DBE uses 16 bit numbers for the lag 0 value. The estimated value for R_{ref} was set to $2^{12} - 1$. Equations 3.19, 3.29 are numerically solved for values of $R_N D$ and $R(0,0)$.

The partials of $\Delta\Gamma(R(0,0), R_{ref}, R_{ND}, T_A)$ were calculated using a computer symbolic algebra program [28]. It is assumed that the antenna noise figure will be ≈ 290 K and will have a 50 K error. Figures 3.5 show the uncertainty in reflectivity estimate for 370 MHz due to the system calibration source precision and surface reflectivity.

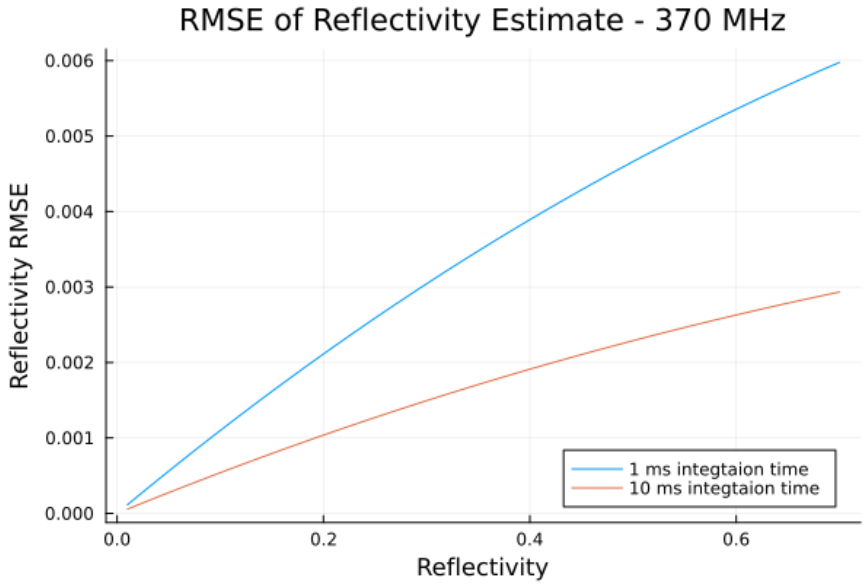

Figure 3.5. 370 MHz Band Error vs Reflectivity

The high error in the 255 MHz signal is due to the low bandwidth (25 kHz) of the signal source. Figures 3.6 shows the error in reflectivity for the 255 MHz band.

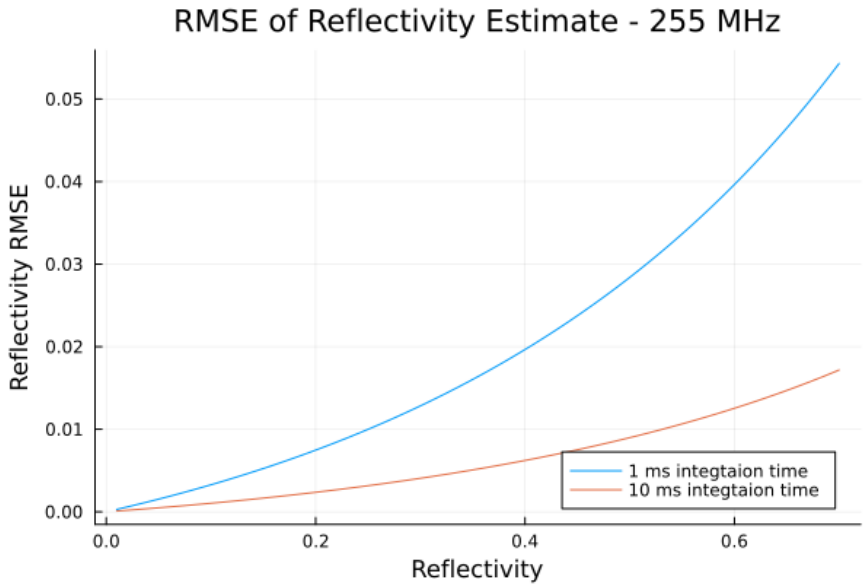

Figure 3.6. 255 MHz Band Error vs Reflectivity

4. SAMPLE LEVEL SIMULATOR

To assist in the SNOOPI instrument and algorithm deign, a sample-level simulators was developed to numerically validate the analytical model of the spaceborne reflectivity estimation. The simulator was built leveraging existing work from a simpler simulator designed for SoOp flight campaigns [18]. The simulator uses output from the SNOOPI orbit prediction software to generate DDMs [29]. A synthetic (complex) QPSK signal is generated from a uniform random variable, simulating the P-Band source. The appropriate path delays, loses and Doppler shifting is applied to the signal. The simulator also applies antenna gains, system noise, and front end filtering to the signal. The simulator generates complex DDMs from which the observables are extracted. Figure 4.1 has a graphical overview of the simulator.

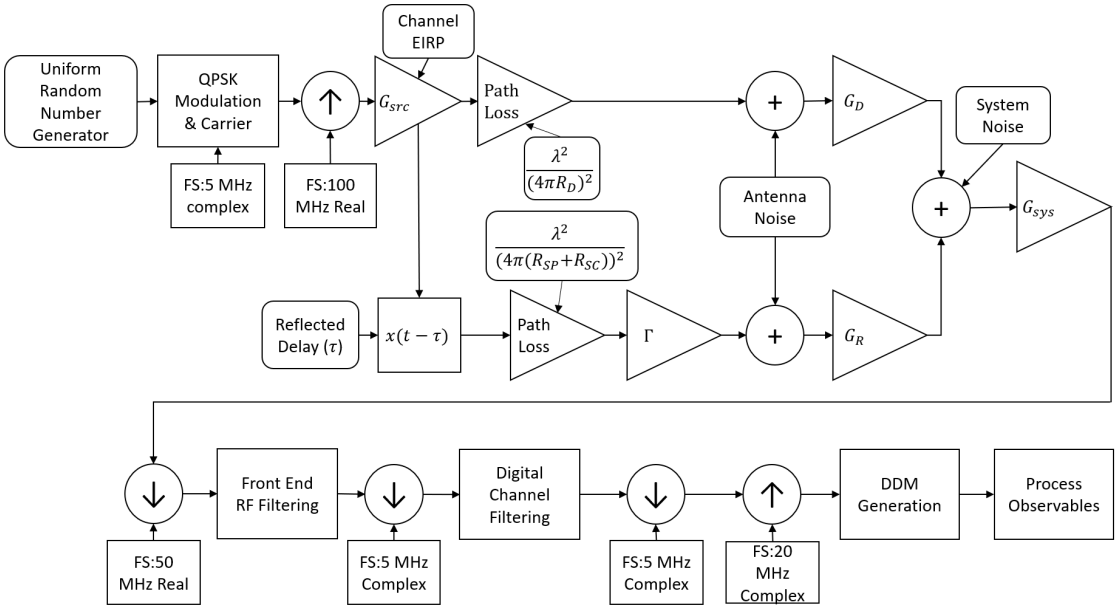

Figure 4.1. Graphical Representation of Simulator

4.1 Simulator Description

The simulator generates a synthetic signal vector

$$x[n] = \sum_{k=1}^{K} s_k[n] \mathrm{e}^{-\mathrm{j}\omega_k n} \tag{4.1}$$

where s_k is an individual channel in a communication system spectra with carrier frequency ω_k. $x[n]$ is simulated at the transmitter with ω_k being the carrier of the transmitter without any Doppler shifting applied. Each $s_k[n]$ is generated as a complex signal at the bandwidth of the channel, filtered using a Root Raised Cosine filter and the up-sampled to 100 MHz and converted to the real domain. An example of a simulated MUOS spectrum before the addition of system thermal noise is shown in Figure 4.2a. Figure 4.2b is the simulated PSD as received by the SNOOPI front end, accounting for path losses, antenna gains, and system noise. The lowest frequency MUOS channel is increased by 6 dB for visualization purposes.

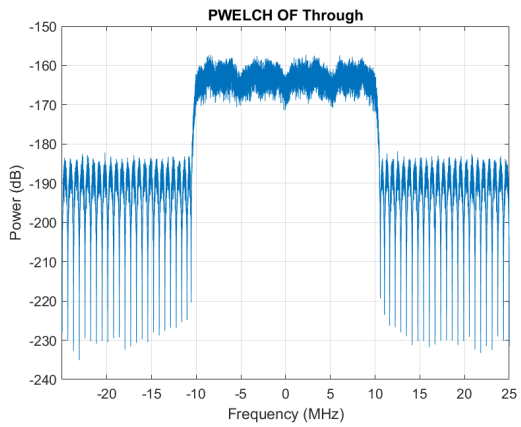

(a) Simulated MUOS Power Spectral Density - without system noise

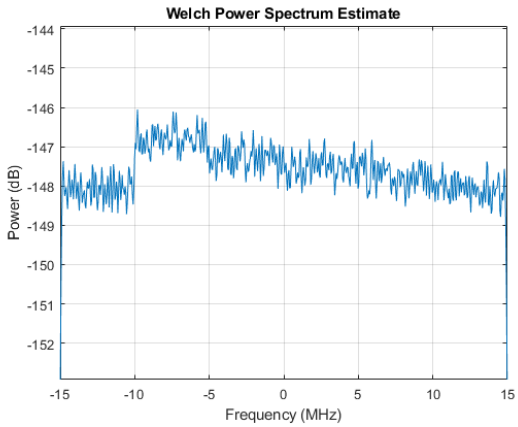

(b) Simulated MUOS Power Spectral Density - with system noise

Figure 4.2. Simulated MUOS Spectrum

Variable Definitions

Note, for the purposes of the simulator, $N_{offset} = N_{RD}$ but this will not be true for a spaceborne instrument. The SNOOPI mission has an error budget of $N_{offset} < \pm 25$ samples to accpunt for errors between the N_{RD} estimate and the true N_{offset}. This error budget set the DDM delay and frequency size for the SNOOPI instrument.

Following the derivation in Section 3.3, the simulator models the received signal as:

Variable	Definition
FS	Sampling Frequency
N_{int}	Number of samples to integrate
N_{RD}	Discretized (true) τ_{RD}
N_{offset}	Estimated signal delay for DDM generator
$x[n]$	The signal as received by the instrument
$x_{buff}[n]$	The buffer in the digital receiver
$x_1[n]$	Component 1 for the correlation, $x_{buff}[n]$ for n = 0 to N_{int}
$x_2[n]$	Component 2 for the correlation, $x_{buff}[n]$ for n = N_{offset} to $N_{offset} + N_{int}$
N_{buff}	Number of samples in buffer $N_{buff} > N_{int}$

$$x(t) = \sqrt{G_{sys}}\left[\sqrt{G_D C_D}a(t-\tau_D)\mathrm{e}^{\mathrm{j}\omega_D(t-\tau_D)} + \sqrt{G_R C_R}a(t-\tau_{RD})\mathrm{e}^{\mathrm{j}\omega_R(t-\tau_R)} + \eta_{sys}(t)\right] \quad (4.2)$$

ω_D, ω_R are the Doppler frequency shift due to the relative motion of the spacecrafts and specular point. τ_D, τ_R are continuous time. For the delay of the signal modulation $a(t-\tau)$, these variables are converted to discrete time via:

$$\tau[n] = floor\left(\frac{\tau}{FS}\right)$$

To account for the carrier phase delay, $\mathrm{e}^{\mathrm{j}\omega(t-\tau)}$, the complex variable ϕ is defined as:

$$\phi = \mathrm{e}^{\mathrm{j}2\pi\omega\tau}$$

η_{sys} is simulated by a random number generator following a zero mean Gaussian distribution with variance the power of the system noise.

Practically in the simulator, $\tau_D = 0$ when simulating $x[n]$; there is no need to simulate bits that are not used in the simulation. The discrete time equivalent of 3.3 is given as:

$$x[n] = \sqrt{G_{sys}}\left[\sqrt{G_D C_D}a[n]\mathrm{e}^{\mathrm{j}2\pi\omega_D[n/FS]}\phi_D + \sqrt{G_R C_R}a[n-N_{RD}]\mathrm{e}^{\mathrm{j}\omega_R[n/FS]}\phi_R + \eta_{sys}[n]\right] \quad (4.3)$$

$x[n]$ is a real domain signal, sampled at 100 MHz. A 20 MHz band-pass filter is applied to $x[n]$ to simulate the front end RF filters.

4.2 Digital Back End Simulation

At this point the signal is an approximation of the output of the RF frontend before digitization. The signal is complex sampled at 50 MHz, simulating the down conversion and discrete sampling. The signal is further filtered to select the channel(s) of interest and down sampled before correlation. Table 4.1 summarizes the SNOOPI DBE DDM size and processing bandwidths. Note, the SNOOPI DBE (and therefore the simulator) upsamples the RF data before correlation by a factor of 4 to allow for a better estimate of the true reflected peak delay τ_{RD}. The simulators DDM generator is user programmable and for visualization purposes, the DDMs shown below have increased Doppler resolution.

Table 4.1. SNOOPI DBE Summary

Signal Band	255 (UFO)	370 (MUOS)
Channel Bandwidth	5 KHz	5 MHz
Number of Channels	5	1
Aggregate Bandwidth	25 KHz	5 MHz
Chip Length	12 km	60 m
Delay Resolution	60 m	15 m
Delay Bins	5	200
Doppler Bins	3	3

For the simulator, $x[n]_{buff}$ is a complex signal sampled at 50 MHz, simulating the output from the A to D. A DDM is generated is generated via non-circular correlation. Simulating the SNOOPI instrument the simulator correlated 1 ms blocks and outputs a complex map. A modified time-domain discrete auto-correlation function is defined as:

$$Y(k + N_{offset}, f) = \frac{1}{N_{\text{int}}} \sum_{n=0}^{N_{int}} x_{buff}[n] x^*_{buff}[n + k + N_{offset}] \mathrm{e}^{2\pi f \mathrm{j}[n/FS]} \tag{4.4}$$

Note that, $N_{offset} > 0$, the length of $x_{buff} \geq N_{\text{int}} + N_{offset}$

An computationally efficient method of correlation is performed using the Fast Fourier Transform (FFT). To perform a non-circular correlation using FFTs, the DDM correlation matrix R is formed as:

1. Take N_{int} number of samples to correlate and pad with N zeros. Name this vector X_1
2. Advance N_{offset} samples into the data and select N_{int} samples and pad with N zeros. Name this vector X_2
3. Create a vector of length $2N_{int}$ for complex sinusoidal Doppler shift $e^{j2\pi f_D[n/FS]}$
4. Multiple $FFT(X_1)$ and the conjugate of $FFT(X_2 * e^{j2\pi f_D[N/FS]})$.
5. Take IFFT of result from 4 and save in appropriate row of R matrix.
6. Repeat steps 3 through 6 for number for each Doppler row in the matrix R.

The DDM matrix R from this algorithm:

$$\mathcal{R}[\tau, f_D] = \frac{1}{N_{int}} \begin{bmatrix} IFFT\Big(FFT(X_1) * FFT^*(X_2 * e^{-j2\pi f_D[n/FS]})\Big) \\ ... \\ IFFT\Big(FFT(X_1) * FFT^*(X_2 * e^{j2\pi f_D[n/FS]})\Big) \end{bmatrix} \tag{4.5}$$

An example of simulated DDMs for the MUOS band is shown in Figure 4.3. DDMs of the data were generated with integration time of 5 ms, Doppler range of ±1500 hz and a delay range of ±20 samples. The direct gain is 0 dBi and the reflected gain is -3 dBi, with a 1 ms integration time. The DDM dimensions were chosen for visualization purposes.

An example of the MUOS band SNOOPI DDM is shown in Figure 4.4.

4.3 Expected System Performance

We define a SNR metric to give a measure of detectability of the reflected peak against the noise background:

$$\text{SNR} = \frac{< |\mathcal{R}[\tau_{rd}, f_D]| >}{\text{STD}\Big(\mathcal{R}[\tau_{rd}, f_D]\Big)} \tag{4.6}$$

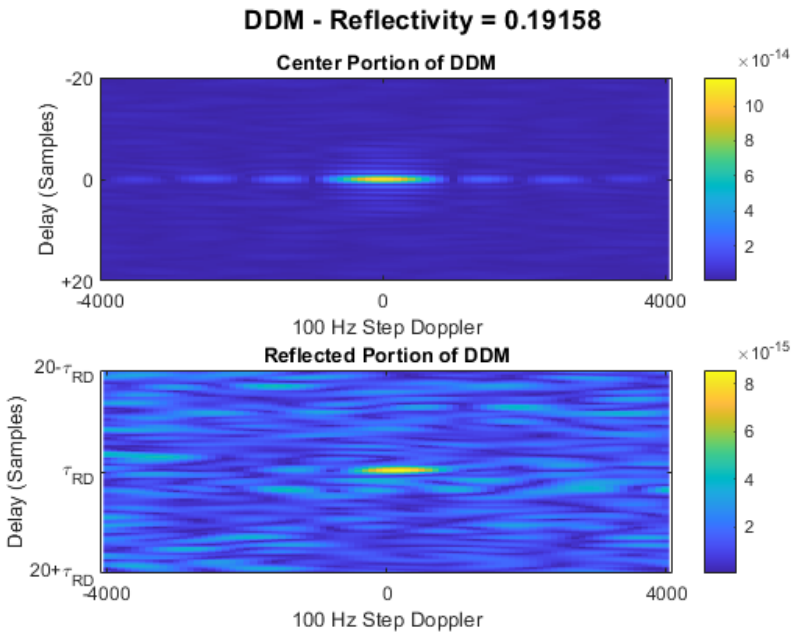

Figure 4.3. Example Single 5 MHz channel DDM Simulation

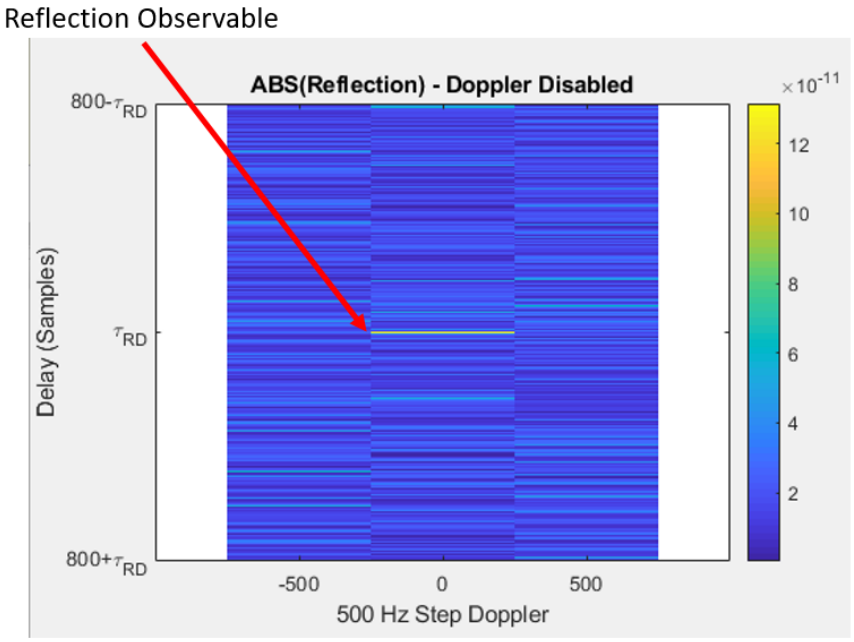

Figure 4.4. Example SNOOPI DDM Simulation

STD is the standard deviation operator. Figure 4.5 shows the signal detectability with 1 ms integration. Figures 4.5 and 4.6 estiamte the standard deviation of the Phase Estiamte and Reflectivity Estimate.

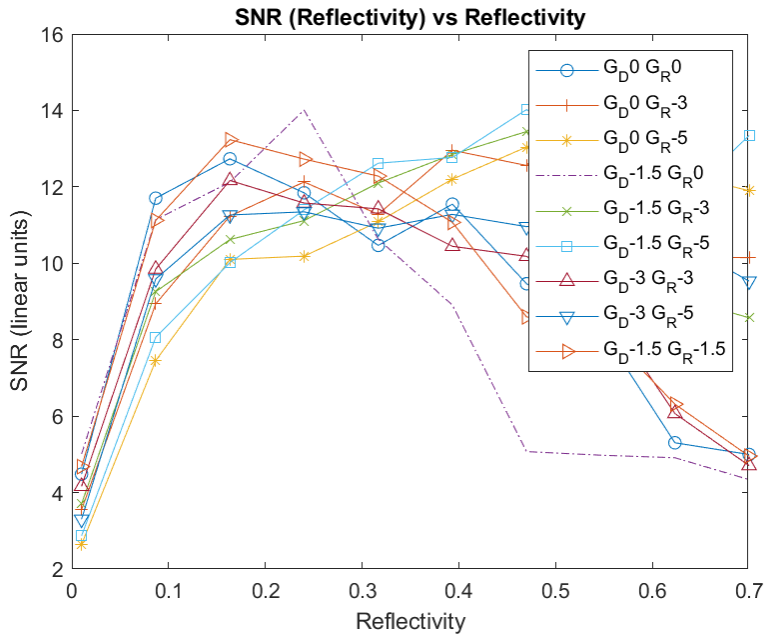

Figure 4.5. Estimated SNR vs. Reflectivity

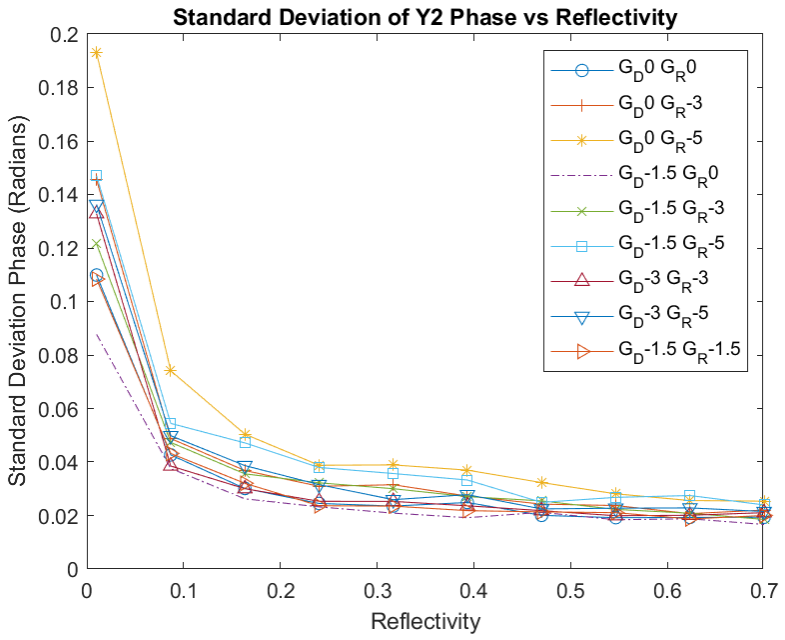

Figure 4.6. Standard Deviation of Estimated Phase vs Reflectivity

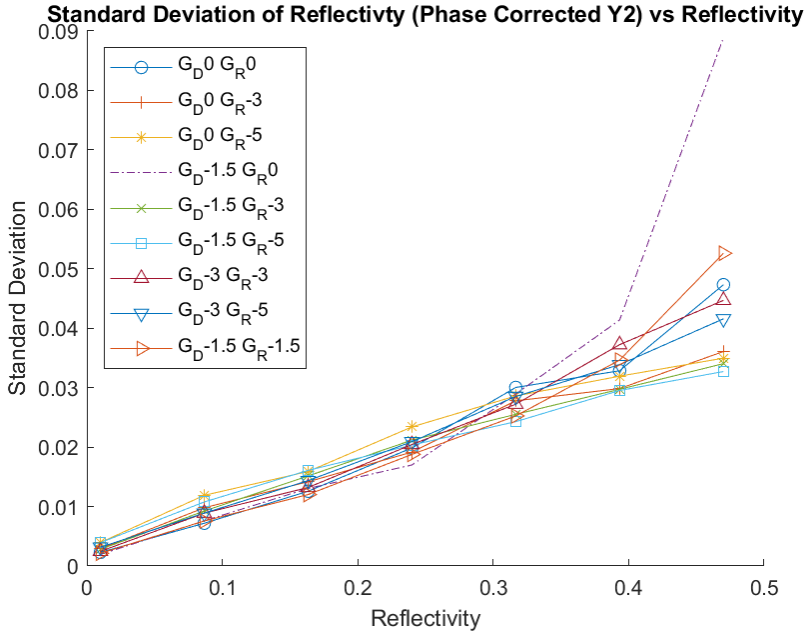

Figure 4.7. Standard Deviation of Estimated Reflectivity

5. WYATT-EIRP MONITORING SYSTEM

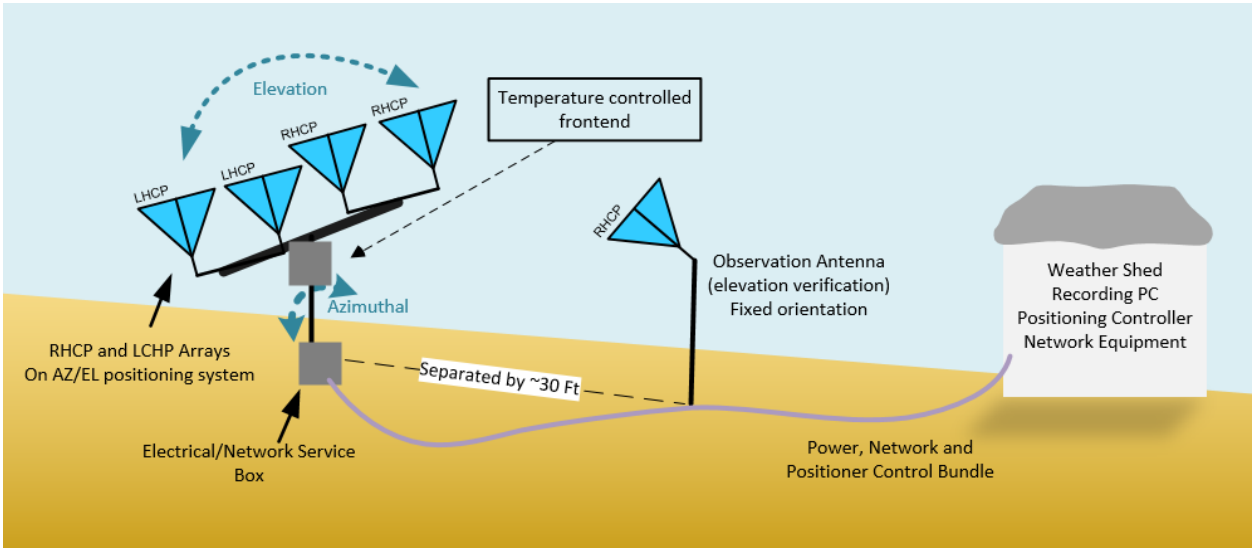

Figure 5.1. WYATT-EIRP Station Graphic

To support the SNOOPI spaceborne instrument, a ground monitoring station of the P-Band SoOp transmitter source has been designed. The WYATT-EIRP (Wide-band Year-long Ambiguity-function Transmission Tracking Effective Isotropic Radiated Power) system incorporates onboard calibration methods similar to a GPS EIRP monitoring station [30], [31], an active-cold load [32], as well as techniques developed in other Signals of Opportunity instruments [33], [17]. WYATT-EIRP is designed for the following items:

1. LHCP and RHCP wide bandwidth RF recording of the 255 and 370 MHz P-Band SoOp sources

2. Periodic monitoring of P-Band transmission sources EIRP and self-ambiguity functions

3. 360x180 sky scanning mode for background noise monitoring

4. P-Band SoOp transmitter source orbit elevation verification

The system will periodically collect wide-band RF recording of the P-Band transmitter source. This data will be processed to produce a EIRP estimate, self-ambiguity function

and orbit elevation data product. The system will have three primary operating modes, summarized in Table 5.1. The data storage requirements are shown in Table 5.2.

Table 5.1. WYATT-EIRP Recording Modes

Name	Recording Length	Frequency
Snapshot	1 minute	4x daily
Overpass Monitoring	15 minutes	1-2x weekly
Skyscannign Mode	1 hour	2x monthly

Table 5.2. WYATT-EIRP System Data Requirements

	255 MHz	370 MHz	Total	Units
RF Bandwidth	30	20	50	MHz
Sampling Rate	40	30	70	MHz
Mega Bytes/Second	160	120	280	MB/s
Source Snapshot (30 sec)	4.8	3.6	8.4	GB
SNOOPI Overpass (15 minutes)	144	108	252	GB
Sky Scanning Mode (1 hour)	576	432	1008	GB

5.1 Location

Several locations around Purdue University were evaluated for the WYATT-EIRP system installation. It was determined that installing the system on a roof of a building on campus or in the West Lafayette area would be at a higher risk for RFI. Several locations did not have a clear view of the sky for sky scanning mode e.g., locations with dense trees or hilly elevations. Purdue ACRE was chosen as the installation location is over a half-mile from the nearest subdivision and over 3 miles from Purdue's main campus.

5.2 Hardware Description

The WYATT-EIRP system consists of an azimuthal and elevation actuating antenna pedestal with 2, 2-element array antennas. The temperature controlled front end is mounted

Figure 5.2. WYATT-EIRP Station Location

on the actuating pedestal to minimize movement of the coaxial feed lines between the antenna and the low noise front end. There is a secondary "observation" antenna located approximately 35 ft north from the actuating pedestal. The temperature controlled front end has an optical data connection to the nearby weather shed for communication with the USRP control computer. The data shed also contains the antenna pedestal controllers, computer network equipment and data recorder server for the instrument. The system also features two internet accessible cameras for monitoring the antennas. The server, cameras and various controllers are placed behind an edge router, connected to Purdue internal network.

5.2.1 Antenna Description

The antennas are COTS helix antennas designed to operate in 225-400 MHz. A single helix antenna has 8 turns with a 96" long boom. The 2 element vertically stacked antennas,

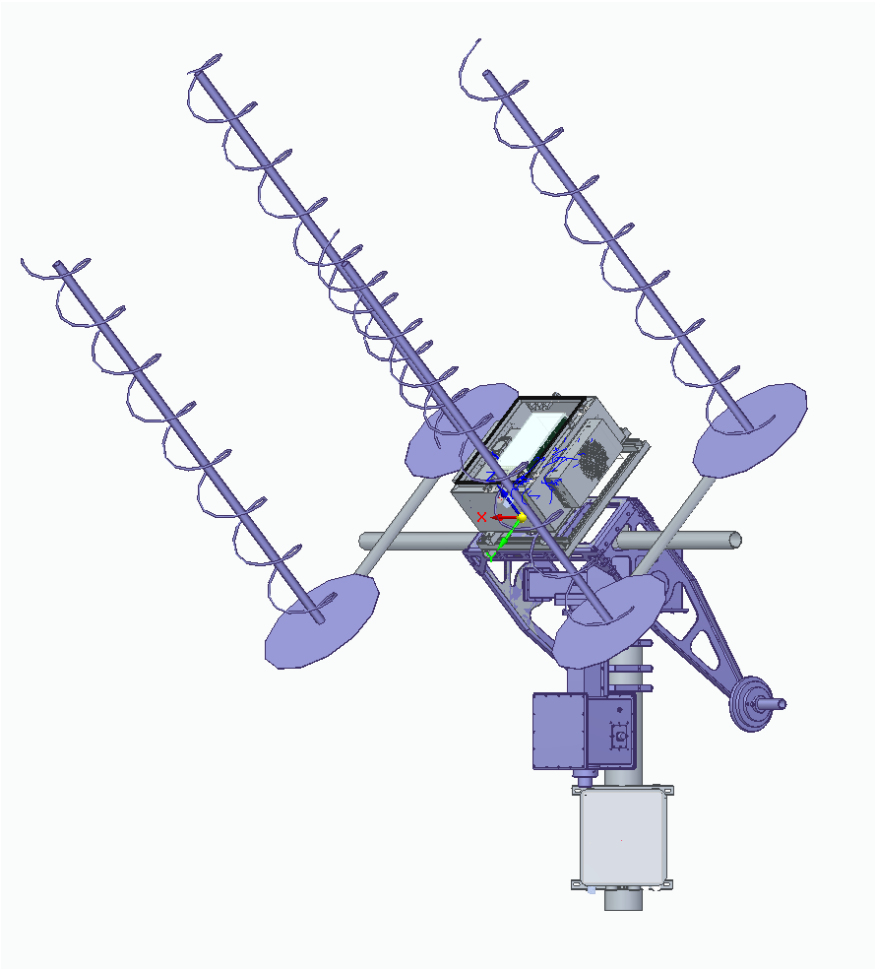

Figure 5.3. Antenna Arrays on Pedestal Rendering

36" arrays were chosen to create a narrower vertical gain pattern than a single helical antenna. This also had the benefit of decreasing the amplitude of the gain pattern's side lobes in the vertical plane which is desirable to isolate the direct signal from ground reflections. Gain patterns were simulated in Open EMS [34]. Patterns for both the single antenna and the 2-element antenna array shown in Appendix A, Figures A.1 and A.2. The pedestal and reference antennas were installed on pipes mounted in concrete bases.

Figure 5.4. Antenna Arrays (before front end install)

5.2.2 Reference Antenna Location

The reference antenna will be located approximately 35 ft north of the pedestal. RG-400 and CAT-6A is buried in a conduit between the reference antenna and the pedestal for the RF signal and the network camera respectively.

Table 5.3. WYATT-EIRP Antenna Parameter Summary

Parameter	**255 MHz**	**370 MHz**	**Units**
Single Antenna			
Gain	8.8	11.5	dBi
Cross Polarization Isolation	28	17	dB
Antenna Array			
Gain	11.6	14.66	dBi
Cross Polarization Isolation	29	17	dB

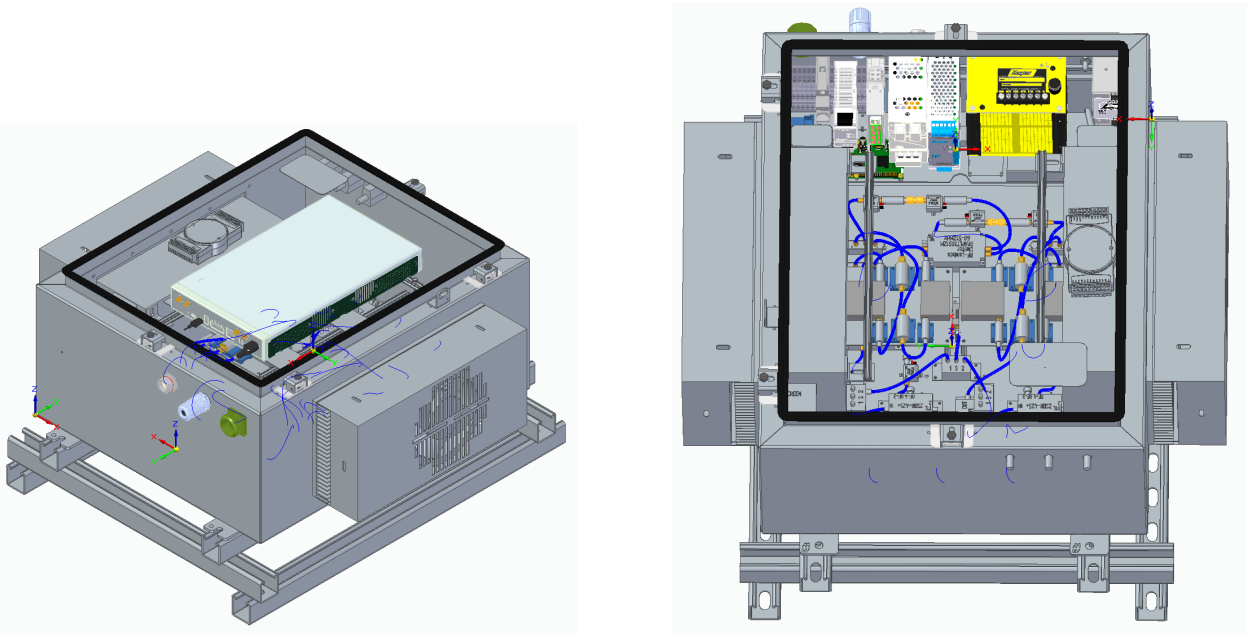

(a) Top View Of Front End

(b) Internal View CAD

Figure 5.5. Front End Enclosure Rendering

5.3 Microwave Instrument Description

The microwave instrument was designed to allow simultaneous recording of LHCP and RHCP signals. A block diagram of the front end is shown in Figure 5.7. The band-pass filters are identical to the RFI filters in the SNOOPI LNFE.

Switches

Pin diode switches were chosen for the coaxial switches for their scattering parameter stability in comparison to mechanical switches. Even though mechanical switches have lower insertion loss, they wear over time changing their insertion loss and scattering parameters. Mechanical switches S21 parameters also vary in the order of ≈ 0.1 dB between each switching instances.

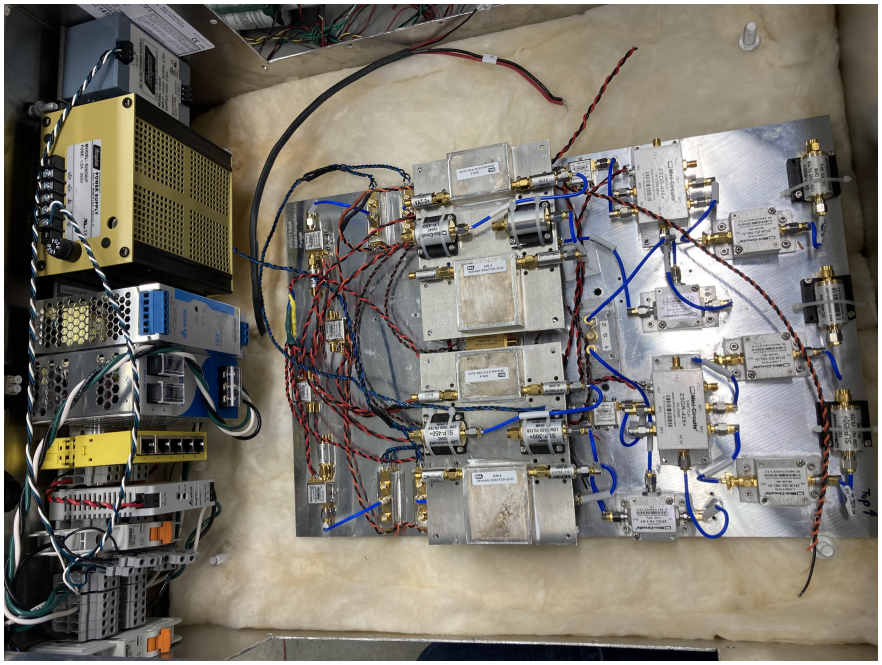

Figure 5.6. Partially Assembled Front End in Enclosure

Calibration Network

Three calibration sources are present in the front end: a matched load, an active cold FET (Field-effect Transistor), and a noise diode. The active cold FET should provide a equivalent noise temperature of ≈ 60 K. The system has a single noise diode, shared between the two channels via a power splitter. This allows for a common signal source between the two chains. The noise diode is also coupled into the chain, allowing for multiple calibration points.

The digital recorder is an Ettus N300 USPR unit serving as the down converter and analog to digital sampler. This unit features two independently tuneable RF inputs, allowing for simultaneous recording of the 255 MHz and 370 MHz bands.

5.3.1 Front End Location Placement

The front end enclosure was placed on the antenna actuator portion to eliminate any bending of the coaxial feed lines between the antenna array and the front end. The RF

Table 5.4. EIRP Front End Parameters

	255 MHz	**370 MHz**	**Units**
EIRP (Single Channel)	26	37	dBW
Channel Bandwidth	25	30000	kHz
Free Space Path Loss	172	175	dB
Power At Antenna	-140	-132	dBm
Antenna Array Gain	11	15	dBc
Antenna Est Noise Temperature	5	5	K
Frontend Gain	50.7	45.4	dB
Receiver Noise Temperature	124.8	114.7	K
Expected SNR	28.45	17.2	-
1 dB Compression Point	-74	-70	dBm
Cold Load Temperature	≈ 60	≈ 60	K
Noise Diode Temperature	1540	1540	K

digital back end (USRP N300) is placed in the front end enclosure to digitize the signal. Optical fiber connected the USRP to the server in the weather shed.

5.3.2 Thermal Control

A requirement for system front end gain stability drove the decision to thermally control the front end. Due to the decision that the front end will move with the antenna array, thermometric cooling/heating modules where chosen for this design. The most thermally sensitive components including the calibration network and amplifiers are placed on a cold plate, a TIC-6 aluminum sheet thermally coupled to a cold plate thermometric cooler. The entire front end box is thermally controlled via 2x 515 BTU/HR thermometric blown-air air conditioners. The cold plate and air conditioner units also have build in heating elements, allowing for temperature stability in the winter months.

The cold plate module protrudes out the rear of the front end box as shown in Figure 5.5. This allows for the heat to be displaced outside the box, lowering the thermal load on the blown-air air-conditioners. A summary of the thermal load and thermoelectric cooling potential is shown in Table 5.6.

It is planned to have 2 or 3 temperature set points for the front end to accommodate the change in the outdoor weather temperature as shown in Table 5.5. This is primarily to reduce the strain on the heating elements during the winter months.

Table 5.5. Front End Temperature Set Points

Season	**Set Point**
Summer	26 C
Spring/Fall	10 C
Winter	0 C

Table 5.6. Front End Thermal Summary

Microwave Componets	74	BTU/HR
USRP	273	BTU/HR
Sun + Max Ambient Load	136	BTU/HR
Other	170	BTU/HR
Total Heat Load	653	BTU/HR
Blown Air Cooling Capacity	1060	BTU/HR
Delta C from Ambient	-15	Δ C

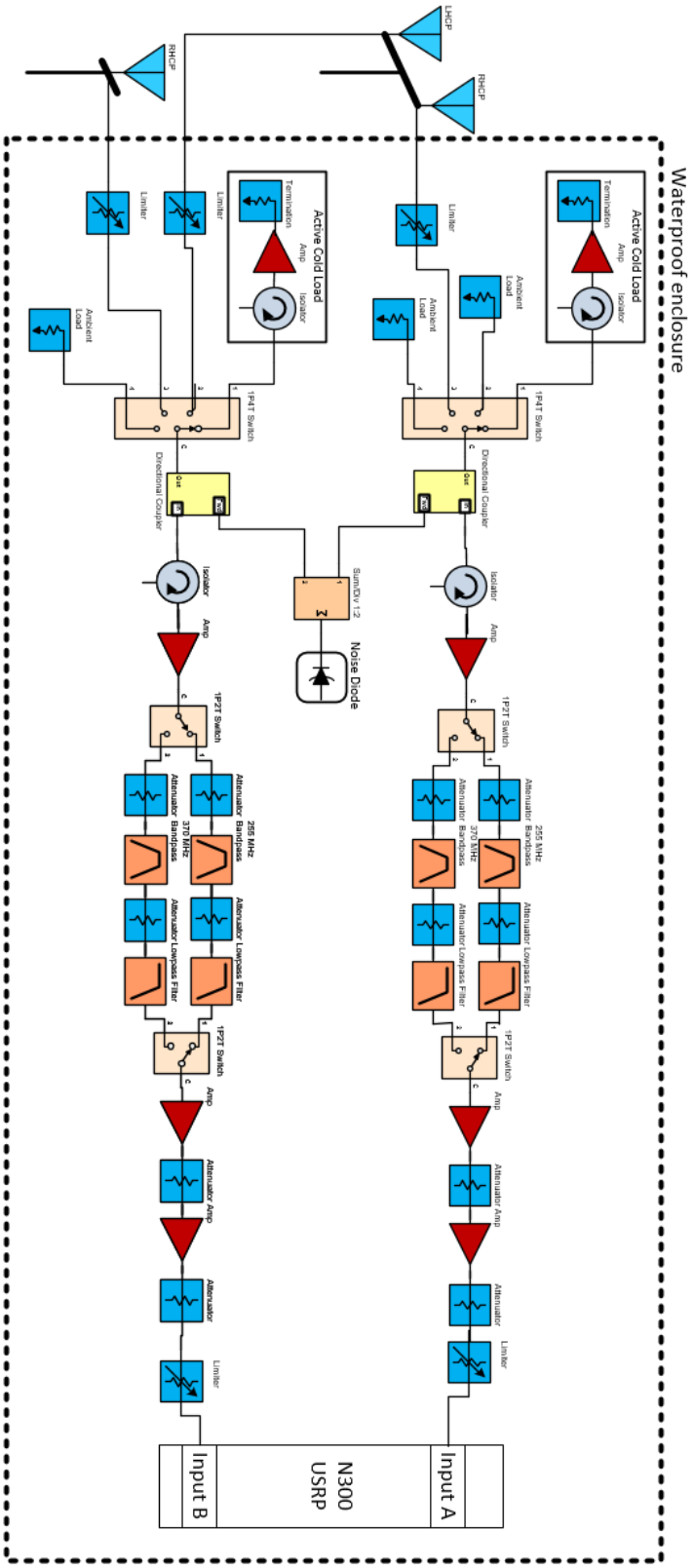

Figure 5.7. EIRP Microwave Block Diagram

5.4 Power Observable Derivation

The WYATT-EIRP system is assumed to have a narrow main beam antenna with sensitivity in the ground reflection direction. This derivation follows the derivation in 3.3 with a few simplifications.

1. The only Doppler frequency shift will be due to the motion of the transmitter.
2. A reflection will occur and due to the low antenna height from the ground, the reflected peaks will be within the auto-correlation function.
3. The reflection coefficient is a complex variable
4. The cross-polarization isolation of the antennas are sufficiently high to ignore any cross-polarized components of the signal.

The signal from the front end follows the same derivation as in Equations 3.13 - 3.17. Since the tower is stationary, the only Doppler shift present is due to the motion of the satellite, which is negligible for our transmitter. $\omega_D = \omega_R = \omega_C$. We also can make the assumption that the delay from the ground reflection is only a few meters, allowing for $C_R \approx C_D$. This also has the consequence of causing the reflection to be within the main support of the $\tau = 0$ auto-correlation as shown in Figure 5.8 The auto-correlation result is provided here again:

$$\begin{aligned} R(\tau,\omega) = G_{sys}\Big[& G_D C_D R_s(\tau)\mathrm{e}^{\mathrm{j}\omega\tau} + G_R C_D \mathcal{R}^2 R_s(\tau)\mathrm{e}^{\mathrm{j}\omega\tau} + \\ & C_D\mathcal{R}\sqrt{G_D G_R}R_s(\tau-\tau_{RD})\mathrm{e}^{\mathrm{j}\phi_{RD}}\mathrm{e}^{-\mathrm{j}\omega_R\tau}sinc\Big(\frac{\omega+\omega_C\tau}{2\pi}\Big) + \\ & C_D\mathcal{R}\sqrt{G_D G_R}R_s(\tau+\tau_{RD})\mathrm{e}^{-\mathrm{j}\phi_{RD}}\mathrm{e}^{-\mathrm{j}\omega_D\tau}sinc\Big(\frac{\omega-\omega_C\tau}{2\pi}\Big) + \\ & + kT_{sys}Bsinc(2B\tau)sinc\Big(\frac{\omega\tau}{2\pi}\Big) + \nu_0\Big] \end{aligned} \quad (5.1)$$

Invoking the auto-correlation's even-function property per Equation 3.6:

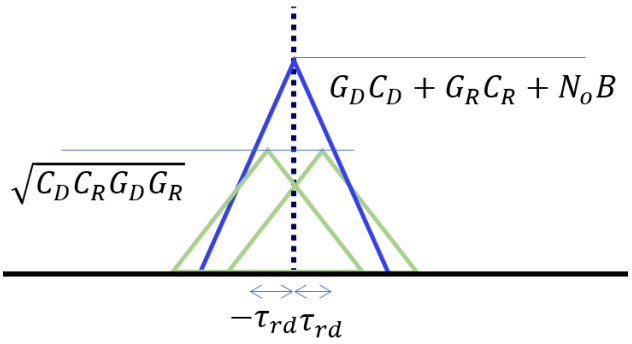

Figure 5.8. Short τ_{RD} autocorrelation

$$\left(C_D\mathcal{R}\sqrt{G_D G_R}R_a(\tau-\tau_{RD})\mathrm{e}^{\mathrm{j}(\omega_c+\omega)\tau}\right)^* = C_D\mathcal{R}^*\sqrt{G_D G_R}R_a(\tau+\tau_{RD})\mathrm{e}^{-\mathrm{j}(\omega_c+\omega)\tau} \tag{5.2}$$

Furthermore,

$$\mathcal{R}^*R_a(\tau-\tau_{RD})\mathrm{e}^{\mathrm{j}(\omega_c+\omega)\tau} + \mathcal{R}R_a(\tau+\tau_{RD})\mathrm{e}^{-\mathrm{j}(\omega_c+\omega)\tau} = 2R\mathrm{e}\Big(\mathcal{R}\mathrm{e}^{\mathrm{j}\omega(-\tau_{RD})}R_a^*(-\tau)\Big) \tag{5.3}$$

The main observable reduces to:

$$\begin{aligned}\mathcal{R}(\tau,\omega) = G_{sys}\Big[&C_D G_D R_a(\tau)\mathrm{e}^{\mathrm{j}\omega\tau} + \mathcal{R}^2 C_D G_R R_a(\tau-\tau_{RD})\mathrm{e}^{\mathrm{j}\omega\tau} \\ &+2C_D\sqrt{G_D G_R}R\mathrm{e}\Big(\mathcal{R}\mathrm{e}^{\mathrm{j}\omega(\tau-\tau_{RD})}R_a^*(\tau-\tau_{RD})\Big) \\ &+ kT_{sys}Bsinc(2B\tau) + \nu_0\Big]\end{aligned} \tag{5.4}$$

Solving at $\tau = 0$ and $\omega = 0$ we get an observable Y_1:

$$\begin{aligned}R(0,0) = G_{sys}C_D G_D\Big[1 + \frac{G_R}{G_D}\mathcal{R}^2 + 2\sqrt{\frac{G_R}{G_D}}R\mathrm{e}\Big(\mathcal{R}\mathrm{e}^{\mathrm{j}\omega(-\tau_{RD})}R_a^*(-\tau_{RD})\Big)\Big] \\ + G_{sys}kT_{sys}B + \nu_0\end{aligned} \tag{5.5}$$

To add another layer of complexity, the transmitter has ≈ 8 degree elevation change over a 24 hour period. Returning to our assumption that the reflected signal is mostly reversed polarized, Figure 5.9 shows the RHCP (direct) and LHCP (reflected) gain patterns. The array spacing was chosen to optimize the width of the nulls at the reflected angle.

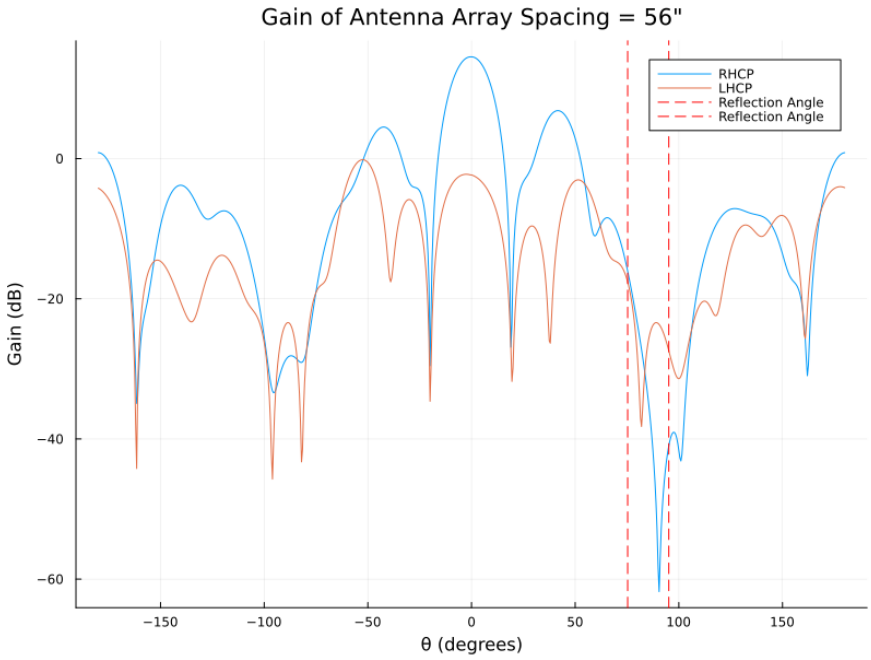

Figure 5.9. Gain Pattern for 56" Array Spacing

Assuming the antenna array phase center is 1.5 m above the ground, Figure 5.10 shows the error in EIRP estimate (in dB units) as a function of transmitter elevation.

The measurement will have an error that is dependent on the antenna gain towards the reflection. Under the condition when when the transmitter is at approximately 39 Deg elevation, the $G_R\, G_D$ terms are negligible. C_D is solved via:

$$C_D = \frac{1}{\hat{G}_D}\left[\frac{\mathcal{R}(0,0)}{\hat{G}_{sys}} - k(\hat{T}_{FE} + \hat{T}_A)B\right] \tag{5.6}$$

G_D is found via the antenna simulations, $\hat{G_{sys}}$ and $\hat{N}_0$ are estimate from the calibration states as discussed in section 5.6.

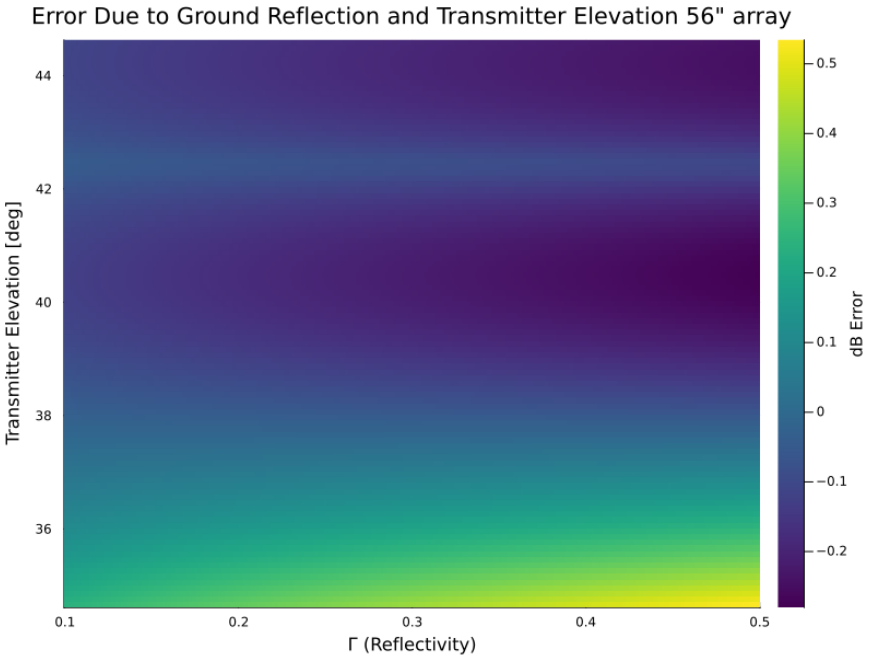

Figure 5.10. Error in EIRP estimate due to ground reflection

5.5 Phase Observable Derivation

Both the observation antenna and the pedestal array will be used for this measurement. Assume any phase difference between the front end chains is known and has been factored out.

$$x_1(t) = \sqrt{G_{sys,1}}\left[\sqrt{G_{D,1}C_D}a(t-\tau_D)\mathrm{e}^{\mathrm{j}\omega_D(t-\tau_{D1})} + \eta_1(t)\right] \tag{5.7}$$

$$x_2(t) = \sqrt{G_{sys,2}}\left[\sqrt{G_{D,2}C_D}a(t-\tau_D)\mathrm{e}^{\mathrm{j}\omega_D(t-\tau_{D2})} + \eta_2(t)\right] \tag{5.8}$$

The cross-correlation operator is defined as:

$$R_{12}(\tau) = \int_{-T/2}^{T/2} x_1(t)x_2^*(t-\tau)dt \tag{5.9}$$

Cross-correlating $x_1(t)$, $x_2(t)$:

$$R_{12}(\tau) = \sqrt{G_{sys,1}G_{sys,2}}C_D\sqrt{G_{D,1}G_{D,2}}\Big[R_{12}(\tau)\mathrm{e}^{\mathrm{j}\omega_D(\tau_{D2}-\tau_{D1}+\tau)} + \nu_0\Big] \tag{5.10}$$

The phase can be retrieved by solving when $\tau = 0$

$$\angle R_{12}(0) = \mathrm{e}^{\mathrm{j}\omega_D(\tau_{D2}-\tau_{D1})} \tag{5.11}$$

5.6 Calibration State Observable

The instruments ability to couple in the noise diode allows for several calibration points, summarized in Table 5.7.

Table 5.7. Designed Calibration Source Temperatures

Cold	60	K
Ref	270	K
Noise Diode	1540	K
Cold + Noise	1600	K
Ref + Noise	1810	K

The calibration state signal can be modeled as:

$$x(t)_{C,n} = G_{sys}(\eta(t)_{cal,n} + \eta(t)_{FE}) \tag{5.12}$$

Where $\eta(t)$ is a band-limited white Gaussian processes with a variance the power of the noise source.

The discrete-time auto-correlation is defined as:

$$\mathcal{R}[k] \ = \Big\langle x[n]x^*[n-k]\Big\rangle_T \tag{5.13}$$

is applied to this signal:

In post-processing the auto-correlation operator will be applied to this signal and solved at $k = 0$:

$$R_{Cal,n} = G_c(T_{cal,n} + T_{FE})kB \tag{5.14}$$

Where $R_{C,n}$ is the nth calibration source listed in Table 5.7. $R_{C,n}$ is the power of the signal $G_c = G_{sys}C$ accounts for the system gain and a conversion factor C which converters the physical units of Watts to digital counts of the integration $R_{C,n}$.

There are 5 calibration sources in total, but for any 2 sources, we can solving for G_c via:

$$G_c = \frac{R_{Cal,2} - R_{Cal,1}}{T_{Cal,2} - T_{Cal,1}} \tag{5.15}$$

Solving for T_{FE}:

$$T_{FE} = \frac{R_{Cal,1}}{G_c k B} - T_1 = \frac{R_{Cal,1}(T_2 - T_1)}{R_{Cal,2} - R_{Cal,1}} - T_1 \tag{5.16}$$

Calibration Precision

For the calibration source, the standard deviation in the measurement is:

$$\Delta T = \frac{T}{\sqrt{B\tau}} \tag{5.17}$$

The standard deviation of the estimator for a signal with a known noise power is derived in Appendix C. The result is given as:

$$\sigma_s = \hat{P}_s \sqrt{\frac{1}{N_r}\left(1 + \frac{1}{S_N}\right)^2 + \frac{1}{N_n}\left(\frac{1}{S_n}\right)^2} \tag{5.18}$$

Where $N_r = B\tau_r$ is the integration time of the signal + noise condition and $N_n = B\tau_n$ is the integration time of the noise/calibration state.

For the following propagation of error analysis the following assumption were made.

1. The EIRP is retrieved when the satellite elevation results in minimal error due to reflection. See Figure 5.10.

2. The value for the observation integration is nominally $2^{10} - 1 = 1023$

3. The constraint of measuring the signal for 4x longer than the calibration source was placed on the system.

From assumption 1, we are able to use the simplified equation for the observable.

$$R(0,0) = G_{sys}\Big(C_D G_D + k(T_{FE} + T_A)B\Big) + \nu_0 \tag{5.19}$$

From assumption 2, we solve for values of R_{C1}, R_{C2} using Equation 5.14. Substituting Equations 5.15, 5.16 into Equation 5.6, we get the EIRP estimation:

$$EIRP_{Est} = \left(R(0,0) - R_{C1} - \left(\frac{(T_A - T_1)(R_{C2} - R_{C1})}{T_2 - T_1}\right)\right)\frac{kB(T_2 - T_1)(4\pi R_D)^2}{(R_{C2} - R_{C1})G_D\lambda^2} \tag{5.20}$$

Using a computer linear algebra solver, we take the partial derivatives and solve the propagation of errors. Figure 5.11 shows the error in dB of the EIRP estimate as a function of integration time.

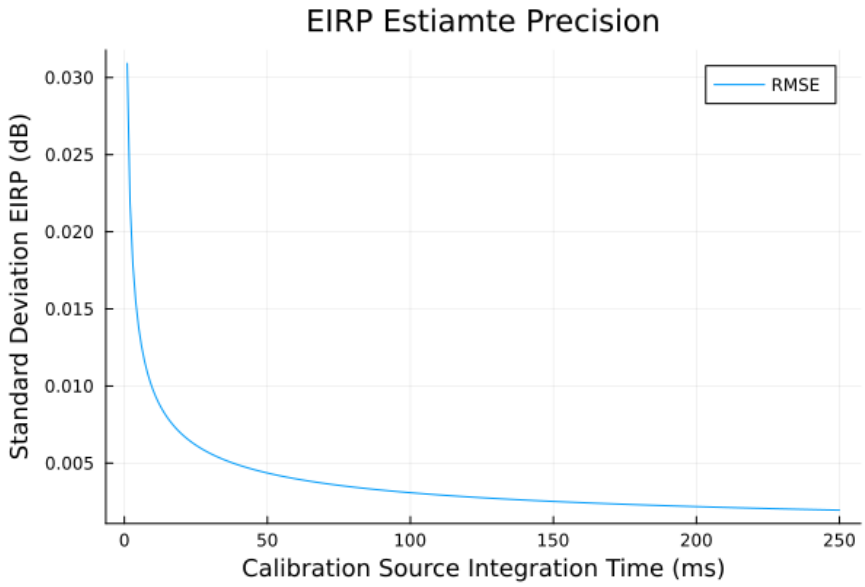

Figure 5.11. EIRP Estimate Error

6. TOWER BASED DEMONSTRATION

A tower based instrument was also designed to demonstrate the SoOp retrieval method. The instrument is designed to be a multi-band, recording I, P, S, and L band SoOp signals. Building from previous instruments, this design featured a redesigned RF/digital physical arrangement, improved power stability, thermally controlled front end, multiple RF calibration sources, and improved antennas

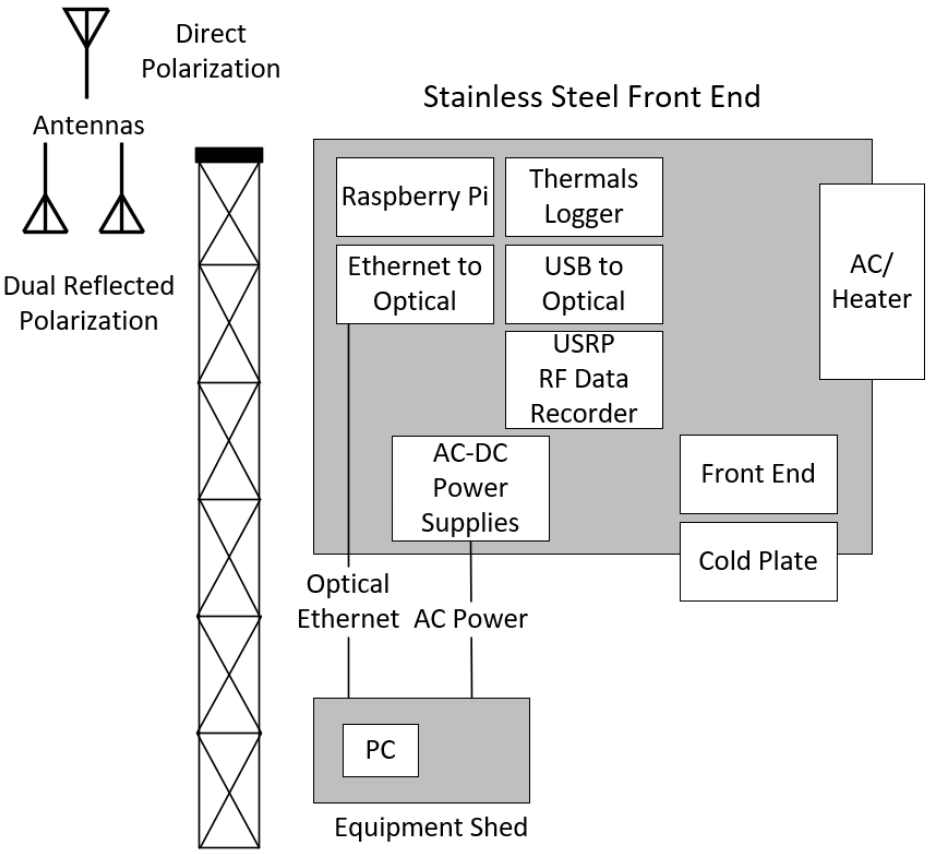

Figure 6.1. Component Locations

6.1 Component Locations

Previous iterations of SoOp based tower instruments placed the front end at the top of the tower and ran coaxial cables (150ft long) down the side to the digital receivers placed in an equipment shed at the bottom [20]. It was observed that the data from those instruments

had a high power and phase variation in the data with short integration periods. There was also a correspondence between this variation and wind speed. By placing the Ettus B210 USRP RF digitizing unit in the front end enclosure, the long coaxial cables were eliminated. A USB-Optical converter was placed in the front end and optical fiber (digital data) was run to the equipment shed.

6.1.1 Power

AC power was run to the front end enclosure and linear AC to DC converters were used for the appropriate front end voltages. This allows for easy addition of extra voltages and additional power to be added to the front end in the future. Previously, 5V and 12V DC power was generated in the equipment shed and ran to the top of the tower. This method had a drawback of observed ripple DC power at the front end, most likely a side effect of the long distance between the DC source and the front end load. Placing AC to DC converters in the front end eliminated this issue.

6.1.2 Thermal Control

The front end enclosure also includes the analog to digital converter as well as the AC to DC power converters, both devices produce a significant heat load. A thermoelectric forced air cooling/heating unit is used to dump the heat created by the active components. The first amplifier, cold loads, matched loads, directional-couplers and noise diode are all placed on a thermoelectric hot/cold plate. The front end also has 7 Resistance Temperature Detectors (RTD) placed on the matched load and various amplifiers for aid in data calibration.

6.1.3 Antennas

Circularly polarized COTS antennas were procured for all signals bands. All signal bands have both LHCP and RHCP reflected polarization. All antennas will be placed on ground planes to increase their front-to-back ratio.

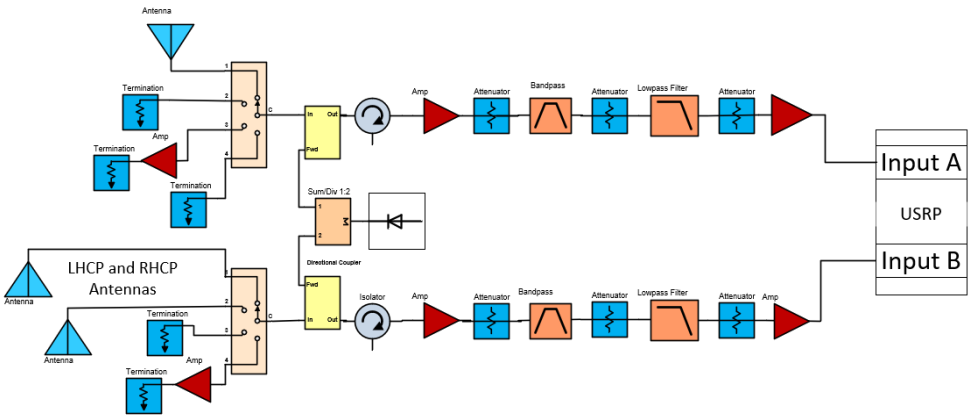

Figure 6.2. Simplified Single Band Tower Frontend

6.2 Microwave Design

A single front end was designed to record the I, P, S and L band SoOp Signals. The instrument is designed to record both RHCP and LHCP reflected signals. The front end is only capable of recording a single band/reflected polarization pair at a time.

The design was primarily driven by only having a single noise diode to share between all of the signal bands. Solid state SP4T RF switches are used for the calibration sources. These were chosen for long-term gain stability for the calibration sources. To keep the microwave system noise low, the SP2T switches are low loss mechanical. Each channel has three calibration sources, an active cold load, a matched load and a coupler injected noise diode. Isolators are used to account for impedance mismatch between the first LNA and the calibration section. Band pass filters were procured for all frequency bands. S-Band does not have a band pass filter due to cost and lead time of the filter. All signal chains are connected to SP4T switches and a single data recorder. An example of a single signal chain is shown in Figure 6.2. The full block diagram is shown in Appendix B, Figure B.1.

6.2.1 Calibration Control

Previous iterations of SoOp towers did not have synchronization between the data recording start time, calibration states and reflected polarization [20], [35]. The Ettus B210 data

Table 6.1. Tower Link Budget

Band Name	I-Band	P-Band	L-band	S-Band
Frequnecy	137.5 MHz	370 MHz	1.575 GHz	2.343 GHz
Front End Bandwidth	1 MHz	20 MHz	10 MHz	8 MHz
Transmitter EIRP	12 dBW	43 dBW	24.8 dBW	71.5 dBW
Path Loss	141.33 dB	175 dB	182 dB	191 dB
Antenna Gain	3 dB	3 dB	3 dB	3 dB
Noise Figure	3.34 dB	4 dB	2.859 dB	2.36 dB
System Gain	71 dB	51 dB	47 dB	64 dB
Expected C/N	17.00906 dB	0.169696 dB	-19.9168 dB	19.86 dB

recorder has 8 GPIOs available that are controlled with RF sample level timing precision. Due to the number of switch control wires for the front end calibration, a Arduino Due was used as a simple "multiplex control unit" between the B210 and the front end switches. The Arduino runs a simple program that changes the outputs to the RF switches based on the 8 GPIO "bits" from the B210.

A link budget is shown in Table 6.1. All C/N numbers are before integration. The P-Band MUOS signal is a low SNR signal by design. For L-Band, The negative SNR is expected for as GPS L1 signal is designed to be below the noise floor.

7. SPIRE DEMONSTRATION

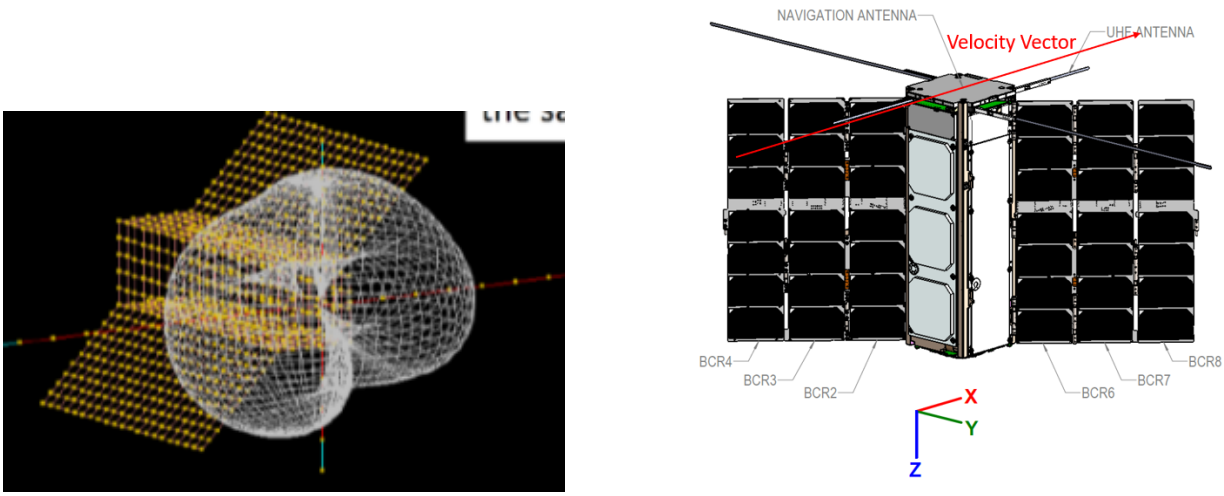

(a) Antenna Pattern

(b) LEMUR 2 Satellite

Figure 7.1. SPIRE Satellite

In late 2021, an opportunity became available to obtain raw P-Band data from a space instrument. SPIRE Global, Inc operates satellites designed to record RF data. An arrangement with Goddard Space Flight Center allowed for the capture of raw RF data in P-Band. This data was used to demonstrate the auto-correlation method of reflectivity retrieval.

The SPIRE instrument was flown on the Low Earth Multi-Use Receiver (LEMUR) 3U cube sat platform. It primary consisted of a software defined radio and designed for receiving communication signals. The antennas were linearly polarized dipoles. A figure of the simulated antenna gain pattern of the Software Defined Radio (SDR) antenna is shown in figure 7.1a.

This instrument differs from the SNOOPI instrument in a few ways:

1. The RF frontend does not have the P-Band RFI filters.

   The instrument relies on the filters of the SDR ASIC down converter and digitizer.

2. The instrument lacks RF power calibration hardware.

   Because the instrument was designed to be a communications receiver, the front end does not contain any radiometric power calibration hardware.

7.1 Data Processing

9.175 seconds of data collected on 12/23/2021 has been processed. The data has a sampling bandwidth of 5 MHz with 12-bit complex quantization, centered at 367.5 MHz. Two Line Element (TLEs) were used for the MUOS-5 and the "Djara" Spire satellite to predict the orbits. Specular point prediction software developed for the SNOOPI mission generated a list of predicted delay and Doppler values based on the TLEs. For calculation efficiency, the correlation for the DDM generator algorithm is performed in the frequency domain via a Fast Fourier Transformation (FFT). The raw data was post-processed to produce DDMs via the same algorithem described in the simulator section.

DDMs of the data were generated with integration time of 5 ms, Doppler range of ±1500 hz and a delay range of ±10 samples. The data was upsampled by a factor of 4 before the DDM was created to allow for a better estimate of the reflected peak for curve fitting. The DDM dimensions were chosen for visualization purposes. An example DDM is shown in Figure 7.2

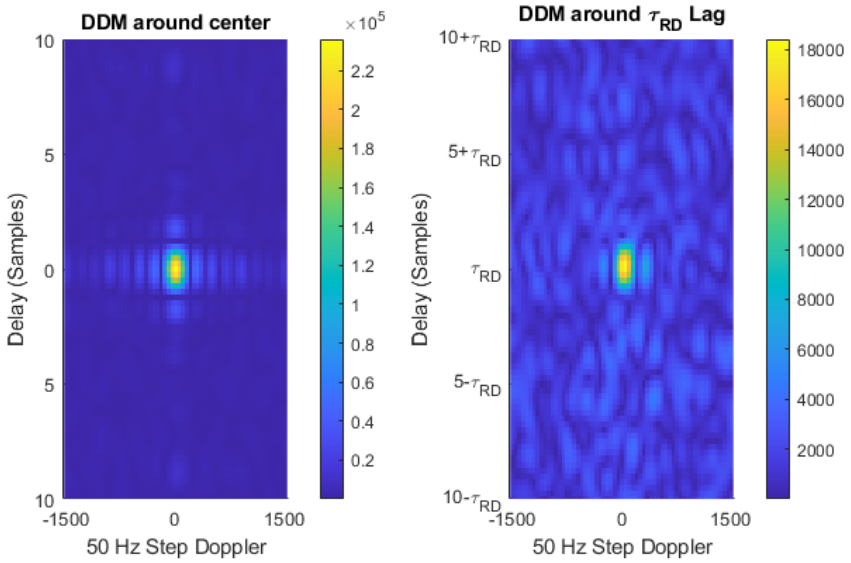

Figure 7.2. Example SPIRE DDM

7.2 Reflectivity Estimation

Repeating the observable equations from section 3.3 here:

$$y_1 = \mathcal{R}(0,0) = G_{sys}\Big[G_D C_D + G_R C_D \Gamma + kT_{sys}B + \nu_0\Big] \tag{7.1}$$

$$y_2 = \mathcal{R}(\tau_{RD}, \omega_{RD}) = G_{sys}\Big[C_D\sqrt{G_D G_R \Gamma} + \nu_{RD}\Big] \tag{7.2}$$

The challenge for this instrument is we cannot obtain an estimate of system noise $T_{sys}B$ as with the SNOOPI instrument. A signal to noise ratio is defined, where T_{sys} is the system noise figure.

$$S = \left(\frac{G_d}{T_{sys}}\right)\frac{C_D}{kB} \tag{7.3}$$

$$d \approx \frac{1 + \mid \mathcal{R}_{\mathrm{e}} \mid^2 + S^{-1}}{\mathcal{R}_{\mathrm{e}}} \tag{7.4}$$

The reflectivity is estimated:

$$d = \frac{y_1}{2y_2} = \frac{1 + \mathcal{R}_{\mathrm{e}}^2}{2\mathcal{R}_{\mathrm{e}}} \tag{7.5}$$

$$\mathcal{R}_{\mathrm{e}} = d \pm \sqrt{d^2 - 1} \tag{7.6}$$

$$\mathcal{R}_{\mathrm{e}} = \frac{R_D}{(R_{TS} + R_{SR})}\sqrt{\frac{G_R}{G_D}}\mathcal{R} \tag{7.7}$$

The reflected peak was fit with a 3rd-order polynomial to estimate the reflected delay position and amplitude.

7.3 Data Quality Control

The processed data set has 1834 DDMs. Quality control was performed on the data set as follows:

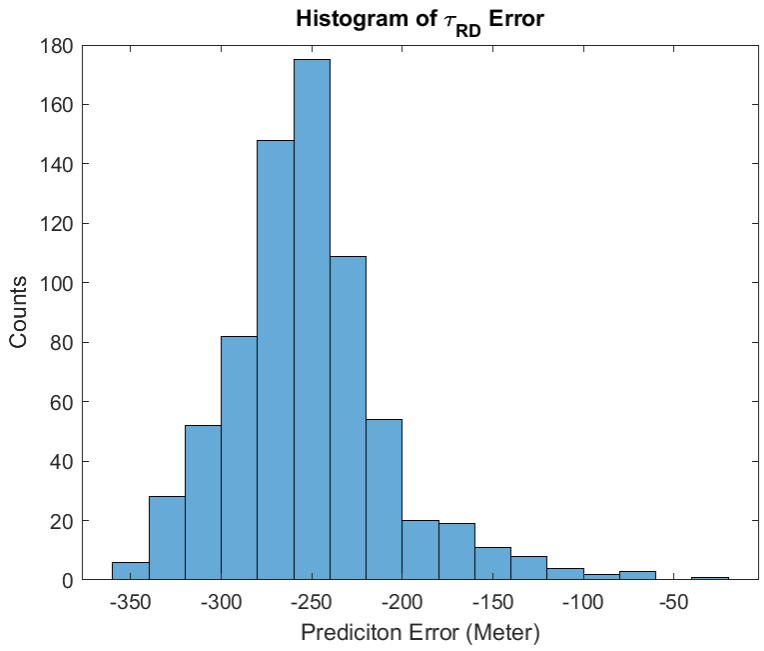

Figure 7.3. Histogram of Estimated Delay

1. Removed all DDMs with reflected peaks amplitude below 4.3 SNR.

2. Remove all DDMs with an estimated Doppler more than 100 Hz $\pm$ the predicted Doppler.

3. Remove all DDMs with the amplitude of the reflected peak greater than 3σ the mean value of the reflected peaks.

Test 1 and 2 removed approximately %50 of the DDMs with low SNR values. Test 3 removes the cases of RFI. Figure 7.3 shows the histrogram of the observed Doppler.

7.4 Overpass

Values for $\frac{G_d}{T_{sys}}$ were determined based on the antenna gain pattern and the published front end noise figure. Three values of the antenna gain $G_d = [-2, -1, 1]$ dB were chosen. A quality controlled time series of the estimated reflectivity it shown in Figure 7.5.

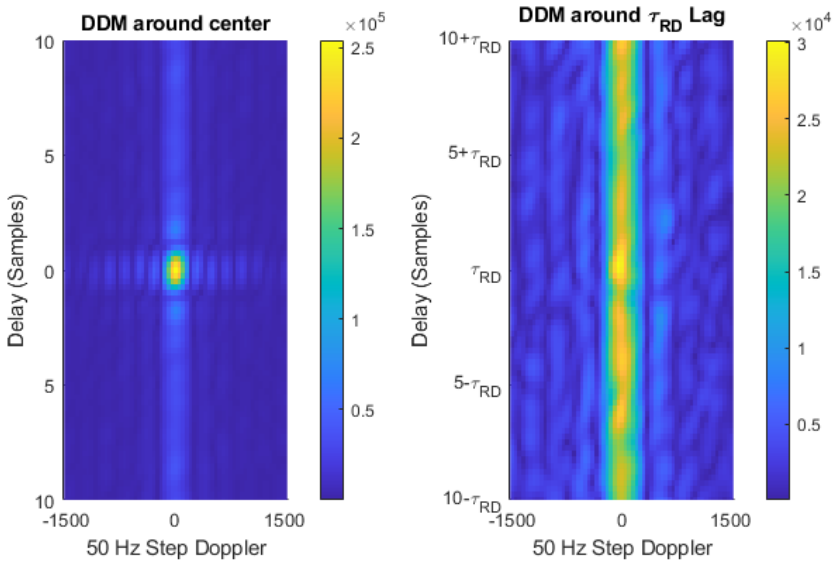

Figure 7.4. Example SPIRE DDM with RFI

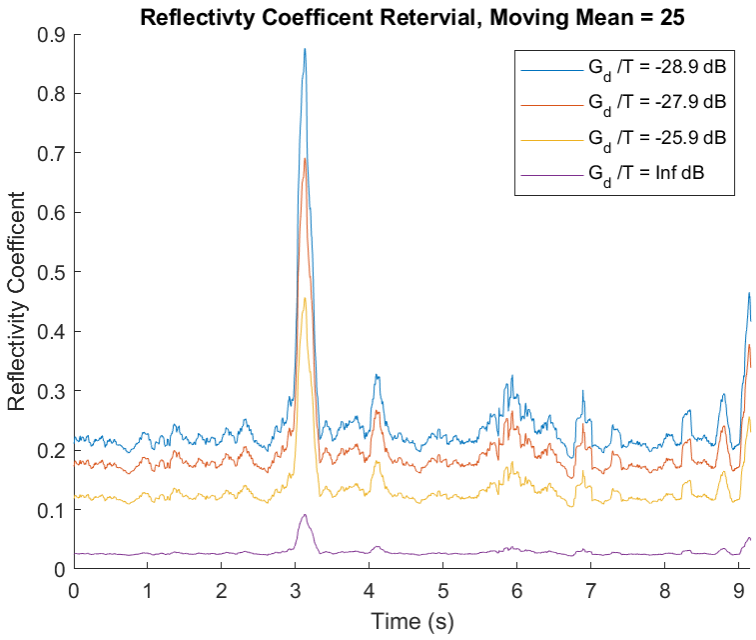

Figure 7.5. Reflectivity Estimate

The reflectivity estimate $\frac{G}{T_{sys}} = -27.9$ dB is plotted over a Google Earth image in Figure 7.6. The reflected track runs over the border of Minnesota and Wisconsin. The reflectivity track was adjusted 2540 m in the cross track direct of the normal (approximately NNE

direction) and 1.8 seconds along track. This aligned the peak reflectivity over Mud Lake south of Quamba, MN.

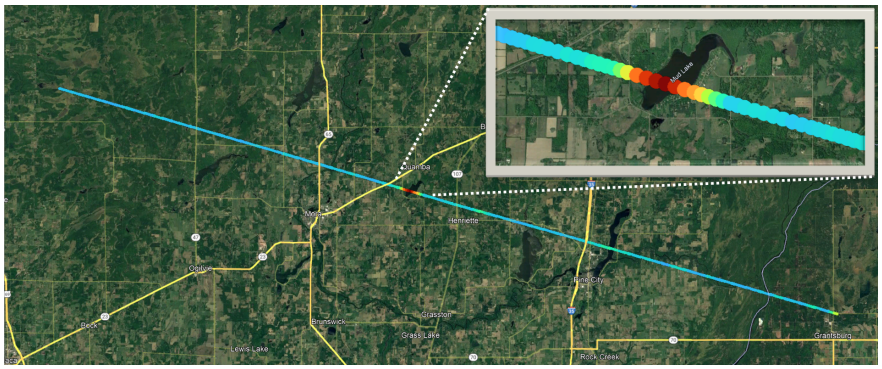

Figure 7.6. Reflectivity Ground Track

7.5 Conclusion

The SPIRE data set consists of 4 recordings taken with 3 similar spacecraft. A cursory processing of the later three data sets shows significant RFI in the data. It has not yet been determined if the RFI is from the ground or due to the spacecraft bus (internal jamming). Table 7.1 summarizes the data sets.

Table 7.1. Summary of SPIRE Recording Data

Date	Spacecraft Name	Satcat ID	Recording Length	Overpass Location
12/23/2021	Djara	46926	9 Seconds	Minnesota
04/12/2022	Miriwari	51054	>25 seconds	Minesota
06/03/2022	Djirang	51058	30 Seconds	Mississippi
06/03/2022	Djirang	51058	30 Seconds	Georgia

8. CONCLUSIONS

SNOOPI is planned to launch in early 2024 with a planned 9 months of operation. The sample-level simulator is planned to be expanded to include sources of RFI in the simulation. SNOOPI's raw data capture modes will collect any RFI sources and the simulator can be updated to estimate their effects on DDMs and the reflectivity estimates.

The remaining datasets of the SPIRE data will be analyzed. It is yet unclear if the observed RFI in the remaining datasets of SPIRE data is from the instrument itself or from an external transmitter. Combined with the data from SNOOPI, there will be a greater understanding of P-Band RFI in space. SNOOPI will also have the benefit of being able collect the other 3 channels than 367.5 MHz for a more complete RFI picture.

Looking ahead, the WYATT-EIRP system will be used for periodic monitoring of the MUOS satellite transmitters. It will also be used to monitor for any new space-based P-Band sources . It is also planned to use the station to verify the background galactic noise maps for 370 MHz and make any necessarily adjustments for 255 MHz. The simulator can be easily modified for new space-based SoOp instruments.

REFERENCES

[1] E. National Academies of Sciences, Ed., *Thriving on Our Changing Planet: A Decadal Strategy for Earth Observation from Space* (Consensus study report), eng. 2019, ISBN: 0-309-46757-8. DOI: 10.17226/25437.

[2] NASA, "NASA Responding to the Challenge of Climate and Environmental Change : NASA's Plan for a Climate-Centric Architecture for Earth Observations and Applications from Space," NASA, Tech. Rep. June, 2010. [Online]. Available: www.nasa.gov.

[3] R. D. Koster, S. P. Mahanama, B. Livneh, D. P. Lettenmaier, and R. H. Reichle, "Skill in streamflow forecasts derived from large-scale estimates of soil moisture and snow," *Nature Geoscience*, vol. 3, no. 9, pp. 613–616, 2010, ISSN: 17520894. DOI: 10.1038/ngeo944.

[4] A. A. G. Al-Shammary, A. Z. Kouzani, A. Kaynak, S. Y. Khoo, M. Norton, and W. Gates, "Soil Bulk Density Estimation Methods: A Review," *Pedosphere*, vol. 28, no. 4, pp. 581–596, Aug. 2018, ISSN: 10020160. DOI: 10.1016/S1002-0160(18)60034-7.

[5] Marshall, H.P., Vuyovich, Carrie, Hiemstra, Chris, *et al.*, "NASA SnowEx 2020 Experiment Plan," National Aeronautics and Space Administration, Experiment Plan, 2020, p. 82.

[6] A. Lundberg, N. Granlund, and D. Gustafsson, "Towards automated 'Ground truth' snow measurements-a review of operational and new measurement methods for Sweden, Norway, and Finland," *Hydrological Processes*, n/a–n/a, 2010, ISSN: 08856087, 10991085. DOI: 10.1002/hyp.7658.

[7] D. Entekhabi, E. G. Njoku, P. E. O'Neill, *et al.*, "The soil moisture active passive (SMAP) mission," *Proceedings of the IEEE*, 2010, ISSN: 00189219. DOI: 10.1109/JPROC.2010.2043918.

[8] S. K. Chan, R. Bindlish, P. E. O'Neill, *et al.*, "Assessment of the SMAP Passive Soil Moisture Product," *IEEE Transactions on Geoscience and Remote Sensing*, vol. 54, no. 8, pp. 4994–5007, Aug. 2016, ISSN: 0196-2892, 1558-0644. DOI: 10.1109/TGRS.2016.2561938.

[9] A. Chang, J. Foster, and D. Hall, "Nimbus-7 SMMR Derived Global Snow Cover Parameters," *Annals of Glaciology*, vol. 9, pp. 39–44, 1987, ISSN: 0260-3055. DOI: 10.3189/s0260305500200736.

[10] M. T. Hallikainen and P. A. Jolma, "Comparison of Algorithms for Retrieval of Snow Water Equivalent from Nimbus-7 SMMR Data in Finland," *IEEE Transactions on Geoscience and Remote Sensing*, vol. 30, no. 1, pp. 124–131, 1992, ISSN: 15580644. DOI: 10.1109/36.124222.

[11] M. Durand and S. A. Margulis, "Correcting first-order errors in snow water equivalent estimates using a multifrequency, multiscale radiometric data assimilation scheme," *Journal of Geophysical Research: Atmospheres*, vol. 112, no. D13, n/a–n/a, ISSN: 0148-0227. DOI: 10.1029/2006JD008067.

[12] S. J. Katzberg and J. L. Garrison, "Utilizing GPS To Determine Ionospheric Delay Over the Ocean," 1996.

[13] H. Carreno-Luengo, S. Lowe, C. Zuffada, S. Esterhuizen, and S. Oveisgharan, "Spaceborne GNSS-R from the SMAP mission: First assessment of polarimetric scatterometry over land and cryosphere," *Remote Sensing*, vol. 9, no. 4, Apr. 2017, ISSN: 20724292. DOI: 10.3390/rs9040362.

[14] C. Chew, R. Shah, C. Zuffada, G. Hajj, D. Masters, and A. J. Mannucci, "Demonstrating soil moisture remote sensing with observations from the UK TechDemoSat-1 satellite mission," *Geophysical Research Letters*, 2016, ISSN: 19448007. DOI: 10.1002/2016GL068189.

[15] C. C. Chew and E. E. Small, "Soil moisture sensing using spaceborne GNSS reflections: Comparison of CYGNSS reflectivity to SMAP soil moisture," *Geophysical Research Letters*, vol. 45, no. 9, pp. 4049–4057, 2018. DOI: 10.1029/2018GL077905. eprint: https://agupubs.onlinelibrary.wiley.com/doi/pdf/10.1029/2018GL077905.

[16] R. Shah, J. L. Garrison, and M. S. Grant, "Demonstration of bistatic radar for ocean remote sensing using communication satellite signals," *IEEE Geoscience and Remote Sensing Letters*, vol. 9, no. 4, pp. 619–623, 2012, ISSN: 1545598X. DOI: 10.1109/LGRS.2011.2177061.

[17] J. Garrison, Y. C. Lin, B. Nold, *et al.*, "Remote sensing of soil moisture using P-band signals of opportunity (SoOp): Initial results," in *International Geoscience and Remote Sensing Symposium (IGARSS)*, vol. 2017-July, 2017, pp. 4158–4161, ISBN: 9781509049516. DOI: 10.1109/IGARSS.2017.8127917. [Online]. Available: www.n2yo.co..

[18] Y.-C. Lin, *Remote Sensing of Soil Moisture with Signals of Opportunity (SOOP)*, 2017.

[19] J. L. Garrison, B. Nold, Y. C. Lin, *et al.*, "Recent results on soil moisture remote sensing using P-band signals of opportunity," in *Proceedings of the 2017 19th International Conference on Electromagnetics in Advanced Applications, ICEAA 2017*, Institute of Electrical and Electronics Engineers Inc., Oct. 2017, pp. 1604–1607, ISBN: 9781509044511. DOI: 10.1109/ICEAA.2017.8065595.

[20] B. R. Nold, "DESIGN OF AN INSTRUMENT FOR SOIL MOISTURE AND ABOVE GROUND BIOMASS REMOTE SENSING USING SIGNALS OF OPPORTUNITY A Dissertation," Ph.D. dissertation, Purdue University, 2019. DOI: 10.25394/PGS.9108248.v1.

[21] J. D. Covert, "Unmanned aerial vehicle remote sensing of soil moisture with I-band signals of opportunity," May 2020. DOI: 10.25394/PGS.12275162.v1.

[22] S. H. Yueh, X. Xu, R. Shah, *et al.*, "Remote Sensing of Snow Water Equivalent Using Coherent Reflection from Satellite Signals of Opportunity: Theoretical Modeling," *IEEE Journal of Selected Topics in Applied Earth Observations and Remote Sensing*, 2017, ISSN: 21511535. DOI: 10.1109/JSTARS.2017.2743172.

[23] A. Komanduru, "REMOTE SENSING OF SNOW USING BISTATIC RADAR REFLECTOMETRY," Ph.D. dissertation, Purdue University, 2016.

[24] J. L. Garrison, R. Shah, S. Kim, *et al.*, "Analyses Supporting Snoopi: a P-Band Reflectometry Demonstration," *International Geoscience and Remote Sensing Symposium (IGARSS)*, pp. 3349–3352, 2020. DOI: 10.1109/IGARSS39084.2020.9323547.

[25] J. D. Oetting and T. Jen, "The Mobile User Objective System," *Johns Hopkins APL Technical Digest (Applied Physics Laboratory)*, vol. 30, no. 2, pp. 103–112, 2011, ISSN: 02705214.

[26] R. B. Jackson, "THE CANTED TURNSTILE AS AN OMNIDIRECTIONAL SPACECRAFT ANTENNA SYSTEM," Tech. Rep., 1967.

[27] M. Remazeilles, C. Dickinson, A. J. Banday, M. A. Bigot-Sazy, and T. Ghosh, "An improved source-subtracted and destriped 408-MHz all-sky map," *Monthly Notices of the Royal Astronomical Society*, vol. 451, no. 4, pp. 4311–4327, 2015, ISSN: 13652966. DOI: 10.1093/mnras/stv1274. arXiv: 1411.3628.

[28] J. Bezanson, A. Edelman, S. Karpinski, and V. B. Shah, "Julia: A fresh approach to numerical computing," *SIAM Review*, vol. 59, no. 1, pp. 65–98, 2017. DOI: 10.1137/141000671. [Online]. Available: https://epubs.siam.org/doi/10.1137/141000671.

[29] S. Kim and J. L. Garrison, "Development of an End-to-End Mission Simulator for Land Remote Sensing with Signals of Opportunity," *International Geoscience and Remote Sensing Symposium (IGARSS)*, pp. 5933–5936, 2020. DOI: 10.1109/IGARSS39084.2020.9323710.

[30] T. Wang, C. Ruf, S. Gleason, B. Block, D. McKague, and D. Provost, "Development of GPS constellation power monitor system for high accuracy calibration/validation of the cygnss L1B data," *International Geoscience and Remote Sensing Symposium (IGARSS)*, vol. 2017-July, pp. 1008–1011, 2017. DOI: 10.1109/IGARSS.2017.8127125.

[31] T. Wang, C. S. Ruf, B. Block, D. S. McKague, and S. Gleason, "Design and Performance of a GPS Constellation Power Monitor System for Improved CYGNSS L1B Calibration," *IEEE Journal of Selected Topics in Applied Earth Observations and Remote Sensing*, vol. 12, no. 1, pp. 26–36, 2019, ISSN: 21511535. DOI: 10.1109/JSTARS.2018.2867773.

[32] Sten Schmidl Søbjærg, Jan E. Balling, N. Skou, and National, "Performance assessment of an LNA used as active cold load," in *IGARSS 2015*, 2015, pp. 4742–4745, ISBN: 9781479979295. DOI: 10.1007/978-1-349-95810-8_1129.

[33] B. R. Nold, "DESIGN OF AN INSTRUMENT FOR SOIL MOISTURE AND ABOVE GROUND BIOMASS REMOTE SENSING USING SIGNALS OF OPPORTUNITY A Dissertation," Ph.D. dissertation, Purdue University, 2019. DOI: 10.25394/PGS.9108248.v1. [Online]. Available: https://hammer.purdue.edu/articles/thesis/DESIGN%7B%5C_%7DOF%7B%5C_%7DAN%7B%5C_%7DINSTRUMENT%7B%5C_%7DFOR%7B%5C_%7DSOIL%7B%5C_%7DMOISTURE%7B%5C_%7DAND%7B%5C_%7DABOVE%7B%5C_%7DGROUND%7B%5C_%7DBIOMASS%7B%5C_%7DREMOTE%7B%5C_%7DSENSING%7B%5C_%7DUSING%7B%5C_%7DSIGNALS%7B%5C_%7DOF%7B%5C_%7DOPPORTUNITY/9108248.

[34] T. Liebig. "Openems - open electromagnetic field solver," General and Theoretical Electrical Engineering (ATE), University of Duisburg-Essen. (), [Online]. Available: https://www.openEMS.de.

[35] A. S. Choudhari, "Surface soil moisture retrieval using reflectometry of S-band signals of opportunities," Aug. 2020. DOI: 10.25394/PGS.12743843.v1.

[36] F. T. (T. Ulaby, *Microwave remote sensing : active and passive Volume 2* (Remote sensing ; no. 2-[4]), eng. Reading, Mass: Addison-Wesley Pub. Co., Advanced Book Program/World Science Division, 1981 - 1986, ISBN: 0890061939.

[37] H. Nyquist, "Thermal agitation of electric charge in conductors," eng, *Physical review*, vol. 32, no. 1, pp. 110–113, 1928, ISSN: 0031-899X.

[38] S. O. Rice, "Mathematical analysis of random noise," *Bell System Technical Journal*, vol. 24, no. 1, pp. 46–156, 1945. DOI: https://doi.org/10.1002/j.1538-7305.1945.tb00453.x. eprint: https://onlinelibrary.wiley.com/doi/pdf/10.1002/j.1538-7305.1945.tb00453.x. [Online]. Available: https://onlinelibrary.wiley.com/doi/abs/10.1002/j.1538-7305.1945.tb00453.x.

A. EIRP SYSTEM SIMULATIONS AND RESULTS

A.1 Manufacturer Provided Antenna Simulations

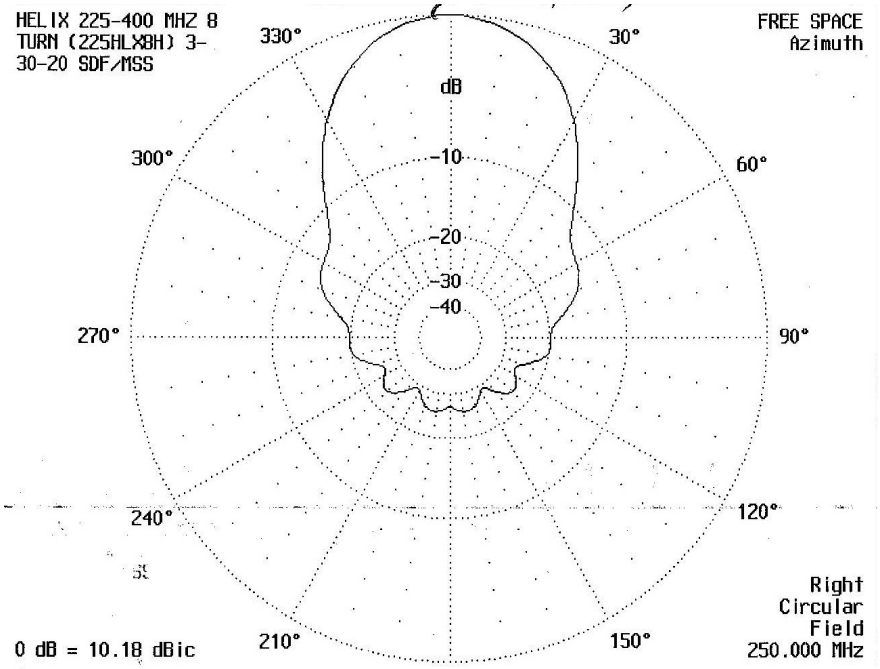

Figure A.1. Gain Pattern Single Element Helical Antenna - 255 MHz

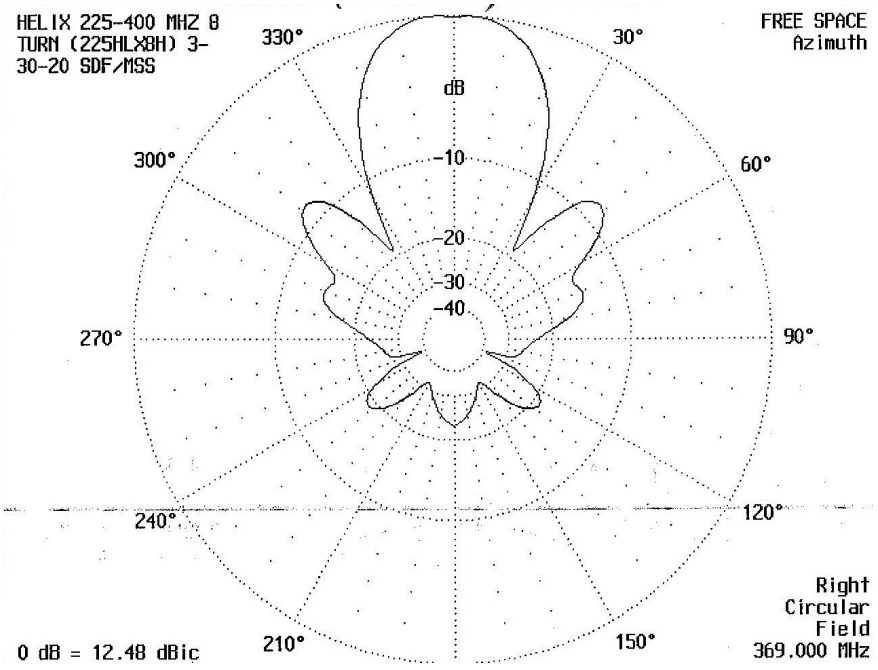

Figure A.2. Gain Pattern Single Element Helical Antenna - 370 MHz

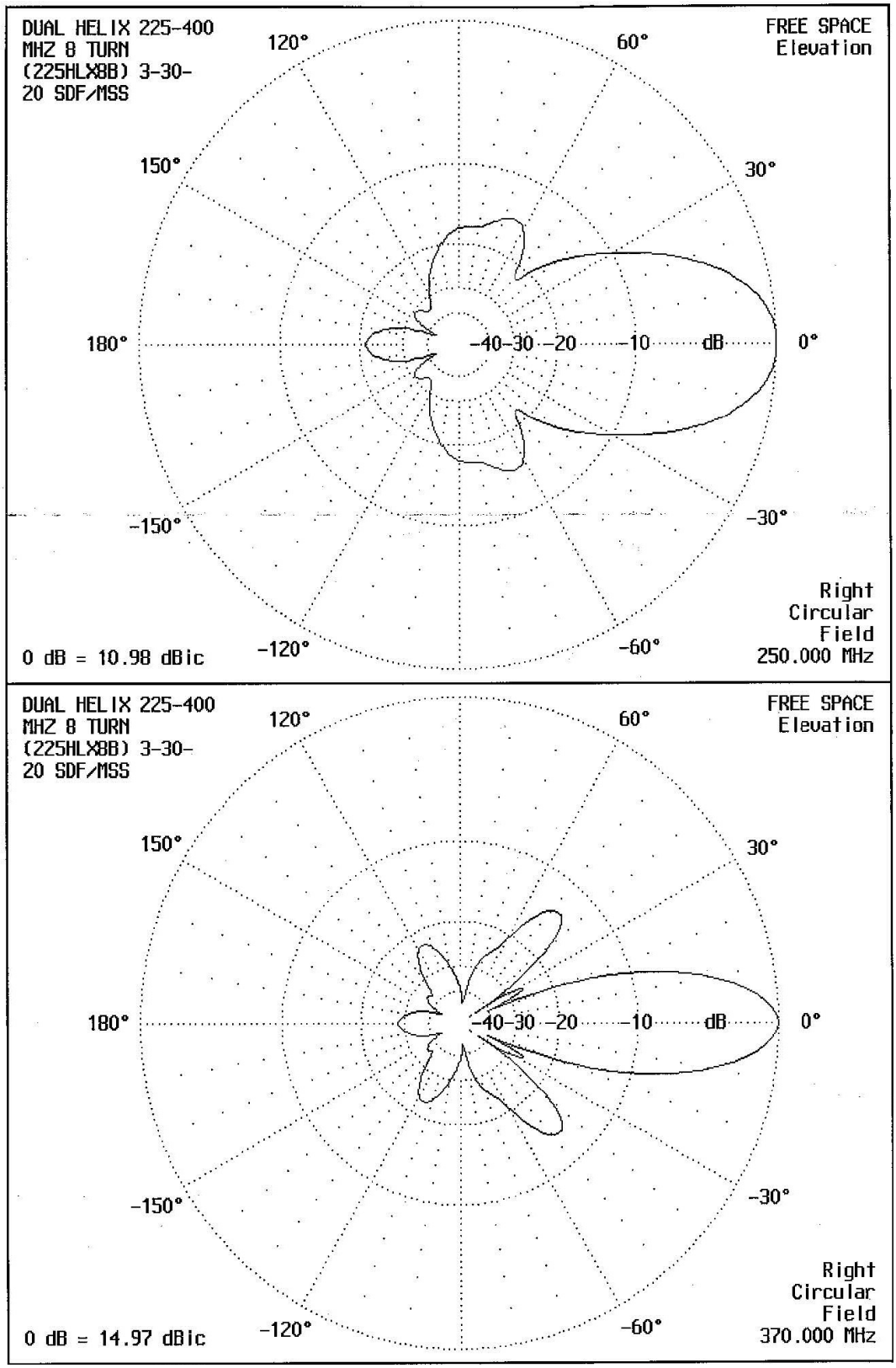

Figure A.3. Gain Pattern Vertically Stacked 38" Two Element Array

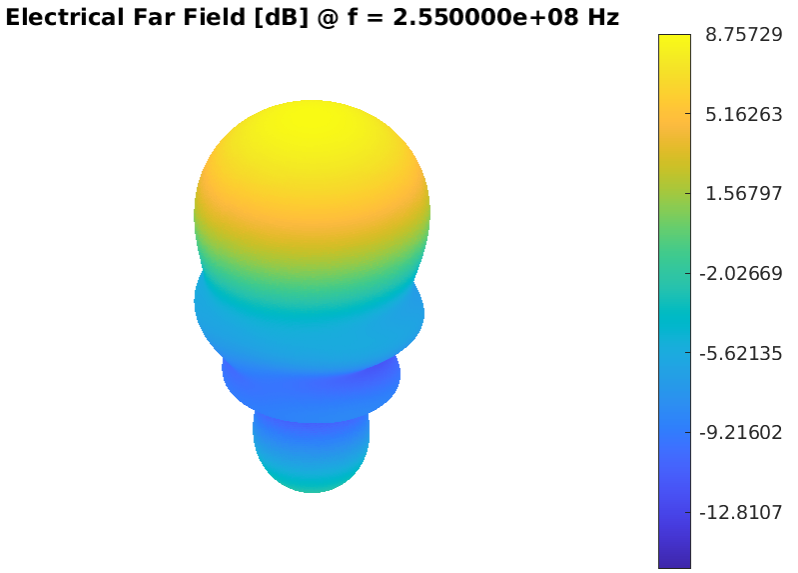

Figure A.4. 3D Single Antenna Gain Pattern Simulation - 255 MHz

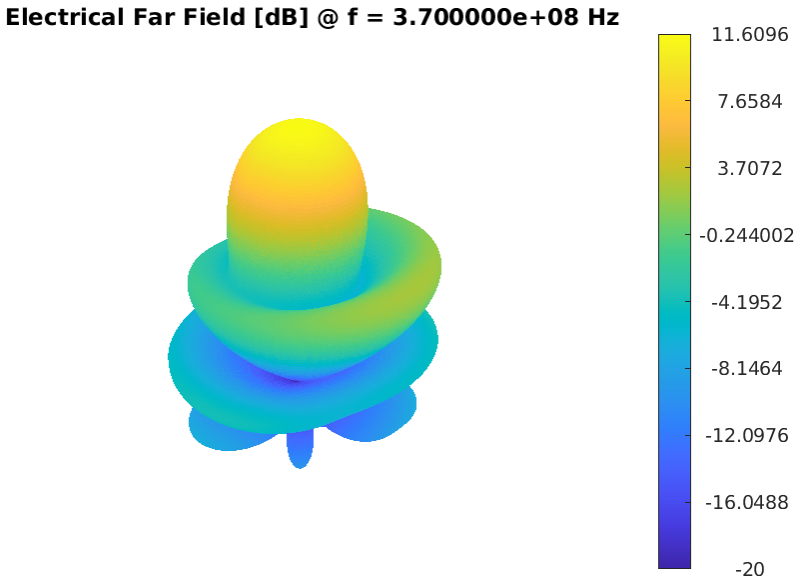

Figure A.5. 3D Single Antenna Gain Pattern Simulation - 370 MHz

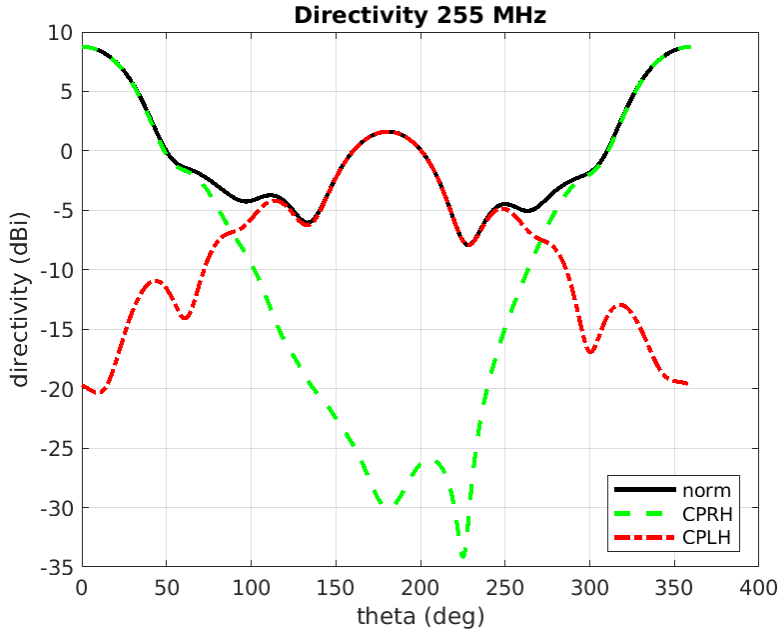

Figure A.6. Single Antenna Directivity Plot - 255 MHz

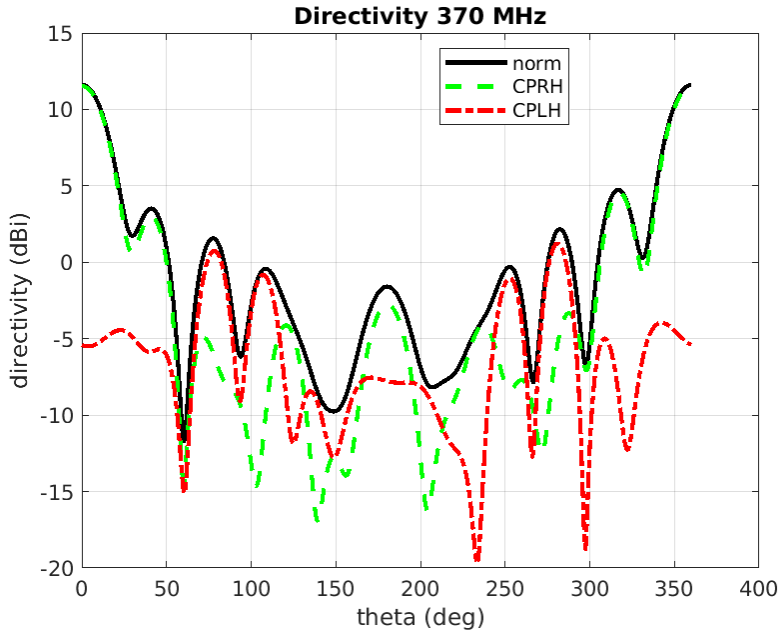

Figure A.7. Single Antenna Directivity Plot - 370 MHz

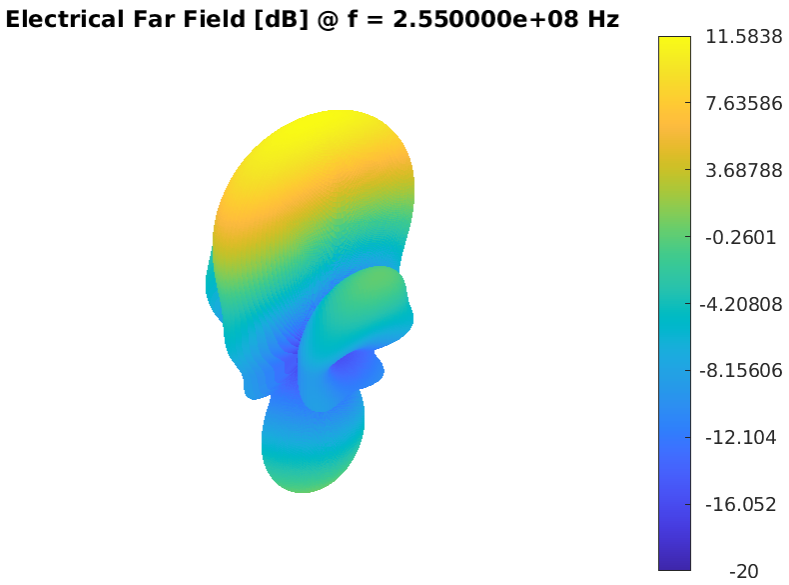

Figure A.8. 3D Antenna Array Gain Pattern Simulation - 255 MHz

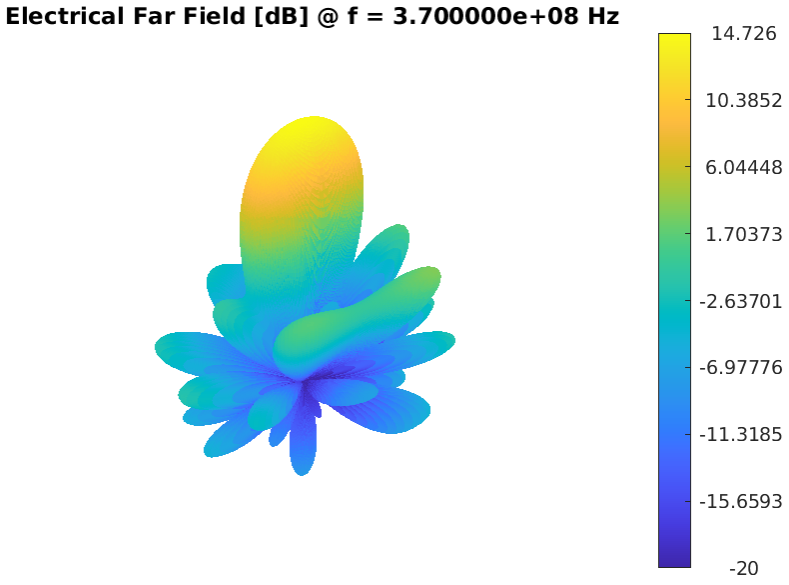

Figure A.9. 3D Antenna Array Gain Pattern Simulation - 370 MHz

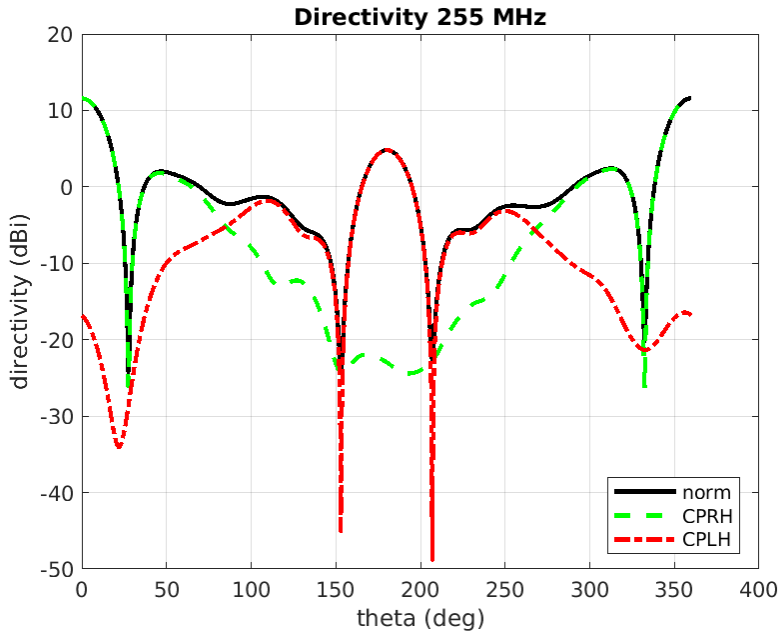

Figure A.10. Antenna Array Directivity Plot - 255 MHz

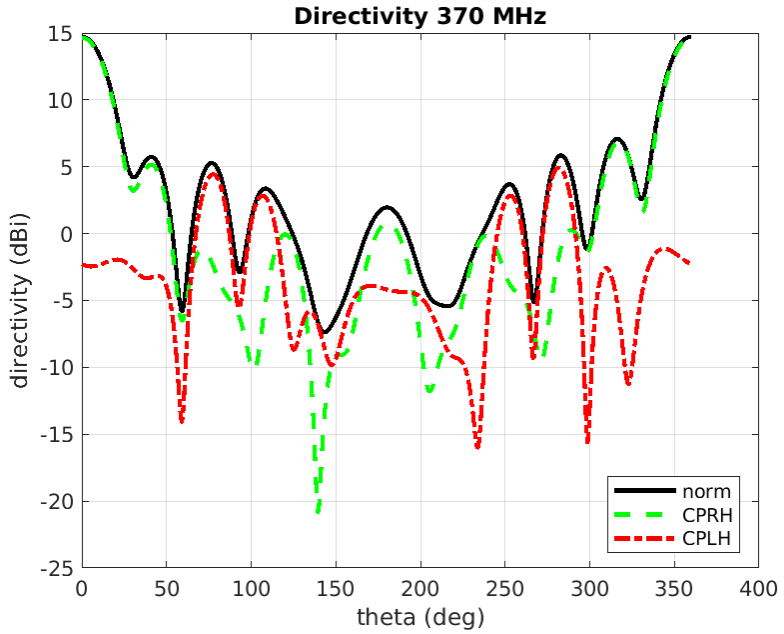

Figure A.11. Antenna Array Directivity Plot - 370 MHz

A.2 Front End Microwave Data

Cascaded Gain

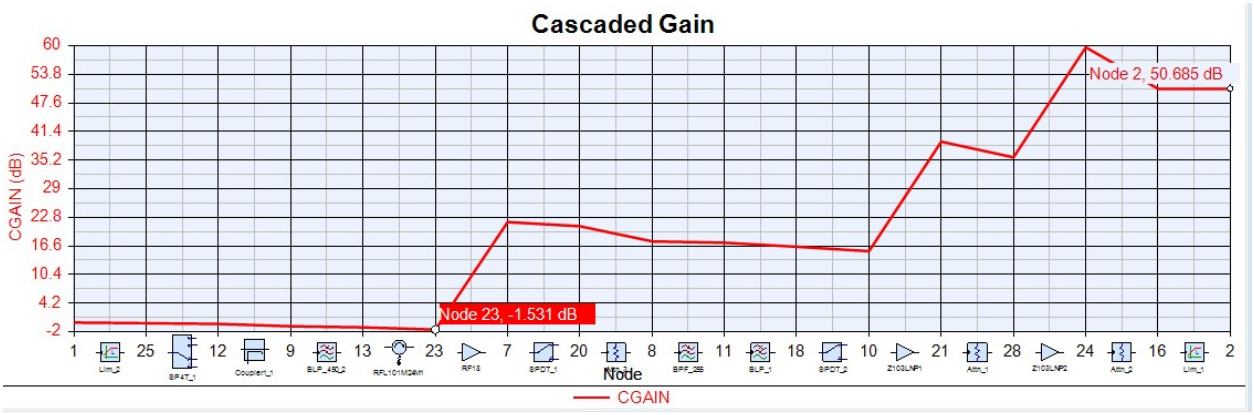

Figure A.12. Simulated Cascaded Gain of 255 MHz Chain

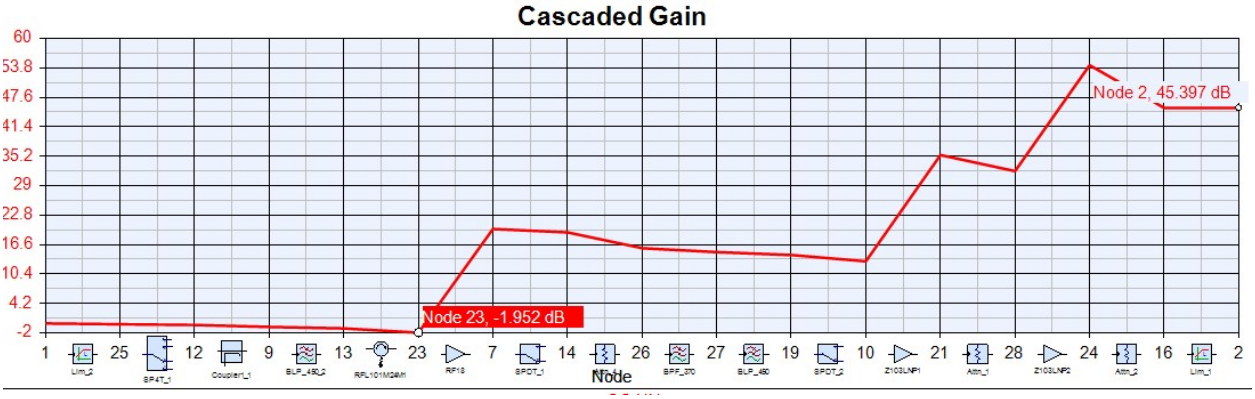

Figure A.13. Simulated Cascaded Gain of 370 MHz Chain

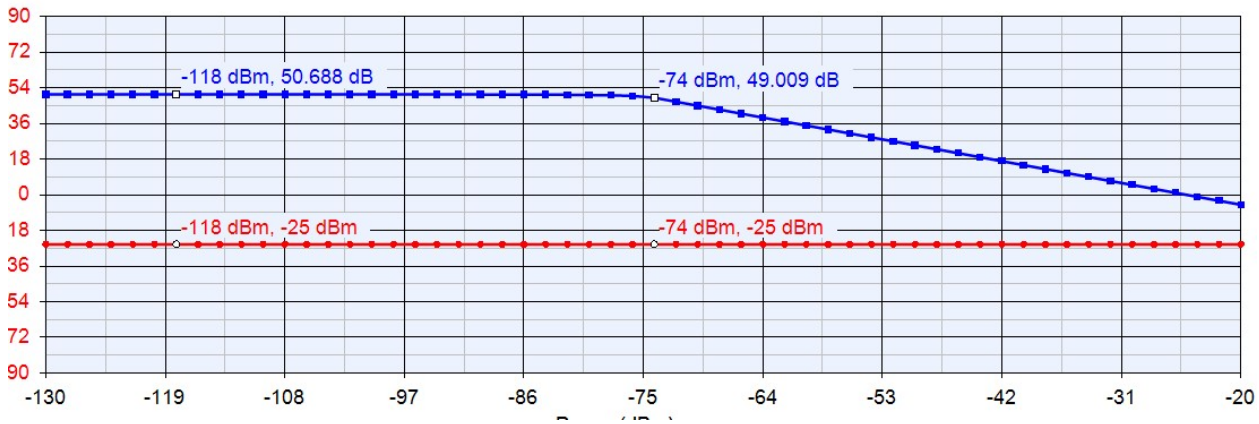

Figure A.14. Simulated Cascaded Gain Sweep 255 MHz

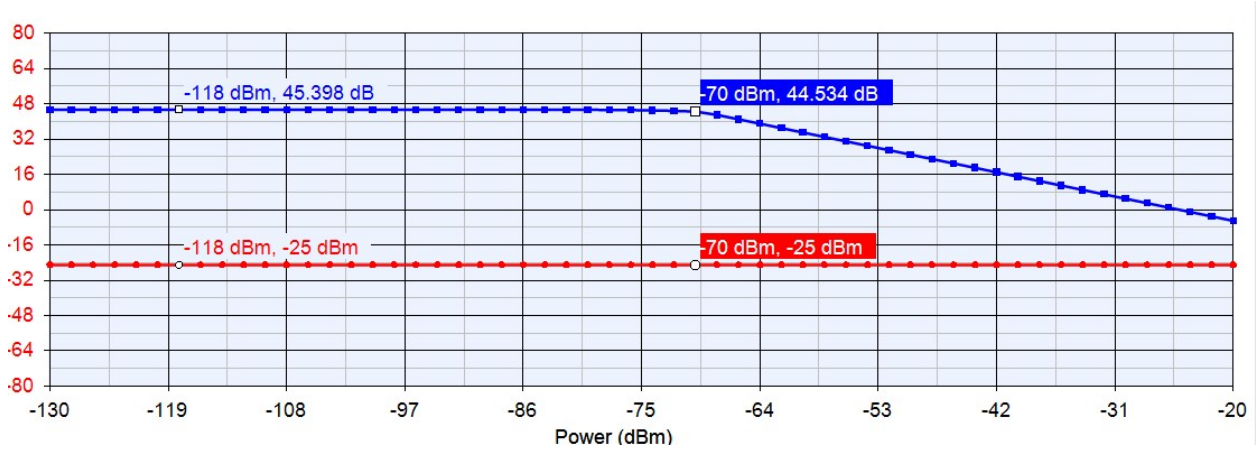

Figure A.15. Simulated Cascaded Gain Sweep 370 MHz

Noise Figure

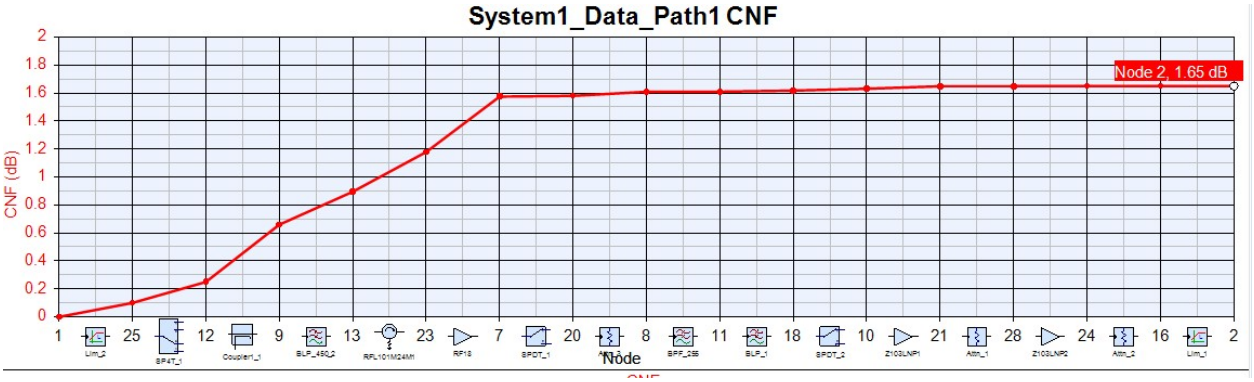

Figure A.16. Simulated Cascaded Noise Figure 255 MHz

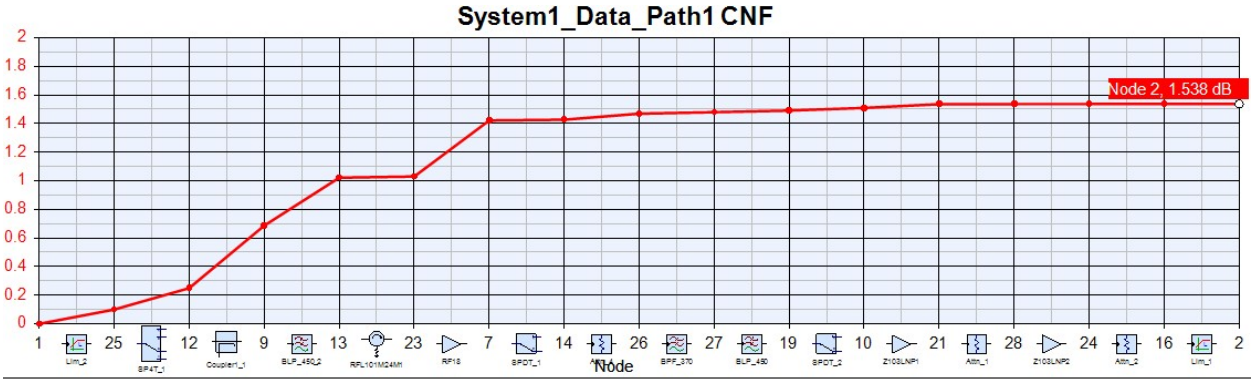

Figure A.17. Simulated Cascaded Noise Figure 370 MHz

S21 Sweeps

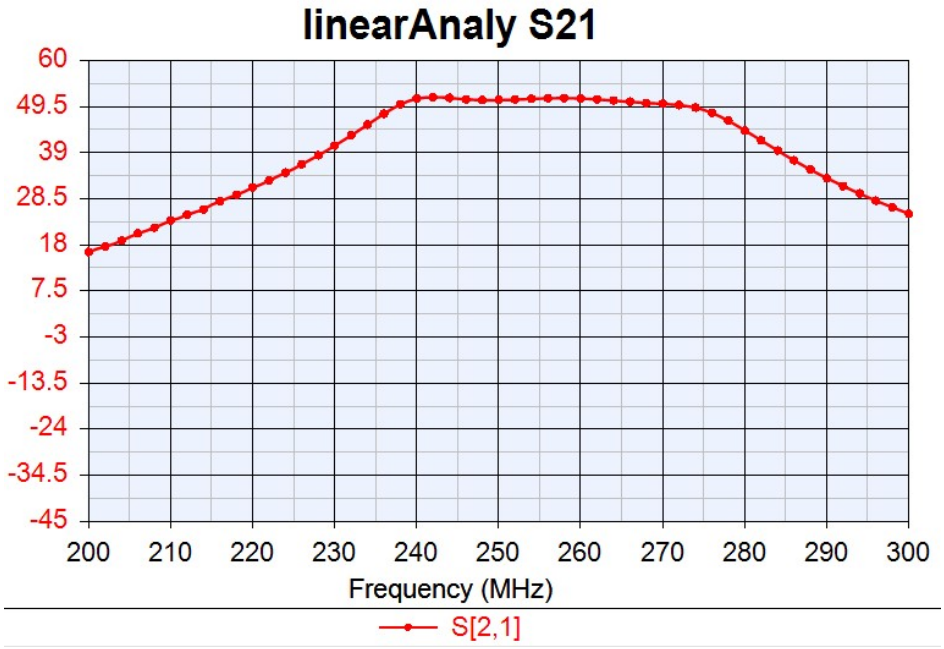

Figure A.18. Simulated S21 255 MHz

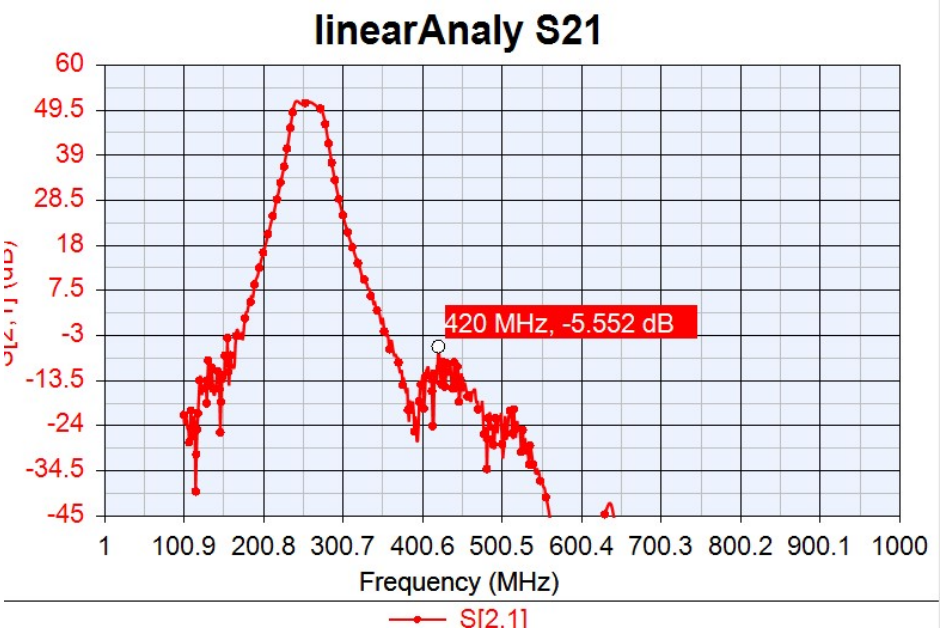

Figure A.19. Simulated S21 255 MHz

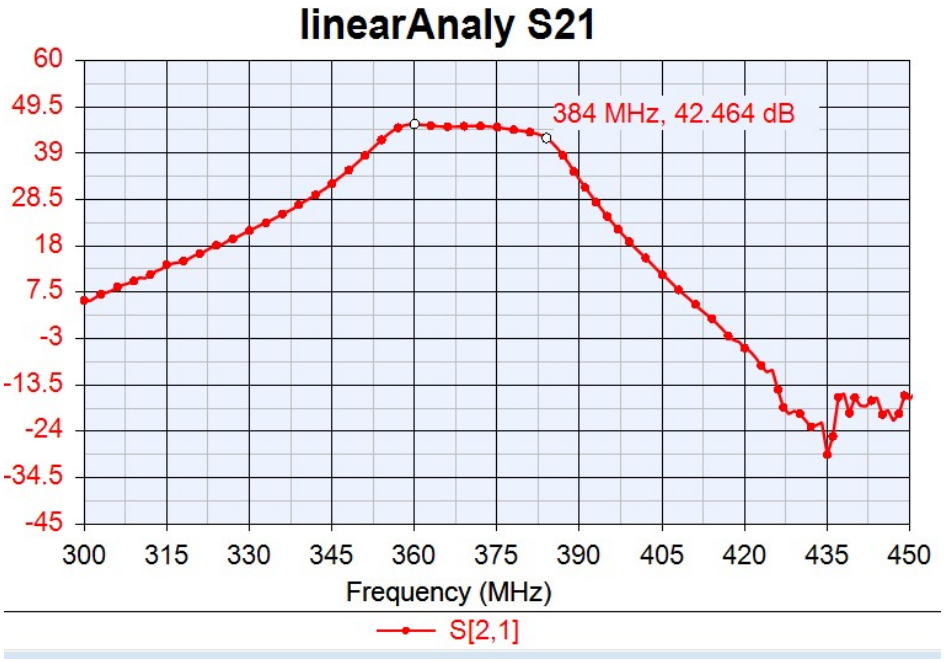

Figure A.20. Simulated S21 370 MHz

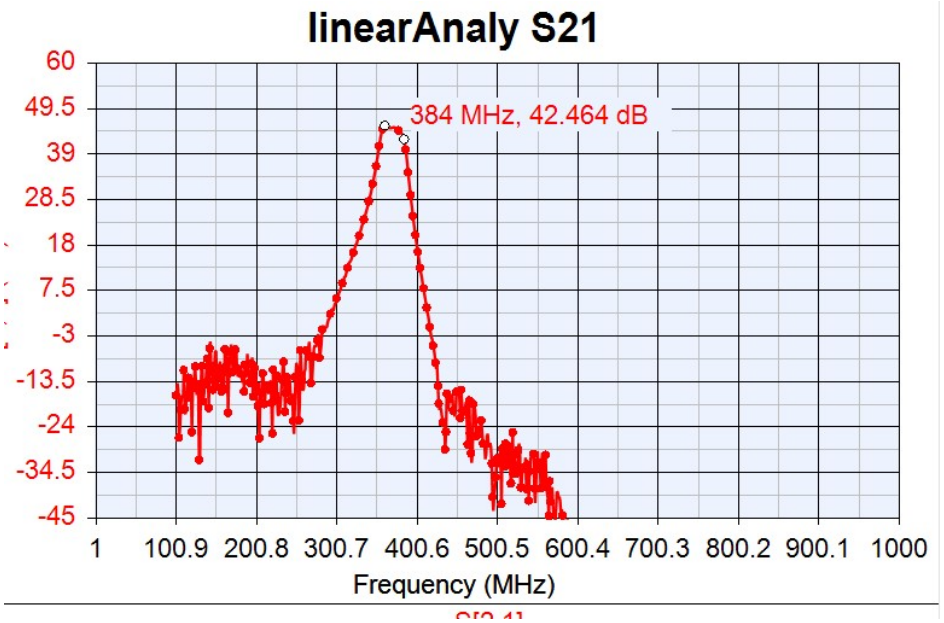

Figure A.21. Simulated S21 370 MHz

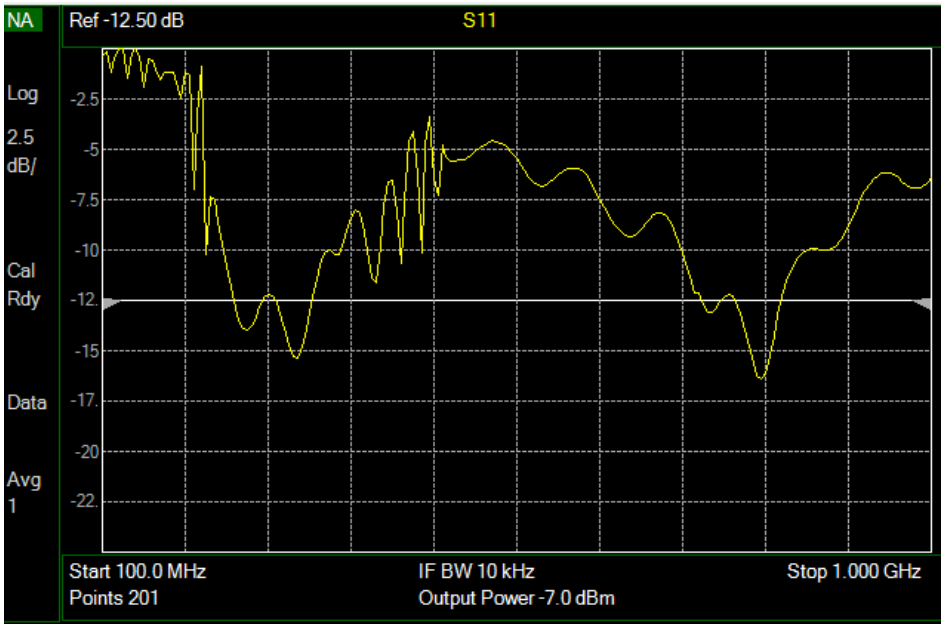

Figure A.22. Measured S21 RHCP

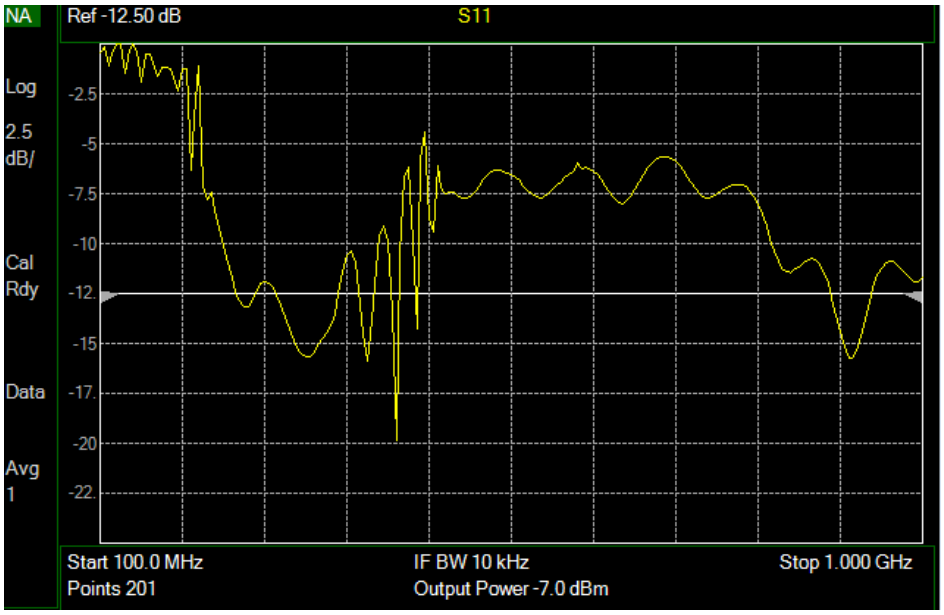

Figure A.23. Measured S21 LHCP

Observed PSDs

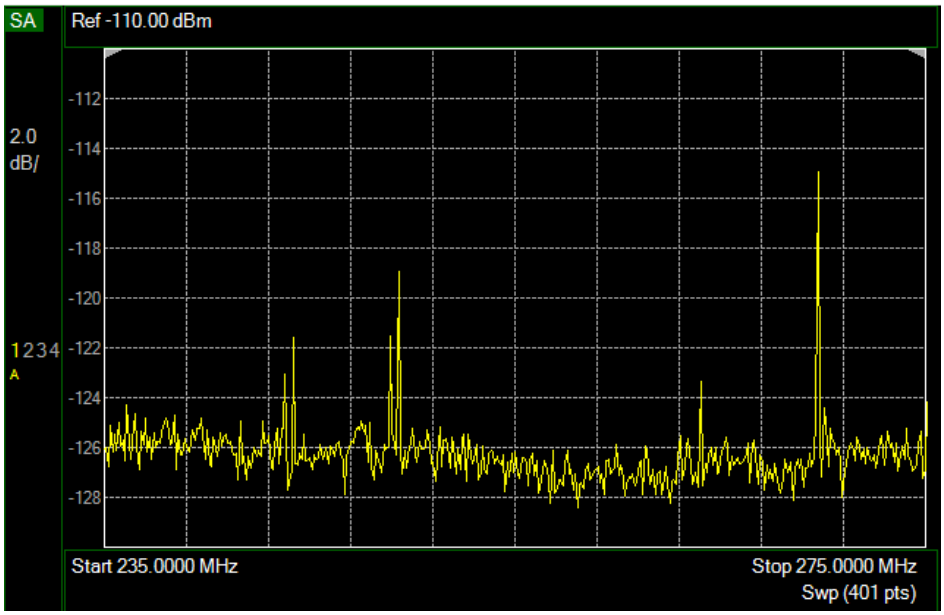

Figure A.24. RHCP 255MHz PSD

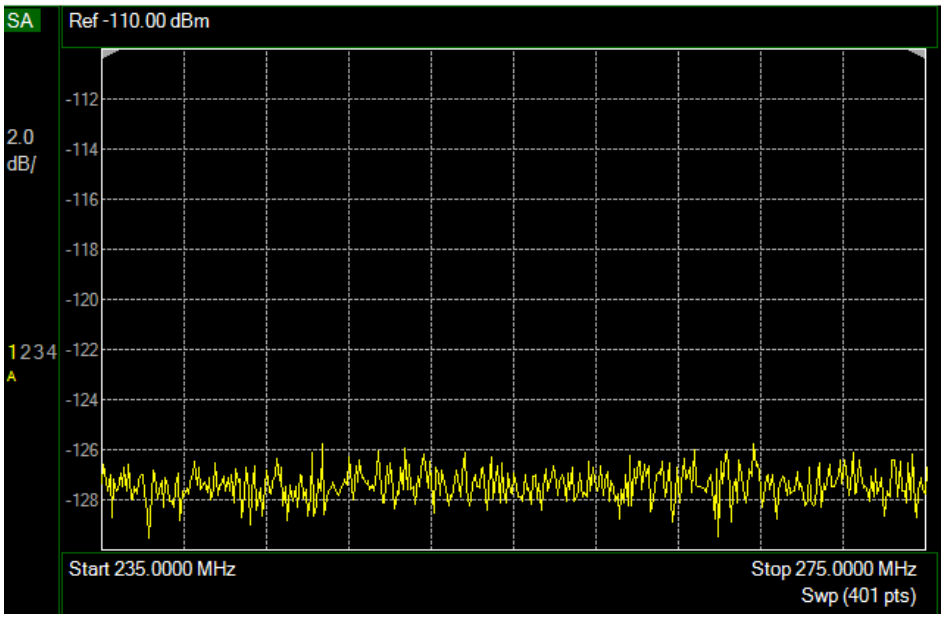

Figure A.25. LHCP 255MHz PSD

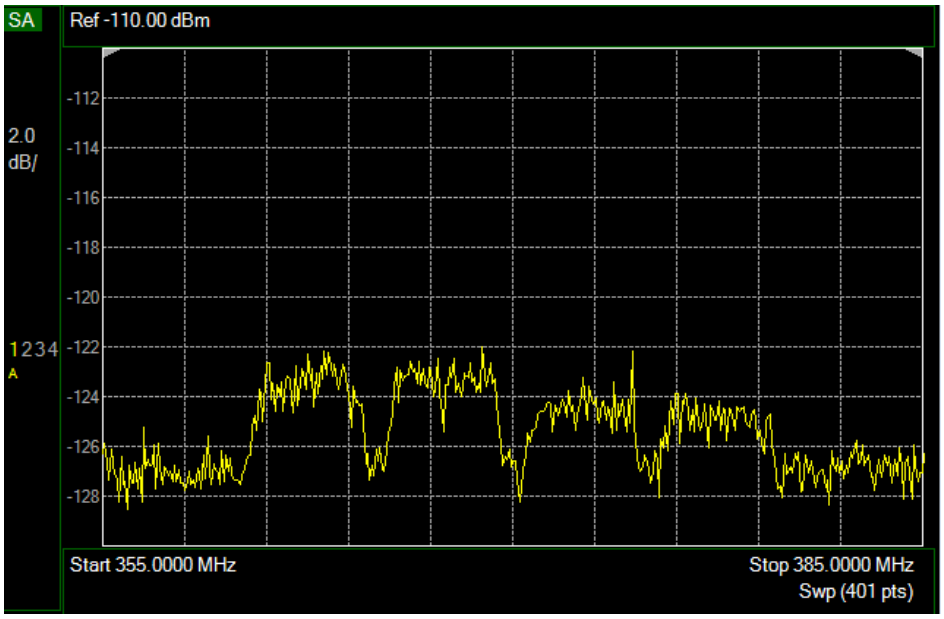

Figure A.26. RHCP 370MHz PSD

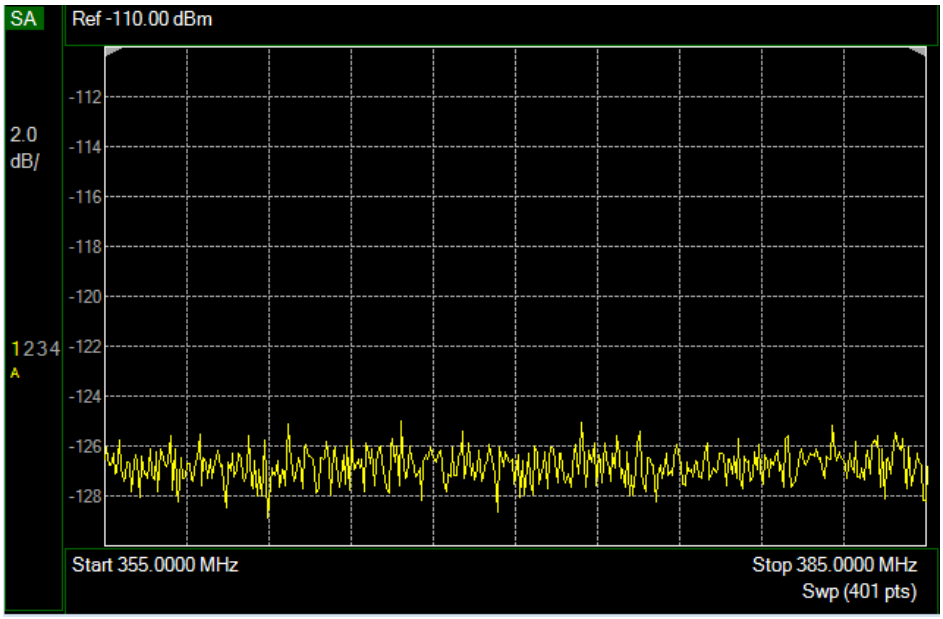

Figure A.27. LHCP 370MHz PSD

B. TOWER DEMONSTRATION APPENDIX

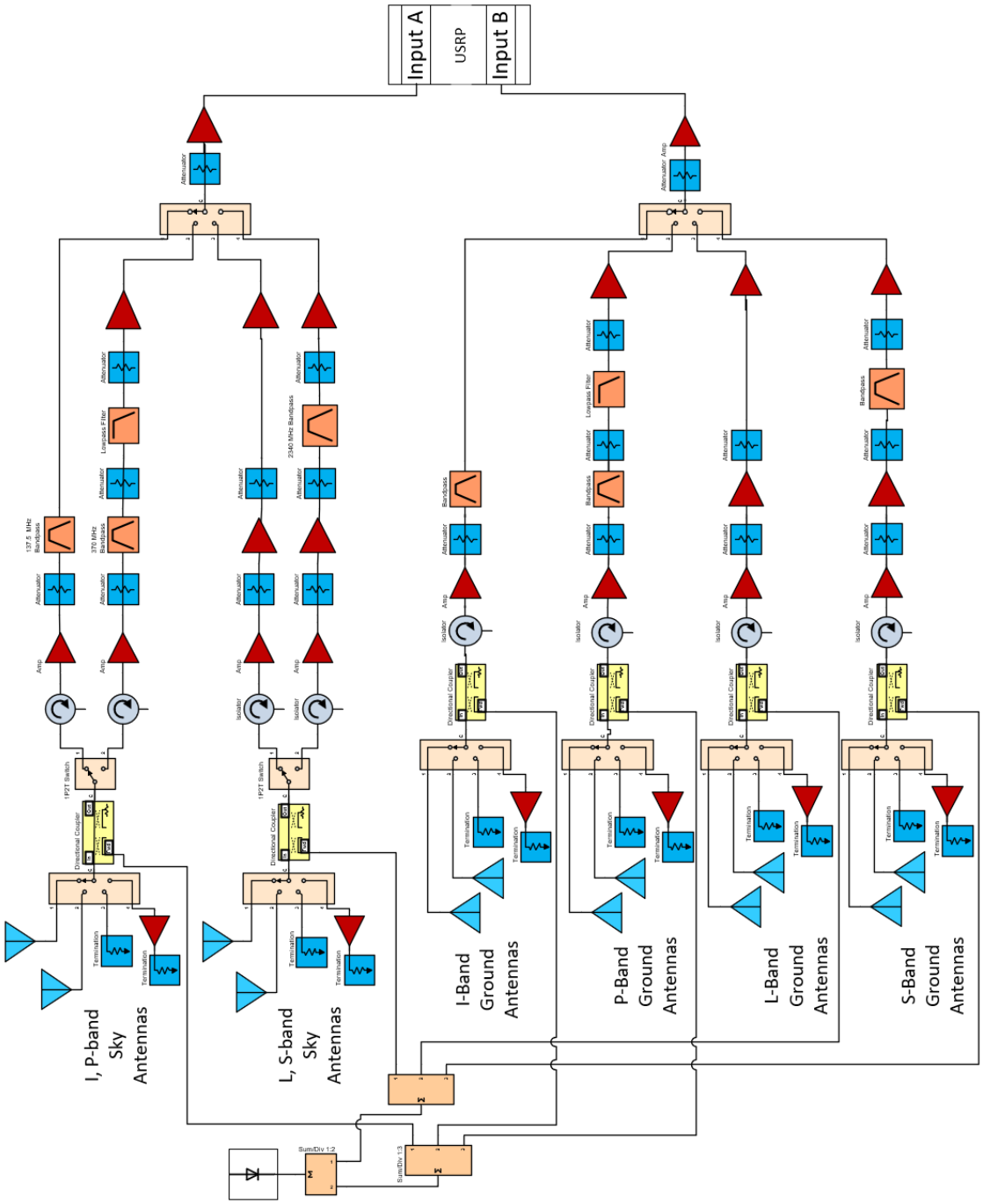

Figure B.1. Tower Front End Design

C. NOISE CORRELATION APPENDIX

This derivation follows derivations in Microwave remote sensing: Active and Passive - Chapter 7 [36]. Nyquist showed the output of a unity gain rectangular filter [37]:

$$V_{rms}^2 = \left\langle v^2(t) \right\rangle = 4RkTB$$

Then, the well known result relating signal power to an equivalent noise temperature:

$$P_n = I_{rms}^2 R = \left(\frac{F_{rms}}{2R}\right) R = \frac{V_{rms}^2}{4R} = kTB$$

Thermal noise in a microwave receiver is the summation of infinitesimally short bursts of current. All of these sources are uncorrelated. We can model the instantaneous voltage at the intermediate frequency (IF) f_{IF} as a time varying sinusoid:

$$v_n(t) = V_n cos(2\pi f_{IF} t + \phi_n)$$

Because the input is noise, $v_{\mathrm{e}}(t)$, $\phi(t)$ are independent. It is easy to see that:

$$E\Big[v_{IF}\Big] = 0$$

The IF voltage would then be the summation of these sources:

$$V_{IF}(t) = \sum_{n=1}^{N_s} V_n cos(2\pi f_{IF} t + \phi_n)$$

Rewriting in phase-notation, where V_n is the envelope of the signal:

$$V_{IF}(t) = \sum_{n=1}^{N_s} V_n \mathrm{e}^{\mathrm{j}\phi_n}$$

V_{IF} are two normally distributed zero mean, uncorrelated random variable. Because they are normal random variables, uncorrelated also means they are statistically independent. Their joint PDF is:

$$p(V_x, V_y) = \frac{1}{\sqrt{2\pi}\sigma^2} \mathrm{e}^{-V_x^2/2\sigma^2} \frac{1}{\sqrt{2\pi}\sigma^2} \mathrm{e}^{-V_y^2/2\sigma^2} = \frac{1}{\sqrt{2\pi}\sigma^2} \mathrm{e}^{-(V_x^2+V_y^2)/2\sigma^2} \tag{C.1}$$

We then convert this into a pdf in polar coordinates via the transformation:

$$\begin{aligned} p(V_x, V_y)\ dV_x\ dV_y &= p(V_\mathrm{e}, \phi)\ dV_\mathrm{e}\ d\phi \\ V_\mathrm{e}\ dE_\mathrm{e}\ d\phi &= dV_x\ dV_y \\ V_\mathrm{e}^2 &= V_x^2 + V_y^2 \end{aligned}$$

we obtain:

$$\begin{aligned} p(V_\mathrm{e}, \phi) &= \frac{V_\mathrm{e}}{2\pi\sigma^2} \mathrm{e}^{-V_\mathrm{e}/2\sigma^2} \\ 0 \leq V_\mathrm{e} \leq \infty, 0 \leq \phi \leq 2\pi \end{aligned}$$

The phase angle ϕ is uniform over $[0, 2\pi]$:

$$p(V_\mathrm{e}) = \int_0^{2\pi} p(V_\mathrm{e}, \phi) d\phi$$

we arrive at a Rayleigh distribution:

$$P(V_\mathrm{e}) = \begin{cases} \frac{V_\mathrm{e}}{\sigma^2} \mathrm{e}^{-v_\mathrm{e}^2/2\sigma^2} & v_\mathrm{e} \geq 0 \\ 0 & v_\mathrm{e} \leq 0 \end{cases}$$

In words: this is the amplitude of the voltage of a noise source; a summation of many Gaussian noise processes. σ is the same σ in the Gaussian variable. Note that the mean of this Rayleigh distribution (voltage amplitude) is not zero:

$$E[V] = E[V_\mathrm{e}^2] = \sqrt{\frac{\pi}{2}}\sigma$$

The second moment of a Rayleigh distribution:

$$E^2[V_e^2] = 2\sigma^2$$

For a classical radiometer setup, a square-law detector would be used to measure the signal power. This is effectively an integrator of the signal power (V_e^2) with a finite integration time. The relationship between the detector and the input voltage is given by:

$$V_d = CV^2$$

Where C is a gain constant of the detector.

A squared Rayleigh distribution is an exponential distribution:

$$Y = g(X) = X^2$$
$$g^{-1}(Y) = \sqrt{Y}$$
$$V_d = \frac{\sqrt{Y}}{\sigma^2} e^{y/\sigma^2} \frac{1}{2\sqrt{Y}} = \frac{1}{2\sigma^2} e^{-y/\sigma^2}$$

With $E[V_d] = 2\sigma^2$ and a variance $2\sigma^2$

$$E[V_d] = C\ E[V^2] = 2C\sigma^2 = CkBT \tag{C.2}$$

This is the average value of the input noise power.

The detector will average a finite number of samples together to estimate the signal power.

$$\hat{\bar{P}} = E[V_d] = \frac{1}{N} \sum_{i=1}^{N} V_d \tag{C.3}$$

$$E[V_d^2] = \frac{\hat{\bar{P}}^2}{N} \tag{C.4}$$

Then the standard deviation of this measurement:

$$E[V_d^2] - E^2[V_d] = \frac{\hat{\bar{P}}}{\sqrt{N}} = \frac{kTB}{\sqrt{N}} \tag{C.5}$$

Relate to bandwidth

The variance of an integration, continuous or when samples are sufficiently close in time relitivive to the spacing between the independent samples [38]:

$$\sigma_T^2 = \frac{2}{T}\int_0^T \Big(1 - \frac{x}{T}\Big) R_{sf}(x)dx \tag{C.6}$$

$R_{sf}(\tau)$ is the auto-covariance function: $R_{sf} = R_s(\tau) - \hat{P}_e{}^2$. $R_s(\tau)$ is the auto-correlation function. We are sampling a band limited Gaussian process with an auto-correlation given in 3.8. We place the requirement to integrate T much longer than then time for the auto-covariance to reduce to 0. Then:

$$R_{sf} = \bar{P}^2 sinc(\pi B\tau)^2 \tag{C.7}$$

Using Equation C.4:

$$N = \frac{\bar{P}^2 T}{2\int_0^T \Big(1 - \frac{x}{T}\Big) R_{sf}(x)dx} \tag{C.8}$$

Observe $\frac{x}{T} \approx 0$ when the auto-covariance function is of significant size.

Per Ulaby:

$$\sigma_T^2 \approx \frac{\bar{P}^2}{\pi BT}\left[\frac{cos(2\pi BT) - 1}{\pi BT} + 2Si(2\pi BT)\right] \tag{C.9}$$

Where, $Si(x) = \int_0^x sin(t)/t\ dt$. When $BT >> 1$ the first term ≈ 0 and the sine integral is $\approx \pi$. We finally get

$$\sigma_T^2 \approx \frac{\hat{P}^2}{BT} \tag{C.10}$$

$$N \approx BT \tag{C.11}$$

Precision of power estimate

A received signal power can be modeled as:

$$\bar{P}_r = \bar{P}_s + \bar{P}_n \tag{C.12}$$

The signal to noise ration can be expressed as:

$$S_n = \frac{\bar{P}_s}{\bar{P}_n} \tag{C.13}$$

When a square law detector is used, as shown in Equation C.5 the variance of the measurement:

$$\sigma_r = \frac{\bar{P}_s + \bar{P}_n}{\sqrt{N}} \tag{C.14}$$

The precision of the estimate for noise power has been derived above.

Then we arrive at:

$$\sigma_s = \hat{P}_s \sqrt{\frac{1}{N_r}\left(1 + \frac{1}{S_N}\right)^2 + \frac{1}{N_n}\left(\frac{1}{S_n}\right)^2} \tag{C.15}$$

Where $N_r = B\tau$ for the P_r samples and $N_n = B\tau$ is for the noise samples.

VITA

Benjamin Nold was born in Michigan on July 17th, 1993. He attended Oakland University where he obtained an undergraduate degree in Computer Engineering in April of 2016. The following August, he began his graduate studies at Purdue University in West Lafayette, IN where he worked as a graduate research assistant in the Radio Navigation Lab for Dr. James Garrison. In August of 2019 he obtained a Masters of Science in Electrical and Computer Engineering. He received his Doctor of Philosophy in Electrical and Computer Engineering in May of 2023.

Benjamin Nold was a pathways CoOp at NASA Goddard Space Flight Center since January of 2017 in the Components and Hardware Systems Branch. He worked on spaceborne GPS receivers and on the PetitSat, BurstCube and SNOOPI cubesats. He is scheduled to transition to full time at NASA GSFC in the Summer of 2023.

PUBLICATION

- Garrison, J., **Nold, B.**, Masters, D., Brown, C., Bridgeman, J., Mansell, J., Vega, M., Bindlish, R., Piepmeier, J., & Babu, S. (2023). A Spaceborne Demonstration of P-Band Signals-of-Opportunity (SoOp) Reflectometry. Pre-publication in TechRxiv

- Garrison, J., **Nold, B.**, Masters, D., Brown, C., Bridgeman, J., Mansell, J., Vega, M., & Piepmeier, J. (2022). Demonstrating Spaceborne P-band Signals of Opportunity Reflectometry. In AGU Fall Meeting Abstracts (pp. NS42A08).

- Garrison, J., Vega, M., Shah, R., Bindlish, R., Kurum, M., **Nold, B.**, & Kim, S. (2022). Remote Sensing of the water cycle using Signals of Opportunity: challenges and opportunities. Authorea Preprints.

- Garrison, J., Mansell, J., **Nold, B.**, Shah, R., Vega, M., Kim, S., Raymond, J., Bindlish, R., Kurum, M., Piepmeier, J., & others (2022). Instrument Science Experiments on the SNOOPI P-Band Reflectometry Mission. In IGARSS 2022-2022 IEEE International Geoscience and Remote Sensing Symposium (pp. 71467149).

- **Nold, B.**, Vega, M., & Garrison, J. (2022). Design of a Ground Based Power and Ambiguity Function Monitor for P-Band Signals of Opportunity Sources. In IGARSS 2022-2022 IEEE International Geoscience and Remote Sensing Symposium (pp. 76287631).

- Kim, S., Smith, E., **Nold, B.**, Choudhari, A., & Garrison, J. (2022). Multi-Frequency Signals of Opportunity Soil Moisture Retrievals for Agricultural Applications. In IGARSS 2022-2022 IEEE International Geoscience and Remote Sensing Symposium (pp. 42044207).

- Garrison, J., Bindlish, R., Kurum, M., Boyd, D., Kim, S., Choudhari, A., Smith, E., & **Nold, B.** (2021). Sub-surface Soil Moisture Profile Retrieval using Multi-frequency Signals of Opportunity. In AGU Fall Meeting Abstracts (pp. H54B06).

- Shah, R., Garrison, J., Shah, R., Kim, S., Piepmeier, J., Vega, M., Spencer, D., Banting, R., Raymond, J., **Nold, B.**, & others (2020). Analyses Supporting Snoopi: a P-band Reflectometry Demonstration. In 2021 IEEE International Geoscience and Remote Sensing Symposium IGARSS

- Garrison, J., Bindlish, R., Kurum, M., Shah, R., Vega, M., **Nold, B.**, Mansell, J., Raymond, J., Banting, R., & Kim, S. (2021). Hydrology Remote Sensing using P-band Signals of Opportunity (SoOp), the SNOOPI Demonstration Mission. In AGU Fall Meeting Abstracts (pp. A33C05).

- Garrison, J., Shah, R., **Nold, B.**, Mansell, J., Vega, M., Raymond, J., Bindlish, R., Kurum, M., Piepmeier, J., Kim, S., & others (2021). SNOOPI: Demonstrating P-band reflectometry from orbit. In 2021 IEEE International Geoscience and Remote Sensing Symposium IGARSS (pp. 164167).

- Boyd, D., Kurum, M., Garrison, J., **Nold, B.**, Vega, M., Bindlish, R., & Piepmeier, J. (2021). Development of Spaceborne SoOp Reflectometry Model for Complex Terrains. In 2021 IEEE International Geoscience and Remote Sensing Symposium IGARSS (pp. 14291431).

- Garrison, J., Piepmeier, J., Shah, R., Vega, M., Bindlish, R., & **Nold, B.** (2021). Measurement Validation Approach for SigNals Of Opportunity: P-band Investigation (SNOOPI). 43rd COSPAR Scientific Assembly. Held 28 January-4 February, 43, 57.

- Garrison, J., Shah, R., Kim, S., Piepmeier, J., Vega, M., Spencer, D., Banting, R., Raymond, J., **Nold, B.**, Larsen, K., & others (2020). Analyses Supporting Snoopi: a P-Band Reflectometry Demonstration. In IGARSS 2020-2020 IEEE International Geoscience and Remote Sensing Symposium (pp. 33493352).

- Boyd, D., Kurum, M., Eroglu, O., Gurbuz, A., Garrison, J., **Nold, B.**, Vega, M., Piepmeier, J., & Bindlish, R. (2020). SCoBi Multilayer: a signals of opportunity reflectometry model for multilayer dielectric reflections. Remote Sensing, 12(21), 3480.

- **Nold, B.** (2019). Design of an Instrument for Soil Moisture and Above Ground Biomass Remote Sensing using Signals of Opportunity. (Masters thesis, Purdue University Graduate School).

- Boyd, D., Gurbuz, A., Kurum, M., Garrison, J., Nold, B.**Nold, B.**, Piepmeier, J., Vega, M., & Bindlish, R. (2020). Cramerrao lower bound for soop-r-based root-zone soil moisture remote sensing. IEEE journal of selected topics in applied earth observations and remote sensing, 13, 61016114.

- Garrison, J., Piepmeier, J., Lin, Y.C., Bindlish, R., **Nold, B.**, Vega, M., Cosh, M., & Du Toit, C. (2017). P-band signals of opportunity: A new approach to remote sensing of root zone soil moisture. In Annual Meeting, Tampa, FL, American Society of AgronomyCrop Science Society of AmericaSoil Science Society of America (pp. 815).

- Garrison, J., Piepmeier, J., Shah, R., Vega, M., Spencer, D., Banting, R., Raymond, J., **Nold, B.**, Larsen, K., & Bindlish, R. (2019). Definition of a Technology Validation Mission for P-band Reflectometry using Signals of Opportunity. In Workshop on Advanced RF Sensors and Remote Sensing Instruments, ARSI'19.

- Garrison, J., Piepmeier, J., Shah, R., Vega, M., Spencer, D., Banting, R., Firman, C., **Nold, B.**, Larsen, K., & Bindlish, R. (2019). SNOOPI: A technology validation mission for P-band reflectometry using signals of opportunity. In IGARSS 2019-2019 IEEE International Geoscience and Remote Sensing Symposium (pp. 50825085).

- Boyd, D., Kurum, M., Garrison, J., **Nold, B.**, Gurbuz, A., LaGrone, B., Eroglu, O., Mdrafi, R., Piepmeier, J., Vega, M., & others (2019). Inversion Study of Simulated and Physical Soil Moisture Profiles using Multifrequency Soop-Sources. In IGARSS 2019-2019 IEEE International Geoscience and Remote Sensing Symposium (pp. 52595262).

- Kurum, M., Boyd, D., Garrison, J., **Nold, B.**, Bindlish, R., Piepmeier, J., & Vega, M. (2019). Assessment of Value of Multiple Signals of Opportunity (SoOp) for Estimating Root-Zone Soil Moisture (RZSM) Directly. In AGU Fall Meeting Abstracts (pp. IN23C14).

- Boyd, D., Kurum, M., Garrison, J., **Nold, B.**, Pignotti, G., Piepmeier, J., Vega, M., & Bindlish, R. (2018). Probing soil moisture up to root-zone by using multiple signals of opportunity. In 2018 International Conference on Electromagnetics in Advanced Applications (ICEAA) (pp. 206209).

- Garrison, J., Kurum, M., **Nold, B.**, Piepmeier, J., Vega, M., Bindlish, R., & Pignotti, G. (2018). Remote sensing of root-zone soil moisture using I-and P-band signals of opportunity: Instrument validation studies. In IGARSS 2018-2018 IEEE International Geoscience and Remote Sensing Symposium (pp. 83058308).

- Garrison, J., Lin, Y.C., **Nold, B.**, Piepmeier, J., Vega, M., Fritts, M., Du Toit, C., & Knuble, J. (2017). Remote sensing of soil moisture using P-band signals of opportunity (SoOp): Initial results. In 2017 IEEE International Geoscience and Remote Sensing Symposium (IGARSS) (pp. 41584161).

- Garrison, J., **Nold, B.**, Lin, Y., Pignotti, G., Piepmeier, J., Vega, M., Fritts, M., DuToit, C., & Knuble, J. (2017). Recent results on soil moisture remote sensing using P-band signals of opportunity. In 2017 International Conference on Electromagnetics in Advanced Applications (ICEAA) (pp. 16041607).

- Piepmeier, J., Vega, M., Fritts, M., Du Toit, C., Knuble, J., Lin, Y.C., **Nold, B.**, & Garrison, J. (2017). The radio frequency environment at 240270 MHz with application to signal-of-opportunity remote sensing. In 2017 IEEE International Geoscience and Remote Sensing Symposium (IGARSS) (pp. 12591262).